

We greatly value the careful reading and the detailed comments provided by the referees. The responses to the comments of the referees in our direct reply (shown below) and within the revised manuscript (see marked copy) are provided. The pages and lines indicated below correspond to those in the marked copy.

Response to Referee 1 (Referees' comments are italicized)

1. Referee comment: *“These observational data sets should be very useful for the researchers who are interested in the topic of aerosol acidity and organic acid partitioning (especially there are several observations still without reasonable explanations, such as the partitioning of formic and acetic acids). Thus, if possible, I suggest these valuable observational data can be made available/accessible to the research community. In fact, the journal says that “Authors are required to provide a statement on how their underlying research data can be accessed. This must be placed as the section “Data availability” at the end of the manuscript before the acknowledgements. Please see the manuscript composition for the correct sequence. If the data are not publicly accessible, a detailed explanation of why this is the case is required. The best way to provide access to data is by depositing them (as well as related metadata) in reliable public data repositories, assigning digital object identifiers, and properly citing data sets as individual contributions.”*

Author response: The data is made available upon request:

Page 27 line 841: “Data can be accessed by request (rweber@eas.gatech.edu).”

2. Referee comment: *“Section 2.2, Lines 262-263: the unit of H_aq^+ should be mole kg^{-1} and, given the Equation 1, the pH definition is based on molality rather than molarity.”*

Author response: The referee is correct in stating that the pH definition is based on molality rather than molarity, as recommended by IUPAC. However, most thermodynamic equilibrium models (e.g., ISORROPIA-II, E-AIM) report species in terms of concentration per volume of air (e.g., $\mu g\ m^{-3}$, $\mu mol\ m^{-3}$). In addition, the particle pH can be calculated in terms of molarity, using the concentrations of species expressed in terms of molarity ($mol\ L^{-1}$) and concentrations per volume of air (e.g., $\mu g\ m^{-3}$) as shown in previous studies. To remove any confusion, the following changes have been made to the manuscript:

Page 9 line 276: “The pH of an aqueous solution is defined as the negative logarithm of the hydronium ion (H_3O^+) activity on a molality basis (www.goldbook.iupac.org/html/P/P04524.html, last access: 6 July 2018):

$$pH = -\log_{10}[a(H^+)] = -\log_{10}[m(H^+)\gamma_m(H^+)/m^\theta] \quad (1a)$$

where $a(H^+)$ is the hydronium ion activity in an aqueous solution, $m(H^+)$ is the hydronium ion molality, $\gamma_m(H^+)$ is the molality-based hydronium ion activity coefficient, and m^θ is the standard molality ($1\ mol\ kg^{-1}$). For simplicity, H_3O^+ is denoted here as H^+ even though we recognize that the unhydrated hydrogen ion is rare in aqueous solutions. Since most thermodynamic equilibrium models (e.g., ISORROPIA-II, E-AIM) report species in terms of concentration per volume of air (e.g., $\mu g\ m^{-3}$, $\mu mol\ m^{-3}$), the particle pH can be calculated as:

$$pH = -\log_{10} \gamma_{H^+} H_{aq}^+ = -\log_{10} \frac{1000 \gamma_{H^+} H_{air}^+}{W_i + W_o} \cong -\log_{10} \frac{1000 \gamma_{H^+} H_{air}^+}{W_i} \quad (1b)$$

where γ_{H^+} is the molarity-based hydronium ion activity coefficient (assumed to be 1), H_{aq}^+ (mole L⁻¹) is the molar concentration of hydronium ions in particle water (i.e., pH is calculated in terms of molarity), H_{air}^+ (μg m⁻³) is the hydronium ion concentration per volume of air, and W_i and W_o (μg m⁻³) are the bulk particle water concentrations associated with inorganic and organic species per volume of air, respectively. In equation 1b, the molecular weight of H⁺ is taken as 1 g mole⁻¹, and 1000 is the factor needed for unit conversion of g L⁻¹ to μg m⁻³.”

3. Referee comment: “Section 3.3, Lines 424-425: it is mentioned that “diurnal variation in particle pH is driven by W_i ”. Can the authors provide a quantitative analysis to show the relationship in the pH and W_i diurnal variations? I feel the W_i may not be the dominant factor that affects the diurnal variation of pH.”

Author response: The referee is correct in stating that W_i is not the dominant factor that affects the diurnal variation of particle pH. Further analysis of the diurnal profiles of W_i and H_{air}^+ reveals that their maximum/minimum ratios are comparable (6.5 and 5.3, respectively). This indicates that the diurnal variation of particle is driven by both W_i and H_{air}^+ . This information has been added to the revised manuscript:

Page 15 line 475: “PM₁ pH varied by approximately 1.4 units throughout the day. W_i has an average value of 1.6 ± 1.7 μg m⁻³. PM₁ W_i and pH showed similar diurnal profiles, with both peaking in the mid-morning and reaching their minima in the mid-afternoon. These diurnal trends are consistent with those previously reported by Guo et al. (2015) for PM₁ measured during the summer and winter in different parts of the southeastern U.S. Also shown in Fig. 3b is the diurnal profile of H_{air}^+ , which peaked in the mid-afternoon. The W_i and H_{air}^+ maximum/minimum ratios are comparable (6.5 and 5.3, respectively), thus indicating that the diurnal variation in particle pH is driven by both W_i and H_{air}^+ .”

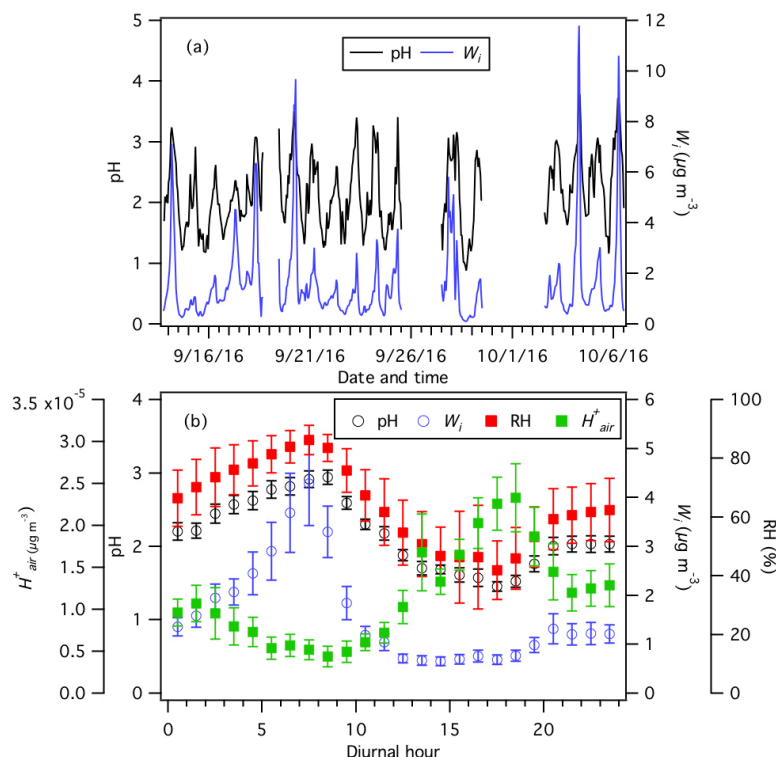


Figure 3: (a) Time series and (b) diurnal profiles of ISORROPIA-predicted PM_1 pH and W_i . The diurnal profiles of RH and ISORROPIA-predicted H^+_{air} are also shown in panel (b). Dates and times displayed are local time. All the data shown here represent averages in 1-hour intervals. Error bars shown in panel (b) are the standard errors.

4. Referee comment: “Section 3.3, Lines 429-439: the average pH of this study is 2.2, which is 0.3 pH unit higher than PM_1 pH in CalNex. The NH_3 level in this study is four times compared to CalNex. A 0.6 pH unit difference is expected from the relationship of 1 pH unit increase ~ 10 times increase in NH_3 . This manuscript attributes this 0.3 unit difference to much higher levels of sulfate and nitrate in CalNex. I think this statement is not well justified since the ambient temperature and RH in these two campaigns are also different. I suggest to provide a more thorough analysis on this pH difference or remove these sentences from the manuscript.”

Author response: The referee is correct in stating that meteorological differences, specifically ambient RH and temperature, in this study vs. the CalNex campaign may also contribute to the 0.3 pH unit difference. As such, we have revised the manuscript to be more circumspect about the role of $\text{PM}_1 \text{NO}_3^-$ mass concentrations in the CalNex campaign causing the 0.3 pH unit difference:

Page 16 line 498: “This may be due, in part, to $\text{PM}_1 \text{SO}_4^{2-}$ and NO_3^- mass concentrations at CalNex being approximately 2 times and 18 times larger than those of this study, respectively. Aerosol inorganic SO_4^{2-} and NO_3^- species are hygroscopic species. The much higher NO_3^- mass concentrations in the CalNex campaign (due, in part, to high NO_x emissions) increased particle W_i substantially, which diluted H^+ and raised particle pH, resulting in more gas-to-particle partitioning of NO_3^- , and eventually leading to pH levels similar to those observed in this study. This type of feedback does not happen in the southeastern U.S. where non-volatile SO_4^{2-} dominates the uptake of particle water. It is also possible that the higher RH and lower

temperatures during the CalNex campaign (relative to this study) contributed to high particle W_i , which diluted H^+ and raised particle pH levels similar to those observed in this study.”

5. Referee comment: *“Section 3.4: On the diurnal variations of organic acids. Several factors (such as emission sources and photochemical production) are provided to explain the diurnal variations of the gas-phase and particle-phase organic acids. The authors seem to ignore the role of phase partitioning on the diurnal variations of the organic acids. If the organic acids are in a gas-particle equilibrium, no matter how they are formed, they would be re-partitioned between these two phases depending on the pH value and the aerosol water mass.”*

Author response: The referee is correct in stating that gas-particle partitioning of organic acids can also contribute to the observed diurnal variations of the organic acids. As such, this possibility has been added to the revised manuscript:

Page 19 line 603: “Some of these gas-phase organic acids may also be formed in the particle phase during organic aerosol photochemical aging, with subsequent volatilization into the gas phase. The gas-particle partitioning of organic acids likely depends on thermodynamic conditions, which are controlled by particle pH and W_i and meteorological conditions as will be shown in section 3.5.”

6. Referee comment: *“Section 3.5, Lines 605-608: an increase from 81% to 89% is expected from the S curve analysis, and what are the corresponding values ($\epsilon_{C_2O_4^{2-}}$) for the observations? Do the observations support the S curve analysis?”*

Author response: Although the measured $\epsilon(C_2O_4^{2-})$ values are generally consistent with the calculated S curve, the measured $\epsilon(C_2O_4^{2-})$ data at particle pH 2.2 and 2.5 is not clear enough to give definite values to support S curve analysis due to data scatter. For example, the averages (\pm standard deviation) of the measured $\epsilon(C_2O_4^{2-})$ at pH 2.2 and pH 2.5 are similar (78 ± 3 % and 79 ± 3 %, respectively) because of the scatter. Therefore, we emphasize in the revised manuscript that the S curve can be used to gain a qualitative understanding of how high NH_3 events at the site affect oxalic acid gas-particle partitioning:

Page 22 line 704: “Since the measured $\epsilon(C_2O_4^{2-})$ are in general agreement with the analytically calculated S curve (Fig. 7), we can use the S curve to understand qualitatively how high NH_3 events at the site affect oxalic acid gas-particle partitioning. Here we define high NH_3 events as periods where the NH_3 concentration was higher than 13.3 ppb (which is the average NH_3 concentration + 1 standard deviation). As discussed in section 3.3, the PM_1 pH during high NH_3 events is 2.5 ± 0.6 , which is slightly higher than the average PM_1 pH of 2.2 ± 0.6 . Based on the S curve calculated using the average temperature and W_i values, $\epsilon(C_2O_4^{2-})$ increases from 81 % to 89 % when particle pH increases from 2.2 to 2.5. While this result indicates that high NH_3 concentrations can raise the particle pH sufficiently such that it can promote gas-to-particle partitioning of oxalic acid, this is not always the case. Specifically, increasing the particle pH from -2 (or lower) to 1 will not result in a significant increase in $\epsilon(C_2O_4^{2-})$. Therefore, whether or not particle pH, and consequently oxalic acid gas-particle partitioning, is sensitive to NH_3 concentration depends strongly on particle pH values.”

7. Referee comment: “Section 3.5, Lines 618-620: it reads from Figure S12 that there is a negative bias of $\epsilon\text{C}_2\text{O}_4(2-)$ during the daytime and a positive bias during the nighttime. Can the authors provide a more quantitative analysis for the diurnal variations of $\epsilon\text{C}_2\text{O}_4(2-)$?”

Author response: Note that Fig. S12 in the original manuscript is now Fig. S13 in the revised manuscript. First, we view this change in partitioning resulting from changes in temperature and particle W_i as a shift, not a bias. Second, the purpose of Fig. S13 is to show that the S curve will change during the transition from day to night as a result of changes in meteorological conditions and particle W_i . Ambient RH and temperatures are higher and lower at night, respectively. Particle W_i will increase as a result of these changes in RH and temperature during the transition from day to night. These changes in the meteorological conditions and particle W_i will generally result in a higher fraction of oxalic acid partitioning to the particle phase for particle pH in this study. Since this shift is non-linear (i.e., see changes in S curve shape), we feel the best way to show the changes is graphically, as done in Fig. S13. It is not possible to provide a more quantitative analysis of $\epsilon(\text{C}_2\text{O}_4^{2-})$.

8. Referee comment: “Section 3.5, Lines 625-627: I do not think the statement that “S curves can be used to estimate activity coefficients based on gas-particle partitioning data xxx” can be derived from the data analysis in this section. For example, in Equation 4, the relationship between $\epsilon\text{C}_2\text{O}_4(2-)$ and pH depends on three activity coefficients: those of H^+ , $\text{C}_2\text{H}_2\text{O}_4$, and C_2HO_4^- , and this relationship is nonlinear. In this case, it seems unlikely to obtain a reasonable value for any activity coefficient.”

Author response: We agree with the referee’s point. Therefore, we have removed the above-mentioned statement in the revised manuscript.

Response to Referee 2 (Referees’ comments are italicized)

1. Referee comment: “Line 17-40: I feel that the authors described mostly the summary of the results in the abstract. I strongly recommend highlighting important findings of the study in this section.”

Author response: We respectfully disagree with the referee’s comment that the abstract is mostly a summary of the results. There are five important findings of this study, and they have been highlighted in the abstract:

- 1) Despite the high NH_3 concentrations (average 8.1 ± 5.2 ppb), PM_{10} were highly acidic with pH values ranging from 0.9 to 3.8, and an average pH of 2.2 ± 0.6 .
- 2) The measured molar fraction of oxalic acid in the particle phase (i.e., particle-phase oxalic acid molar concentration divided by the total oxalic acid molar concentration) ranged between 47 and 90 % for PM_{10} pH 1.2 to 3.4.
- 3) The measured oxalic acid gas-particle partitioning ratios were in good agreement with their corresponding thermodynamic predictions, calculated based on oxalic acid’s physicochemical properties, ambient temperature, particle water and pH.
- 4) The measured formic and acetic acid gas-particle partitioning ratios did not agree with their corresponding thermodynamic predictions.

5) Our study suggests that while higher NH_3 concentrations may lead to higher organic aerosol mass concentrations due to increased gas-to-particle partitioning of some organic acids, this effect is minor since organic acids comprised a small fraction of the overall aerosol mass.

2. Referee comment: *“Line 22: Define “SOA”.”*

Author response: This is defined in the revised manuscript.

3. Referee comment: *“Line 26 and 27: What do authors mean by “study average”. I think it is enough to write only “average” in the entire manuscript.”*

Author response: We have replaced “study average” with “average” in the revised manuscript.

4. Referee comment: *“Line 32 and 33: I suggest to move the sentence “particle-phase.molar concentration” in the methods or results and discussion section.”*

Author response: The co-editor previously requested that the above-mentioned sentence be added to the abstract to prevent any confusion. Therefore, we will keep the sentence in.

5. Referee comment: *“Line 42-47: There are specific salts produced by the reaction of ammonia with sulfuric acid and nitric acid based on the meteorological conditions. I suggest the authors to briefly explain these points in the introduction.”*

Author response: As requested, we have added a brief explanation on how the formation of specific salts in the particle phase is dependent on environmental conditions in the revised manuscript:

Page 2 line 48: “The formation of particle-phase ammonium sulfate and nitrate salts in the aerosol phase depends on the thermodynamic states of their precursors and the environmental conditions, which can consequently affect aerosol pH. For example, Guo et al. (2017b) showed that for Southeast U.S. summertime conditions, as aerosol pH increases, the relative fractions of SO_4^{2-} and HSO_4^- increases and decreases, respectively.”

References:

Guo, H., Nenes, A., and Weber, R. J.: The underappreciated role of nonvolatile cations on aerosol ammonium-sulfate molar ratios, *Atmos. Chem. Phys. Discuss.*, 2017, 1-19, 10.5194/acp-2017-737, 2017b.

6. Referee comment: *“Line 53-55: Although the references have been provided to back up the sentence, I suggest to at least briefly describe how ammonia is produced by industrial and vehicular emission.”*

Author response: As requested, we have added a brief description of how NH_3 is produced from industrial and vehicular emissions:

Page 2 line 58: “The primary source of NH_3 in urban areas are industrial emissions (e.g., NH_3 synthesis, manufacture of ammonium nitrate and urea, fluid and thermal catalytic cracking processes in petroleum refinery), though vehicular emissions can be a significant NH_3 source in some heavily populated cities (Reis et al., 2009; Lamarque et al., 2010; Yao et

al., 2013; Sun et al., 2017). Vehicular NH₃ emissions are thought to be produced primarily from the reaction of nitrogen oxide with hydrogen in the presence of carbon monoxide in three-way catalysts of gasoline light duty vehicles (Barbier-Jr and Duprez, 1994; Whittington et al., 1995; Livingston et al., 2009; Suarez-Bertoa et al., 2014).”

References:

Barbier-Jr, J., and Duprez, D.: Steam Effects in 3-way catalysis, *Applied Catalysis B-Environmental*, 4, 105-140, 10.1016/0926-3373(94)80046-4, 1994.

Whittington, B. I., Jiang, C. J., and Trimm, D. L.: Vehicle exhaust catalysis: I. The relative importance of catalytic oxidation, steam reforming and water-gas shift reactions, *Catalysis Today*, 26, 41-45, 10.1016/0920-5861(95)00093-u, 1995.

Livingston, C., Rieger, P., and Winer, A.: Ammonia emissions from a representative in-use fleet of light and medium-duty vehicles in the California South Coast Air Basin, *Atmospheric Environment*, 43, 3326-3333, 10.1016/j.atmosenv.2009.04.009, 2009.

Reis, S., Pinder, R. W., Zhang, M., Lijie, G., and Sutton, M. A.: Reactive nitrogen in atmospheric emission inventories, *Atmos. Chem. Phys.*, 9, 7657-7677, 10.5194/acp-9-7657-2009, 2009.

Lamarque, J. F., Bond, T. C., Eyring, V., Granier, C., Heil, A., Klimont, Z., Lee, D., Liousse, C., Mieville, A., Owen, B., Schultz, M. G., Shindell, D., Smith, S. J., Stehfest, E., Van Aardenne, J., Cooper, O. R., Kainuma, M., Mahowald, N., McConnell, J. R., Naik, V., Riahi, K., and van Vuuren, D. P.: Historical (1850-2000) gridded anthropogenic and biomass burning emissions of reactive gases and aerosols: methodology and application, *Atmos. Chem. Phys.*, 10, 7017-7039, 10.5194/acp-10-7017-2010, 2010.

Yao, X. H., Hu, Q. J., Zhang, L. M., Evans, G. J., Godri, K. J., and Ng, A. C.: Is vehicular emission a significant contributor to ammonia in the urban atmosphere?, *Atmospheric Environment*, 80, 499-506, 10.1016/j.atmosenv.2013.08.028, 2013.

Suarez-Bertoa, R., Zardini, A. A., and Astorga, C.: Ammonia exhaust emissions from spark ignition vehicles over the New European Driving Cycle, *Atmospheric Environment*, 97, 43-53, 10.1016/j.atmosenv.2014.07.050, 2014.

7. Referee comment: “Line 322 and 323: Authors found that ammonia concentration decreased at 14:00 about 1 hour before temperature decreased. Did you measure the boundary layer height during the campaign as mentioned that the decrease in ammonia concentration was because of the change in the boundary layer height?”

Author response: The boundary layer height was not measured during the study. The decrease in NH₃ concentration was hypothesized to be due to changes in the boundary layer height. As such, we have revised the manuscript to be more circumspect about changes in the boundary layer being the cause of the decrease in NH₃ concentration:

Page 12 line 351: “NH₃ decreased at 14:30, approximately 1 hour before temperature decreased, and may be due to changes in the boundary layer height. However, this hypothesis cannot be tested since the boundary layer height was not measured during the study.”

8. Referee comment: *“Line 368-370: This study found that PILS and filter-based measurements of sulfate is two times lower than that of HR-TOF-AMS measurement. The similar results are also observed for nitrate and ammonium. I suggest clarifying the reason behind this in the revised manuscript.”*

Author response: Disagreements between the HR-ToF-AMS and PILS and filter-based measurements are due to our application of composition-dependent collection efficiency (CDCE) values to the raw HR-ToF-AMS data. In our previous manuscript, we calculated CDCE values using the CDCE parameterization method proposed by Middlebrook et al. (2012), which derives CE values based largely on aerosol inorganic species concentrations and the relative humidity in the sampling line. Under our sampling conditions, the Middlebrook parameterization method estimated CDCE values of 0.44 to 0.55 (average of 0.45). However, the application of these CDCE values to the raw HR-ToF-AMS data resulted in the SO₄²⁻, NO₃⁻ and NH₄⁺ measurements being higher than the PILS and filter-based measurements. This is likely due to organics dominating the aerosol composition during the study (average of 74.2 ± 7.9 % of the non-refractory PM₁ mass concentration). Lee et al. (2015) suggested that a high organic mass fraction may hinder the complete efflorescence of aerosols when they are passed through the drier prior to delivery into the HR-ToF-AMS, reducing the particle bounce and increasing the CE value. As described in our previous manuscript, the CDCE-corrected HR-ToF-AMS measurements had to be scaled by a constant factor of 0.5 in order for them to agree with the PILS and filter-based measurements. It should be noted a previous ambient study also reported poor agreement between the CDCE-corrected HR-ToF-AMS measurements and parallel aerosol composition measurements due to high organic aerosol mass concentrations (see Lee et al. (2015)).

For these reasons, we applied a constant CE value of 0.9 to the raw HR-ToF-AMS data. This CE value was determined from comparisons of the raw HR-ToF-AMS data with PILS measurements. To remove any confusion, the following changes have been made to the manuscript:

Page 6 line 187: “Composition-dependent collection efficiency (CDCE) values of 0.44 to 0.55 were determined using the procedure detailed by Middlebrook et al. (2012), where CDCE values are derived based largely on aerosol inorganic species concentrations and the relative humidity in the sampling line. In addition, a constant collection efficiency (CE) value of 0.9 was determined from the comparison of raw HR-ToF-AMS SO₄²⁻ data with other particulate SO₄²⁻ measurements performed during the study. Comparisons of aerosol mass concentrations obtained from the application of CDCE values (i.e., 0.44 to 0.55) vs. a constant CE value (i.e., 0.9) to the raw HR-ToF-AMS data are discussed in section 3.2.”

Page 13 line 389: “The aerosol inorganic chemical composition was measured by several instruments during this study. The HR-ToF-AMS, PILS-IC and PILS-HPIC measured the composition of PM₁, while a filter-based particle composition monitor measured the composition of PM_{2.5}. Comparisons of aerosol SO₄²⁻, NO₃⁻ and NH₄⁺ mass concentrations obtained from the application of CDCE values to the raw HR-ToF-AMS data are compared to those measured by the other three instruments in Fig. S6. NH₄⁺ measurements by the PILS-IC are not available for comparison due to denuder breakthrough that occurred

during the study.

SO₄²⁻ measurements by the various instruments are generally well correlated with each other, with R² values ranging from 0.64 to 0.92. Although PM₁ SO₄²⁻ measurements by the two PILS systems show good agreement with each other, HR-ToF-AMS CDCE-applied SO₄²⁻ measurements are approximately two times higher than the PILS and filter measurements. Similar systematic differences are also observed for NO₃⁻ and NH₄⁺ measurements. NO₃⁻ and NH₄⁺ measurements by the four instruments are moderately correlated (R² = 0.54 to 0.79 and R² = 0.94, respectively). NO₃⁻ measurements by the PILS and filter systems are mostly similar; however, HR-ToF-AMS CDCE-applied PM₁ NO₃⁻ and NH₄⁺ measurements are approximately three times and two times higher than the PILS and filter measurements. One possible reason is that the calculated CDCE is lower due to organics dominating the aerosol composition during the study (average of 74.2 ± 7.9 % of the non-refractory PM₁ mass concentration). Lee et al. (2015) suggested that a high organic mass fraction may impede the complete efflorescence of aerosols when they are passed through the drier prior to delivery into the HR-ToF-AMS, thus reducing the particle bounce and increasing the CE value. Hence, we estimated HR-ToF-AMS PM₁ mass concentrations that would be consistent with PILS and filter measurements by multiplying all the raw HR-ToF-AMS data by a constant CE value of 0.9, which was obtained from comparisons of the raw HR-ToF-AMS SO₄²⁻ data with PILS-IC and PILS-HPIC SO₄²⁻ measurements. The constant CE-applied HR-ToF-AMS data is used in all our subsequent analyses.

Figure S6 caption: “Aerosol (panels a to d) SO₄²⁻, (panels e to h) NO₃⁻, and (i) NH₄⁺ comparisons between HR-ToF-AMS, PILS-IC, PILS-HPIC and filters for the entire field study. CDCE values were applied to the raw HR-ToF-AMS data to obtain the mass concentrations shown here (see main text for details). For comparisons between the HR-ToF-AMS, PILS-IC and PILS-HPIC data (panels c, d, g and h), the measurements are averaged over 1 hour intervals. For comparisons with filter data (panels a, b, e, f and i), the HR-ToF-AMS, PILS-IC and PILS-HPIC data are averaged over 24 hour intervals. Orthogonal regression fits are shown. Uncertainties in the fits are 1 standard deviation.”

References:

Lee, B. P., Li, Y. J., Yu, J. Z., Louie, P. K. K., and Chan, C. K.: Characteristics of submicron particulate matter at the urban roadside in downtown Hong Kong-Overview of 4 months of continuous high-resolution aerosol mass spectrometer measurements, *Journal of Geophysical Research-Atmospheres*, 120, 7040-7058, 10.1002/2015jd023311, 2015.

Middlebrook, A. M., Bahreini, R., Jimenez, J. L., and Canagaratna, M. R.: Evaluation of Composition-Dependent Collection Efficiencies for the Aerodyne Aerosol Mass Spectrometer using Field Data, *Aerosol Science and Technology*, 46, 258-271, 10.1080/02786826.2011.620041, 2012.

9. Referee comment: “Line 386-398: This is an exciting result that the organic aerosol mass concentration was higher at nighttime. This result probably indicated the unique atmospheric processing of organic aerosols in the nighttime. Nevertheless, I did not find any discussion on the formation mechanisms of organic aerosols at nighttime. I suggest discussing this point in the revised version.”

Author response: As requested, we have added some discussion on the possible nighttime formation mechanisms of organic aerosols in the revised manuscript:

Page 14 line 420: “Organic aerosol mass concentration was slightly higher at night, which is likely caused by changes in the boundary layer height, emission sources and SOA formation processes (Xu et al., 2015b). Previous studies have shown that nighttime SOA production in the Southeastern U.S. is largely attributed to nitrate radical oxidation and ozonolysis of monoterpenes, which are abundant at night (Pye et al., 2015; Xu et al., 2015a; Xu et al., 2015b; Lee et al., 2016; Zhang et al., 2018). Specifically, the nitrate radical oxidation of some monoterpenes (e.g., β -pinene) could form low volatility organic nitrates that are condensable and could contribute substantially to the nocturnal organic aerosol mass (Boyd et al., 2015; Boyd et al., 2017; Ng et al., 2017).”

References:

Boyd, C. M., Sanchez, J., Xu, L., Eugene, A. J., Nah, T., Tuet, W. Y., Guzman, M. I., and Ng, N. L.: Secondary organic aerosol formation from the beta-pinene+NO₃ system: effect of humidity and peroxy radical fate, *Atmos. Chem. Phys.*, 15, 7497-7522, 10.5194/acp-15-7497-2015, 2015.

Boyd, C. M., Nah, T., Xu, L., Berkemeier, T., and Ng, N. L.: Secondary Organic Aerosol (SOA) from Nitrate Radical Oxidation of Monoterpenes: Effects of Temperature, Dilution, and Humidity on Aerosol Formation, Mixing, and Evaporation, *Environmental Science & Technology*, 51, 7831-7841, 10.1021/acs.est.7b01460, 2017.

Lee, B. H., Mohr, C., Lopez-Hilfiker, F. D., Lutz, A., Hallquist, M., Lee, L., Romer, P., Cohen, R. C., Iyer, S., Kurten, T., Hu, W. W., Day, D. A., Campuzano-Jost, P., Jimenez, J. L., Xu, L., Ng, N. L., Guo, H. Y., Weber, R. J., Wild, R. J., Brown, S. S., Koss, A., de Gouw, J., Olson, K., Goldstein, A. H., Seco, R., Kim, S., McAvey, K., Shepson, P. B., Starn, T., Baumann, K., Edgerton, E. S., Liu, J. M., Shilling, J. E., Miller, D. O., Brune, W., Schobesberger, S., D'Ambro, E. L., and Thornton, J. A.: Highly functionalized organic nitrates in the southeast United States: Contribution to secondary organic aerosol and reactive nitrogen budgets, *Proceedings of the National Academy of Sciences of the United States of America*, 113, 1516-1521, 10.1073/pnas.1508108113, 2016.

Ng, N. L., Brown, S. S., Archibald, A. T., Atlas, E., Cohen, R. C., Crowley, J. N., Day, D. A., Donahue, N. M., Fry, J. L., Fuchs, H., Griffin, R. J., Guzman, M. I., Herrmann, H., Hodzic, A., Iinuma, Y., Jimenez, J. L., Kiendler-Scharr, A., Lee, B. H., Luecken, D. J., Mao, J. Q., McLaren, R., Mutzel, A., Osthoff, H. D., Ouyang, B., Picquet-Varrault, B., Platt, U., Pye, H. O. T., Rudich, Y., Schwantes, R. H., Shiraiwa, M., Stutz, J., Thornton, J. A., Tilgner, A., Williams, B. J., and Zaveri, R. A.: Nitrate radicals and biogenic volatile organic compounds: oxidation, mechanisms, and organic aerosol, *Atmos. Chem. Phys.*, 17, 2103-2162, 10.5194/acp-17-2103-2017, 2017.

Pye, H. O. T., Luecken, D. J., Xu, L., Boyd, C. M., Ng, N. L., Baker, K. R., Ayres, B. R., Bash, J. O., Baumann, K., Carter, W. P. L., Edgerton, E., Fry, J. L., Hutzell, W. T., Schwede, D. B., and Shepson, P. B.: Modeling the Current and Future Roles of Particulate Organic

Nitrates in the Southeastern United States, *Environmental Science & Technology*, 49, 14195-14203, 10.1021/acs.est.5b03738, 2015.

Xu, L., Guo, H., Boyd, C. M., Klein, M., Bougiatioti, A., Cerully, K. M., Hite, J. R., Isaacman-VanWertz, G., Kreisberg, N. M., Knote, C., Olson, K., Koss, A., Goldstein, A. H., Hering, S. V., de Gouw, J., Baumann, K., Lee, S.-H., Nenes, A., Weber, R. J., and Ng, N. L.: Effects of anthropogenic emissions on aerosol formation from isoprene and monoterpenes in the southeastern United States, *Proceedings of the National Academy of Sciences of the United States of America*, 112, 37-42, 10.1073/pnas.1417609112, 2015a.

Xu, L., Suresh, S., Guo, H., Weber, R. J., and Ng, N. L.: Aerosol characterization over the southeastern United States using high-resolution aerosol mass spectrometry: spatial and seasonal variation of aerosol composition and sources with a focus on organic nitrates, *Atmos. Chem. Phys.*, 15, 7307-7336, 10.5194/acp-15-7307-2015, 2015b.

Zhang, H. F., Yee, L. D., Lee, B. H., Curtis, M. P., Worton, D. R., Isaacman-VanWertz, G., Offenberg, J. H., Lewandowski, M., Kleindienst, T. E., Beaver, M. R., Holder, A. L., Lonneman, W. A., Docherty, K. S., Jaoui, M., Pye, H. O. T., Hu, W. W., Day, D. A., Campuzano-Jost, P., Jimenez, J. L., Guo, H. Y., Weber, R. J., de Gouw, J., Koss, A. R., Edgerton, E. S., Brune, W., Mohr, C., Lopez-Hilfiker, F. D., Lutz, A., Kreisberg, N. M., Spielman, S. R., Hering, S. V., Wilson, K. R., Thornton, J. A., and Goldstein, A. H.: Monoterpenes are the largest source of summertime organic aerosol in the southeastern United States, *Proceedings of the National Academy of Sciences of the United States of America*, 115, 2038-2043, 10.1073/pnas.1717513115, 2018.

10. Referee comment: “*Line 395-399: Authors found that nitrate concentration increased after sunset and peaked at sunrise due to the formation of organic nitrates from the nighttime chemistry of nitrate and increased gas to particle partitioning of organic and inorganic nitrates due to the decrease in temperature. I do not agree to include the sentence that the result of organic nitrates will be discussed in a future publication. The conclusion stated in lines 396 and 397 does not make sense without the data of organic nitrates.*”

Author response: We agree with the referee that organic nitrate data is needed to explicitly explain the observed diurnal profile of NO_3^- mass concentration. This information has been added to the revised manuscript:

Page 14 line 432: The NO_3^- mass concentration measured by the HR-ToF-AMS is the nitrate functional group ($-\text{ONO}_2$) present on organic and inorganic nitrates. Hence, the diurnal profile of the NO_3^- mass concentration in Fig. 2 has contributions from both organic and inorganic nitrates. The mass concentrations of organic and inorganic nitrates increased after sunset and peaked at sunrise (Fig. S7), likely due to the formation of organic nitrates from nighttime NO_3 chemistry and increased gas-to-particle partitioning of organic and inorganic nitrates as temperature decreased (Xu et al., 2015a; Xu et al., 2015b). Quantification and characterization of organic nitrates based on HR-ToF-AMS and PILS-IC PM_{10} NO_3^- measurements will be discussed in a future publication.

References:

Xu, L., Guo, H., Boyd, C. M., Klein, M., Bougiatioti, A., Cerully, K. M., Hite, J. R., Isaacman-VanWertz, G., Kreisberg, N. M., Knote, C., Olson, K., Koss, A., Goldstein, A. H., Hering, S. V., de Gouw, J., Baumann, K., Lee, S.-H., Nenes, A., Weber, R. J., and Ng, N. L.: Effects of anthropogenic emissions on aerosol formation from isoprene and monoterpenes in the southeastern United States, *Proceedings of the National Academy of Sciences of the United States of America*, 112, 37-42, 10.1073/pnas.1417609112, 2015a.

Xu, L., Suresh, S., Guo, H., Weber, R. J., and Ng, N. L.: Aerosol characterization over the southeastern United States using high-resolution aerosol mass spectrometry: spatial and seasonal variation of aerosol composition and sources with a focus on organic nitrates, *Atmos. Chem. Phys.*, 15, 7307-7336, 10.5194/acp-15-7307-2015, 2015b.

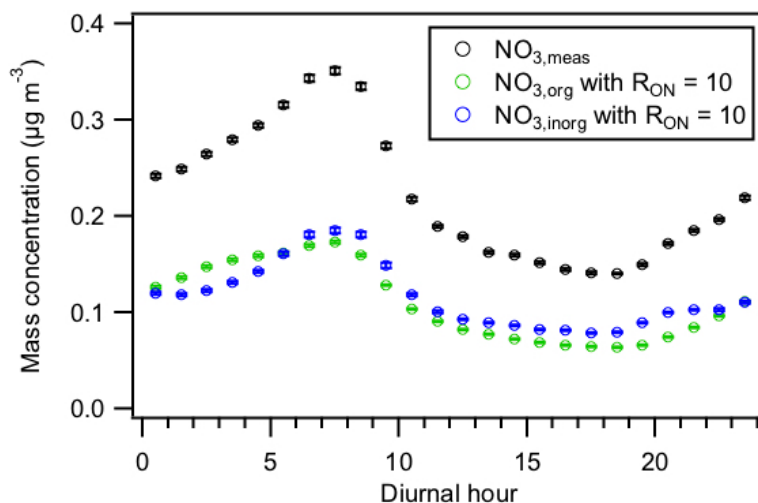


Figure S7: Diurnal profiles of the total nitrate functionality contributed by organic and inorganic nitrates ($\text{NO}_{3,\text{meas}}$), and the nitrate functionality solely from organic nitrates ($\text{NO}_{3,\text{org}}$) and inorganic nitrates ($\text{NO}_{3,\text{inorg}}$). $\text{NO}_{3,\text{org}}$ and $\text{NO}_{3,\text{inorg}}$ are estimated using the $\text{NO}^+/\text{NO}_2^+$ ratio method as described by Farmer et al. (2010) and Xu et al. (2015). Similar to Xu et al. (2015), we used a R_{ON} (defined here as the $\text{NO}^+/\text{NO}_2^+$ ratio for organic nitrates) value of 10 to calculate $\text{NO}_{3,\text{org}}$ and $\text{NO}_{3,\text{inorg}}$. All the data shown here represent averages in 1-hour intervals. Error bars shown are the standard errors.

References:

Farmer, D. K., Matsunaga, A., Docherty, K. S., Surratt, J. D., Seinfeld, J. H., Ziemann, P. J., and Jimenez, J. L.: Response of an aerosol mass spectrometer to organonitrates and organosulfates and implications for atmospheric chemistry, *Proceedings of the National Academy of Sciences of the United States of America*, 107, 6670-6675, 10.1073/pnas.0912340107, 2010.

Xu, L., Suresh, S., Guo, H., Weber, R. J., and Ng, N. L.: Aerosol characterization over the southeastern United States using high-resolution aerosol mass spectrometry: spatial and seasonal variation of aerosol composition and sources with a focus on organic nitrates, *Atmos. Chem. Phys.*, 15, 7307-7336, 10.5194/acp-15-7307-2015, 2015.

11. Referee comment: “Line 405: Which temperature and relative humidity data were used for ISORROPIA-II model inputs? Is it fixed temperature and RH values or temperature and RH observed during the campaign?”

Author response: Temperature and RH values measured during the campaign was used for ISORROPIA-II model inputs. This is clarified in the revised manuscript:

Page 15 line 460: “CIMS HNO₃ and NH₃ data, CE-corrected HR-ToF-AMS PM₁ SO₄²⁻ and NH₄⁺ data, PILS-IC PM₁ NO₃⁻ and non-volatile cation (Cl⁻, Na⁺, Ca²⁺, K⁺ and Mg²⁺) data, measured temperature and RH are used as ISORROPIA-II model inputs to predict PM₁ W_i and pH from 13 September to 6 October.”

12. Referee comment: “Line 433 and 435: What do authors mean by highly hygroscopic? Are that sulfate and nitrate alone contribute more to the hygroscopicity of aerosol particles or their salts play a role in the hygroscopic behavior of aerosol particles?”

Author response: We meant to write that aerosol inorganic sulfate and nitrate are hygroscopic species (i.e., their salts contribute to the hygroscopic behavior of aerosols). This is corrected in the revised manuscript:

Page 16 line 499: “Aerosol inorganic SO₄²⁻ and NO₃⁻ species are hygroscopic species.”

13. Referee comment: “Line 518-520: Which type of biogenic volatile organic compound precursors elevated at high temperature and produced a high amount of organic acids during warm and sunny days? Can you give some examples?”

Author response: Isoprene, which is the dominant BVOC in Yorkville, is one example of a BVOC precursor that is elevated at high temperature. We showed in a previous paper that the concentration of isoprene is moderately correlated with those of formic and acetic acids (R² = 0.42 and 0.40, respectively), which are known products of isoprene photooxidation (Nah et al., 2018). As requested, this information has been added into the revised manuscript:

Page 19 line 600: “For example, isoprene, which is the dominant BVOC in Yorkville, has a somewhat similar diurnal profile as the organic acids. In addition, the concentration of isoprene is moderately correlated with those of formic and acetic acids (Fig. S10 of Nah et al., 2018), which are known products of isoprene photooxidation.”

References:

Nah, T., Ji, Y., Tanner, D. J., Guo, H., Sullivan, A. P., Ng, N. L., Weber, R. J., and Huey, L. G.: Real-time measurements of gas-phase organic acids using SF₆- chemical ionization mass spectrometry, *Atmos. Meas. Tech. Discuss.*, 2018, 1-40, 10.5194/amt-2018-46, 2018.

14. Referee comment: “Line 539-542: Glutarate is a higher homologous diacid of oxalate that has almost similar sources and formation processes. What is the reason that oxalate as well as malonate and succinate peaked in the mid to late afternoon but glutarate peaked on the mid-morning? I do not agree with the authors explanation that they have different biogenic volatile organic compound precursors or different production mechanisms. What about the photodegradation of glutarate to lower carbon number diacids during the afternoon?”

Author response: The referee is correct in stating that the photodegradation of particle-phase glutaric acid may result in the formation of its successive homologues (i.e., oxalic, malonic and succinic acids) via C-C bond cleavage. Therefore, differences in the diurnal profiles of particle-phase oxalate, malonate, succinate and glutarate may also be due, in part, to organic aerosol photochemical aging. This information has been added to the revised manuscript:

Page 20 line 628: “Particle-phase oxalate, malonate and succinate peaked in the mid- to late afternoon, while glutarate generally peaked in the mid-morning. This suggests that while the production of these organic acids is photochemically-driven, they may have different BVOC precursors and/or different photochemical production pathways. In addition, since oxalic (C₂), malonic (C₃), succinic (C₄) and glutaric (C₅) acids belong to the same homologous series of organic diacids, it is possible that the photochemical aging of particle-phase glutaric acid resulted in the formation of its successive homologues via the cleavage of C-C bonds. Hence, organic aerosol photochemical aging may also have contributed to the diurnal profiles of particle-phase oxalate, malonate, succinate and glutarate.”

Additional revisions

1. We corrected the units of the duty cycles for the SF₆-CIMS and NH₃-CIMS:

Page 6 line 166: “The detection limits for HNO₃, SO₂ and the various organic acids measured by the SF₆-CIMS ranged from 1 to 60 ppt for 2.5 min integration periods, which corresponded to the length of a background measurement with a ~4 % duty cycle for each *m/z* (Table S1).”

Page 6 line 170: “The detection limit for NH₃ measured by the NH₃-CIMS was 1 ppb for 2.3 min integration periods, which corresponded to the length of a background measurement with a ~29 % duty cycle for the NH₄⁺ ion.”

2. We added another possible explanation for the disagreement between measured and modeled $\epsilon(\text{HCOO}^-)$ and $\epsilon(\text{CH}_3\text{CO}_2^-)$ in the revised manuscript:

Page 25 line 791: “In addition, formic and acetic acids may not be internally mixed with most of the other PM₁ aerosol components (e.g., SO₄²⁻, NO₃⁻, NH₄⁺, CH₃CO₂H), and thus are not associated with acidic aerosols, as assumed above. They may instead be associated with aerosols largely composed of non-volatile cations and have a pH closer to neutral. More research is needed to explain this disagreement.”

Characterization of Aerosol Composition, Aerosol Acidity and Organic Acid Partitioning at an Agriculture-Intensive Rural Southeastern U.S. Site

Theodora Nah,¹ Hongyu Guo,¹ Amy P. Sullivan,² Yunle Chen,¹ David J. Tanner,¹ Athanasios Nenes,^{1,3,4,5} Armistead Russell,⁶ Nga Lee Ng,^{1,3} L. Gregory Huey¹ and Rodney J. Weber^{1,*}

¹*School of Earth and Atmospheric Sciences, Georgia Institute of Technology, Atlanta, GA, USA*

²*Department of Atmospheric Science, Colorado State University, Fort Collins, CO, USA*

³*School of Chemical and Biomolecular Engineering, Georgia Institute of Technology, Atlanta, GA, USA*

⁴*ICE-HT, Foundation for Research and Technology, Hellas, 26504 Patras, Greece*

⁵*IERSD, National Observatory of Athens, P. Penteli, 15236, Athens, Greece*

⁶*School of Civil and Environmental Engineering, Georgia Institute of Technology, Atlanta, GA, USA*

* To whom correspondence should be addressed: rweber@eas.gatech.edu

Abstract

The implementation of stringent emission regulations has resulted in the decline of anthropogenic pollutants including sulfur dioxide (SO₂), nitrogen oxides (NO_x) and carbon monoxide (CO). In contrast, ammonia (NH₃) emissions are largely unregulated, with emissions projected to increase in the future. We present real-time aerosol and gas measurements from a field study conducted in an agricultural-intensive region in the southeastern U.S. during the fall of 2016 to investigate how NH₃ affects particle acidity and secondary organic aerosol (SOA) formation via the gas-particle partitioning of semi-volatile organic acids. Particle water and pH were determined using the ISORROPIA-II thermodynamic model and validated by comparing predicted inorganic HNO₃-NO₃⁻ and NH₃-NH₄⁺ gas-particle partitioning ratios with measured values. Our results showed that despite the high NH₃ concentrations (average 8.1 ± 5.2 ppb), PM₁ were highly acidic with pH values ranging from 0.9 to 3.8, and an average pH of 2.2 ± 0.6. PM₁ pH varied by approximately 1.4 units diurnally. Formic and acetic acids were the most abundant gas-phase organic acids, and oxalate was the most abundant particle-phase water-soluble organic acid anion. Measured particle-phase water-soluble organic acids were on average 6 % of the total non-refractory PM₁ organic aerosol mass. The measured molar fraction of oxalic acid in the particle phase (i.e., particle-phase oxalic acid molar concentration divided by the total oxalic acid molar concentration) ranged between 47 and 90 % for PM₁ pH 1.2 to 3.4. The measured oxalic acid gas-particle partitioning ratios were in good agreement with their corresponding thermodynamic predictions, calculated based on oxalic acid's physicochemical properties, ambient temperature, particle water and pH. In contrast, gas-particle partitioning of formic and acetic acids were not well predicted for reasons

Deleted: study average

Deleted: study-

Deleted: d

currently unknown. For this study, higher NH_3 concentrations relative to what has been measured in the region in previous studies had minor effects on PM_{10} organic acids and their influence on the overall organic aerosol and PM_{10} mass concentrations.

1. Introduction

Ammonia (NH_3) is the most abundant basic gas in the troposphere and plays an important role in many atmospheric processes. It is a major neutralizer of atmospheric acidic species, reacting readily with sulfuric acid (H_2SO_4) and nitric acid (HNO_3) to form ammonium sulfate and nitrate salts (e.g., $(\text{NH}_4)_2\text{SO}_4$, and other forms such as NH_4HSO_4 , $(\text{NH}_4)_3\text{H}(\text{SO}_4)_2$, and NH_4NO_3), which are often the main inorganic components of atmospheric aerosols. The formation of particle-phase ammonium sulfate and nitrate salts in the aerosol phase depends on the thermodynamic states of their precursors and the environmental conditions, which can consequently affect aerosol pH. For example, Guo et al. (2017b) showed that for Southeast U.S. summertime conditions, as aerosol pH increases, the relative fractions of SO_4^{2-} and HSO_4^- increases and decreases, respectively. Wet and dry deposition are the principle NH_3 sinks (Dentener and Crutzen, 1994). NH_3 is spatially heterogeneous, with the highest concentrations typically found near emission sources (Seinfeld and Pandis, 2016). The dominant NH_3 sources in rural areas are agricultural in nature, and include the application of fertilizers and volatilization of livestock waste (Reis et al., 2009; Ellis et al., 2013; Van Damme et al., 2014). Biomass burning, either from wildfires or from controlled burning during land-clearing operations, is also a significant source of NH_3 in rural environments. The primary source of NH_3 in urban areas are industrial emissions (e.g., NH_3 synthesis, manufacture of ammonium nitrate and urea, fluid and thermal catalytic cracking processes in petroleum refinery), though vehicular emissions can be a significant NH_3 source in some heavily populated cities (Reis et al., 2009; Lamarque et al., 2010; Yao et al., 2013; Sun et al., 2017). Vehicular NH_3 emissions are thought to be produced primarily from the reaction of nitrogen oxide with hydrogen in the presence of carbon monoxide in three-way catalysts of gasoline light duty vehicles (Barbier-Jr and Duprez, 1994; Whittington et al., 1995; Livingston et al., 2009; Suarez-Bertoa et al., 2014).

In the US, implementation of stringent emission controls on traditional anthropogenic air pollutants, such as sulfur dioxide (SO_2), nitrogen oxides (NO_x) and carbon monoxide (CO), have led to steady decreases in their emissions, and consequently their concentrations (Blanchard et al., 2013b; Xing et al., 2013). In contrast, NH_3 emissions are largely unregulated, and are projected to

increase due to increased agricultural operations to feed a growing world population (Reis et al., 2009; Ellis et al., 2013). Satellite observations showed that gas-phase NH_3 concentrations have increased substantially in US agricultural areas from 2002 to 2014 (Warner et al., 2017). More wildfires from a changing climate, or from controlled burning for land clearing for agricultural use, may also lead to increased NH_3 emissions (Reis et al., 2009; Pechony and Shindell, 2010; Warner et al., 2016). These trends suggest that NH_3 could play an increasingly important role in atmospheric chemistry.

Previous laboratory studies have shown that NH_3 can influence secondary organic aerosol (SOA) formation and processing. For example, NH_3 increases SOA mass yields in the α -pinene ozonolysis system, and is hypothesized to be due to the formation of ammonium salts from the reaction of NH_3 with organic acids (Na et al., 2007). The heterogeneous uptake of NH_3 by SOA can also lead to the formation of particulate organonitrogen compounds, a class of brown carbon species that can reduce visibility and impact climate (Laskin et al., 2010; Updyke et al., 2012; Lee et al., 2013; Laskin et al., 2015).

The southeastern U.S. is a natural outdoor laboratory for studying the effects of biogenic-anthropogenic interactions on atmospheric aerosol formation and processing. Subtropical vegetation composed mainly of mixed conifer and deciduous forests emit large quantities of biogenic volatile organic compounds (BVOCs) that can act as precursors for SOA formation (Blanchard et al., 2011; Guenther et al., 2012; Blanchard et al., 2013a). Large urban centers and small towns are surrounded by large expanses of forests and widespread rural areas with agricultural activities. Scattered within the southeastern U.S. are also coal-burning power plants and industrial facilities. Anthropogenic activities in this region emit large concentrations of VOCs, SO_2 , NO_x , CO, NH_3 and aerosols (Blanchard et al., 2013c). Similar to other parts of the U.S., SO_2 , CO and NO_x concentrations have decreased steadily in the southeastern U.S. due to the implementation of emission controls (Blanchard et al., 2013b). In contrast, gas-phase NH_3 concentrations have increased in the southeastern U.S. over the same time period (Saylor et al., 2015). These factors make the southeastern U.S. an intriguing place to study the influence of NH_3 on atmospheric aerosol chemistry.

We performed aerosol and gas measurements during a field study conducted in Yorkville, Georgia, U.S., in the fall of 2016, with the goal of understanding how NH_3 affects aerosol acidity

100 and SOA formation. The field site is surrounded by forest and agricultural land, affording an
101 opportunity to make ambient observations in an area impacted by local emissions of BVOCs and
102 NH_3 . In this paper, we present gas and aerosol composition measurements that includes a suite of
103 organic acids. The thermodynamic equilibrium model, ISORROPIA-II, is used to calculate particle
104 water and pH based on measured inorganic aerosol and gas composition (Nenes et al., 1998;
105 Fountoukis and Nenes, 2007), and these predictions are compared to observed gas-particle
106 partitioning of NH_3 , HNO_3 and organic acids. Together, these measurements are used to determine
107 how aerosol acidity affects the mass concentration of particle-phase organic acids at this site.

108 **2. Methods**

109 **2.1. Field site**

110 Aerosol and gas measurements were conducted at the Yorkville, Georgia (33.929 N,
111 85.046 W) SouthEastern Aerosol Research and Characterization (SEARCH) field site from mid-
112 August to mid-October 2016. This is one of the sampling sites for the Southeastern Center for Air
113 Pollution and Epidemiology (SCAPE) study where aerosol characterization measurements were
114 conducted in the summer and winter of 2012 (Xu et al., 2015a; Xu et al., 2015b). A detailed
115 description of the field site can be found in Hansen et al. (2003). This rural site is situated in a
116 mixed forest-agriculture area approximately 55 km northwest and generally upwind of Atlanta.
117 The immediate surrounding area is used for cattle grazing and poultry concentrated animal feeding
118 operations (CAFOs) (Fig. S1). There are no major roads near the field site and nearby traffic
119 emissions were negligible. A large coal-fired power plant (Plant Bowen) is situated approximately
120 25 km north of the site. Hence, the field site is impacted mainly by BVOC and NH_3 emissions,
121 with occasional spikes in SO_2 and minimal influence from urban anthropogenic pollutants such as
122 HNO_3 , O_3 , NO_x and CO (Fig. S2). The sampling period was characterized by moderate
123 temperatures (24.0 °C average, 32.6 °C max, 9.5 °C min) and high relative humidities (68.9 % RH
124 average, 100 % RH max, 21.6 % RH min). Meteorological data are shown in Fig. S3. Data reported
125 are displayed in eastern daylight time (EDT).

126 **2.2. Instrumentation**

127 Instruments were housed in a temperature controlled (~20 °C) trailer during the field study.
128 Gas-phase HNO_3 , SO_2 and organic acids (formic, acetic, oxalic, butyric, glycolic, propionic,

129 valeric, malonic and succinic acids) were measured by a custom-built chemical ionization mass
130 spectrometer (CIMS) using sulfur hexafluoride ions (SF_6^-) as reagent ions. SO_2 and HNO_3 were
131 detected as fluoride adducts (F_2SO_2^- and $\text{NO}_3 \cdot \text{HF}$, respectively) while the organic acids (HX) were
132 detected primarily as conjugated anions (X^-) by the quadrupole mass spectrometer (Huey et al.,
133 1995; Huey et al., 2004; Nah et al., 2018). This CIMS is referred hereafter as the SF_6 -CIMS. Gas-
134 phase NH_3 was measured by an additional custom-built CIMS using protonated ethanol clusters
135 ($(\text{C}_2\text{H}_5\text{OH})_n^+$) as reagent ions. NH_3 was detected primarily as NH_4^+ ions by the quadrupole mass
136 spectrometer (Nowak et al., 2002; Yu and Lee, 2012; You et al., 2014a). This CIMS is referred
137 hereafter as the NH_3 -CIMS.

138 Since HNO_3 , NH_3 and organic acids may condense on surfaces, both SF_6 -CIMS and NH_3 -
139 CIMS used inlet configurations that minimized wall interactions (Huey et al., 2004; Nowak et al.,
140 2006). Each CIMS was connected to an inlet (a 7.6 cm ID aluminum pipe) that protruded beyond
141 the trailer's wall by ~40 cm into the ambient air. Both inlets were ~2 m above the ground. A donut-
142 shaped ring was attached to the ambient sampling port of each pipe to curtail the influence of
143 crosswinds on the pipe's flow dynamics. Both rings were wrapped with a fine wire mesh to prevent
144 ingestion of insects. A flow of ~2800 L min^{-1} was maintained in each pipe using regenerative
145 blowers (AMETEK Windjammer 116637-03). Part of this flow (7 L min^{-1} for the SF_6 -CIMS and
146 4.6 L min^{-1} for the NH_3 -CIMS) was sampled through a custom-made three-way PFA Teflon valve,
147 which connected the pipe's center to the CIMS sampling orifice and could be switched
148 automatically between ambient and background measurements.

149 Background measurements were performed every 25 min for 4 min for both the SF_6 -CIMS
150 and NH_3 -CIMS. During each background measurement, the sampled air flow was passed through
151 an activated charcoal scrubber (Sigma Aldrich) that removed SO_2 , HNO_3 and organic acids prior
152 to delivery into the SF_6 -CIMS, and through a silicon phosphate scrubber (Perma Pure Inc.) that
153 removed NH_3 prior to delivery into the NH_3 -CIMS. > 99 % of the targeted species were removed
154 during background measurements for both the SF_6 -CIMS and NH_3 -CIMS. Standard addition
155 calibrations were performed every 5 h for the SF_6 -CIMS using the outputs of a 1.12 ppm $^{34}\text{SO}_2$
156 gas cylinder (Scott-Marrin Inc.) and a formic or acetic acid permeation device (VICI Metronics).
157 Calibrations for the other gases measured by the SF_6 -CIMS were performed in post-field
158 laboratory work, details of which can be found in Nah et al. (2018) and SI section S1. Standard

159 addition calibrations were performed hourly for the NH₃-CIMS using the output of a NH₃
160 permeation device (KIN-TEK). The outputs of the formic and acetic acid permeation devices were
161 measured periodically by scrubbing the output of the permeation tube in deionized water, followed
162 by ion chromatography analysis for formate and acetate. The emission rate of the NH₃ permeation
163 device was measured using UV optical absorption (Neuman et al., 2003).

164 The detection limits for species measured by the SF₆-CIMS and NH₃-CIMS were
165 approximated from 3 times the standard deviation values (3 σ) of the ion signals measured during
166 background mode. The detection limits for HNO₃, SO₂ and the various organic acids measured by
167 the SF₆-CIMS ranged from 1 to 60 ppt for 2.5 min integration periods, which corresponded to the
168 length of a background measurement with a ~~~4 %~~ duty cycle for each *m/z* (Table S1). Measurement
169 uncertainties for the concentrations of HNO₃, SO₂ and the various organic acids originate mainly
170 from calibration measurements, and were between 12 and 25 % (Table S1). The detection limit for
171 NH₃ measured by the NH₃-CIMS was 1 ppb for 2.3 min integration periods, which corresponded
172 to the length of a background measurement with a ~~~29 %~~ duty cycle for the NH₄⁺ ion.
173 Measurement uncertainties for NH₃ concentrations were 13 %.

174 A high-resolution time-of-flight aerosol mass spectrometer (HR-ToF-AMS, Aerodyne
175 Research Inc.) was used to measure the elemental composition of ambient non-refractory PM₁
176 (particles with aerodynamic diameters < 1 μ m). Ambient air was sampled at 16.7 L min⁻¹ through
177 a URG PM₁ cyclone and then through a nafion dryer prior to delivery into the HR-ToF-AMS.
178 Aerosols were dried to RH < 20 % to eliminate the influence of RH on the HR-ToF-AMS's particle
179 collection efficiency. A detailed description of the HR-ToF-AMS can be found in the literature
180 (DeCarlo et al., 2006; Canagaratna et al., 2007; Canagaratna et al., 2015). Briefly, the aerodynamic
181 lens of the HR-ToF-AMS focused the dried submicron aerosols into a narrow beam. The aerosols
182 were then impacted onto a heated tungsten surface (~600 °C) where they were flash vaporized.
183 The resulting vapors were ionized by electron impact ionization (70 eV), and the ions were
184 detected by a time-of-flight mass spectrometer. Gas-phase interferences were accounted for by
185 subtracting the signals obtained during daily measurements of filtered, particle-free sampling air.
186 Ionization efficiency calibrations were performed weekly using 300 nm ammonium nitrate and
187 ammonium sulfate particles. Composition-dependent collection efficiency (CDCE) values of 0.44
188 to 0.55 were determined using the procedure detailed by Middlebrook et al. (2012), where CDCE

Deleted: 0.0

Deleted: s

Deleted: 0.

Deleted: s

Deleted: ies

Deleted: applied to the data

values are derived based largely on aerosol inorganic species concentrations and the relative humidity in the sampling line. In addition, a constant collection efficiency (CE) value of 0.9 was determined from the comparison of raw HR-ToF-AMS SO_4^{2-} data with other particulate SO_4^{2-} measurements performed during the study. Comparisons of aerosol mass concentrations obtained from the application of CDCE values (i.e., 0.44 to 0.55) vs. a constant CE value (i.e., 0.9) to the raw HR-ToF-AMS data are discussed in section 3.2. Uncertainties in HR-ToF-AMS measurements were estimated to be approximately 25 % (Canagaratna et al., 2007).

Particle-phase water-soluble organic acids, inorganic cations and anions were measured using two Particle-into-Liquid Sampler (PILS) systems coupled to ion chromatographs (ICs) (Orsini et al., 2003). Each PILS sampled ambient air at nominally 16.7 L min^{-1} through a URG PM_{10} cyclone. Before PILS1, which was used to measure water-soluble inorganic cation and anions, two long (24 cm) URG glass annular denuders coated with sodium carbonate and phosphorous acid were used to remove acidic and basic gases. Before PILS2, which measured water-soluble organic acids, a 28 cm parallel plate carbon denuder (Sunset Lab) was used to remove organic gases (Eatough et al., 1993). In each PILS, aerosols were mixed with water vapor at $\sim 100^\circ\text{C}$ generated from heated ultrapure deionized water (Weber et al., 2001; Orsini et al., 2003). The resulting droplets were impacted onto a plate, with the resulting liquid sample analyzed by ICs. Each IC system was calibrated at the beginning and end of the study using five multi-compound standards in order to create calibration curves. Periodically, a HEPA filter (Pall Life Sciences) was placed on the inlet to determine the background in near real-time. The measurement uncertainty for each IC system was about 10 %.

PILS1 was connected to two Dionex ICS-1500 ICs (Thermo Fisher Scientific) to measure the water-soluble inorganic ions. These two IC systems include an isocratic pump, self-regenerating anion or cation suppressor, and conductivity detector. This system will be referred hereafter as the PILS-IC. Anions were separated using a Dionex IonPac AS15 guard and analytical column (4 x 250 mm, Thermo Fisher Scientific) employing an eluent of 38 mM sodium hydroxide at a flow rate of 1.5 mL min^{-1} . Cations were separated using a Dionex IonPac CS12A guard and analytical column (4 x 250 mm, Thermo Fisher Scientific) employing an eluent of 18 mM methanesulfonic acid at a flow rate of 1 mL min^{-1} . A new chromatogram was obtained every 30

224 min with a sample loop fill time (i.e., ambient sample integration time) of 20 min. The limit of
225 detection for the various anions and cations was approximately $0.01 \mu\text{g m}^{-3}$.

226 PILS2 was coupled to a Dionex ICS-4000 capillary high-pressure ion chromatography
227 (HPIC) system to measure the water-soluble organic acids. The HPIC includes an eluent generator,
228 isocratic pump, degasser, suppressor, carbonate removal device, and conductivity detector. This
229 system will be referred hereafter as the PILS-HPIC. The organic acids were separated using a
230 Dionex AS11-HC-4 μm capillary guard and analytical column (0.4 x 250mm, Thermo Fisher
231 Scientific), which used a potassium hydroxide gradient separation method at a flow rate of 0.015
232 mL min^{-1} . A new chromatogram was obtained every 60 min with a sample loop fill time of 2 min.
233 The limit of detection for the various organic acids was approximately $0.001 \mu\text{g m}^{-3}$.

234 Particle- and gas-phase water-soluble organic carbon (WSOC_p and WSOC_g , respectively)
235 were measured using two Sievers 900 series total organic carbon (TOC) analyzers (GE Analytical
236 Instruments), as described by Sullivan et al. (2004). For WSOC_p measurements, ambient air was
237 sampled at 15.2 L min^{-1} through a URG PM_{10} cyclone and a parallel plate carbon denuder into a
238 PILS coupled to the first TOC analyzer. For WSOC_g measurements, ambient air was sampled at
239 20 L min^{-1} through a Teflon filter (45 mm diameter, 2.0 μm pore size, Pall Life Sciences) to remove
240 particles in the air stream. This filter was changed every 3 to 4 days. The particle-free air was then
241 directed to a MIST chamber filled with ultrapure deionized water, which scrubbed the soluble
242 gases at an air flow rate of 20 L min^{-1} . Soluble gases with Henry's law constants greater than 10^3
243 $\text{mole L}^{-1} \text{ atm}^{-1}$ were scrubbed into deionized water in the MIST chamber (Spaulding et al., 2002).
244 The resulting MIST chamber liquid sample was analyzed by the second TOC analyzer. The TOC
245 analyzers converted the organic carbon in the liquid samples to carbon dioxide using UV radiation
246 and chemical oxidation. The carbon dioxide formed was then measured by conductivity. The
247 amount of organic carbon in the liquid samples is proportional to the measured increase in
248 conductivity of the dissolved carbon dioxide. Each WSOC_p and WSOC_g measurement lasted 4
249 min. Background WSOC_p and WSOC_g measurements were performed for 45 min every 12 h by
250 stopping the sample air flow and rinsing the system with deionized water. Both TOC analyzers
251 were calibrated at the beginning and end of the study using varying concentrations of sucrose
252 solutions to create calibration curves (as specified by the instrument manual). The limit of
253 detections for WSOC_p and WSOC_g were 0.2 and $0.4 \mu\text{gC m}^{-3}$, respectively. The measurement

uncertainties for WSOC_p and WSOC_g were estimated to be 10 % based on uncertainties in the TOC analyzer, sample air and liquid flows.

A suite of instruments operated by the SEARCH network provided supporting gas and aerosol measurements (Hansen et al., 2003; Edgerton et al., 2005, 2006). O₃ was measured by a UV absorption instrument (Thermo Fisher Scientific) with a temporal resolution of 1 min. NO and NO_x were measured by a chemiluminescence instrument (Thermo Fisher Scientific) with a temporal resolution of 1 min. NO₂ was obtained from the difference between NO and NO_x. CO was measured by a non-dispersive infrared absorption instrument (Thermo Fisher Scientific) with a temporal resolution of 1 min. NH₃ was measured by a denuder-based instrument (ARA) with a temporal resolution of 5 min. Comparisons of measurements by the NH₃-CIMS and denuder-based instrument will be presented in section 3.1. A filter-based particle composition monitor (ARA) provided 24 h-integrated PM_{2.5} measurements of particle mass and major inorganic ions measured offline by ion chromatography. Organic carbon (OC) and elemental carbon (EC) in PM_{2.5} were measured by a OCEC Analyzer (Sunset Labs) with a temporal resolution of 1 h. This analyzer determined OC by thermal optical transmittance. VOCs were measured by a gas chromatography-flame ionization detector (GC-FID, Agilent Technologies) with a temporal resolution of 1h.

2.2. Particle pH and water calculation

The thermodynamic equilibrium model ISORROPIA-II was used to determine the phase state and composition of an NH₄⁺-SO₄²⁻-NO₃⁻-Cl⁻-Na⁺-Ca²⁺-K⁺-Mg²⁺-water inorganic aerosol in equilibrium with its corresponding gas-phase species (Fountoukis and Nenes, 2007; Nenes et al., 1998). This approach was used in previous studies to determine particle water and pH in different parts of the world (Guo et al., 2015; Bougiatioti et al., 2016; Guo et al., 2016; Weber et al., 2016; Guo et al., 2017a; Guo et al., 2017c; Shi et al., 2017). The pH of an aqueous solution is defined as the negative logarithm of the hydronium ion (H₃O⁺) activity on a molality basis (www.goldbook.iupac.org/html/P/P04524.html, last access: 6 July 2018):

$$pH = -\log_{10}[a(H^+)] = -\log_{10}[m(H^+)\gamma_m(H^+)/m^\theta] \quad (1a)$$

where $a(H^+)$ is the hydronium ion activity in an aqueous solution, $m(H^+)$ is the hydronium ion molality, $\gamma_m(H^+)$ is the molality-based hydronium ion activity coefficient, and m^θ is the standard molality (1 mol kg⁻¹). For simplicity, H₃O⁺ is denoted here as H⁺ even though we recognize that

Formatted: Line spacing: 1.5 lines

Deleted: the negative logarithm of the hydronium ion (H₃O⁺) activity in an aqueous solution.

the unhydrated hydrogen ion is rare in aqueous solutions. Since most thermodynamic equilibrium models (e.g., ISORROPIA-II, E-AIM) report species in terms of concentration per volume of air (e.g., $\mu\text{g m}^{-3}$, $\mu\text{mol m}^{-3}$), the particle pH can be calculated as:

$$\text{pH} = -\log_{10} \gamma_{H^+} H_{aq}^+ = -\log_{10} \frac{1000 \gamma_{H^+} H_{air}^+}{W_i + W_o} \cong -\log_{10} \frac{1000 \gamma_{H^+} H_{air}^+}{W_i} \quad (1b)$$

where γ_{H^+} is the molarity-based hydronium ion activity coefficient (assumed to be 1), H_{aq}^+ (mole L^{-1}) is the molar concentration of hydronium ions in particle water (i.e., pH is calculated in terms of molarity), H_{air}^+ ($\mu\text{g m}^{-3}$) is the hydronium ion concentration per volume of air, and W_i and W_o ($\mu\text{g m}^{-3}$) are the bulk particle water concentrations associated with inorganic and organic species per volume of air, respectively. In equation 1b, the molecular weight of H^+ is taken as 1 g mole^{-1} , and 1000 is the factor needed for unit conversion of g L^{-1} to $\mu\text{g m}^{-3}$. H_{air}^+ and W_i are outputs of the ISORROPIA-II model. Previous studies have shown that particle pH values predicted using only W_i are reasonably accurate since the sensitivity of particle pH to the effects of W_o is small (Guo et al., 2015). For the southeastern U.S., Guo et al. (2015) reported that particle pH values predicted using only W_i were systematically 0.15 to 0.23 units lower than those predicted using $W_i + W_o$ during the 2013 Southern Oxidant Aerosol Study (SOAS) and SCAPE campaigns. Given this small deviation and that organic aerosol hygroscopicity was not measured in this field study, we report particle pH only considering W_i .

ISORROPIA-II was run in “forward” mode, which assumes that aerosols are “metastable” with no solid precipitates, to predict particle pH and the partitioning of semi-volatile compounds. In “forward” mode, the model calculates the gas-particle equilibrium partitioning concentrations based on the input of the total concentration of a species (i.e., gas + particle). In “reverse” mode, the model calculates the gas-particle equilibrium partitioning concentrations based on the input of only the particle-phase concentration of a species. We used “forward” mode because the “reverse” mode is sensitive to measurement errors, which often result in large model biases in the predicted particle pH (Hennigan et al., 2015). The measured particle-phase inorganic NH_4^+ , SO_4^{2-} and NO_3^- concentrations and gas-phase HNO_3 and NH_3 concentrations were used as model inputs. The “metastable” assumption is reasonable since the high RH (average RH 68.9 %) observed during the study indicated that the aerosols had likely deliquesced. We excluded data for periods where

Deleted: The

Deleted: is

Deleted: defined

314 the RH was above 95 % since the exponential growth in particle liquid water with RH introduces
315 large pH uncertainties (Malm and Day, 2001; Guo et al., 2015).

316 In using ISORROPIA-II to predict particle pH and the partitioning of semi-volatile
317 compounds, we also assumed that the aerosols are internally mixed and that the particle pH does
318 not change with particle size (i.e., the overall particle pH is characterized by the particle's bulk
319 properties). As long as some small fraction of sulfate is mixed with various aerosol components,
320 (e.g., non-volatile cations), the assumption that aerosols are completely internally mixed has a
321 small effect on the predicted pH (Guo et al., 2017b). However, the presence of multiple organic
322 and inorganic species in ambient aerosols may lead to multiple phases within the particle (i.e.,
323 phase separation). Consequently, this may result in the unequal distribution of inorganic species
324 among different phases, each with its own water activity and inorganic concentration. Previous
325 studies have shown that liquid-liquid and solid-liquid phase separations may occur for mixed
326 organic and inorganic aerosols at low RH and organic aerosol oxygen-to-carbon atomic ratios
327 (O/C) (Bertram et al., 2011; Song et al., 2012; You et al., 2013; You et al., 2014b; You and
328 Bertram, 2015). Phase separations were always observed at $O/C \leq 0.5$, while no phase separation
329 was observed at $O/C \geq 0.8$. The probability for the occurrence of phase separation decreased at
330 higher RH for $0.5 < O/C < 0.8$. The average O/C for this field study is 0.69 ± 0.06 . Organic acids
331 were not included in the calculation of particle pH. This is reasonable since their total mass
332 concentration was small compared to the total inorganic mass concentration. The ~~average~~ ratio of
333 the organic acid mass concentration to the inorganic mass concentration is 0.25. Furthermore, Song
334 et al. (2018) showed that including organic acid mass concentrations in thermodynamic model
335 calculations had minor effects on particle pH if the system is in equilibrium. The validity of these
336 assumptions and the resulting thermodynamic model predictions will be evaluated by comparing
337 the predicted gas-particle partitioning ratios of semi-volatile inorganic compounds with measured
338 values in section 3.3.

Deleted: study-averaged

339 3. Results and Discussion

340 3.1. NH₃ observations

341 Continuous measurements of NH₃ were made using the NH₃-CIMS from 13 September to
342 12 October. Figures 1a and 1b show the time series and ~~average~~ diurnal profile of NH₃.

Deleted: study-averaged

345 respectively. NH_3 concentrations ranged from 0.7 to 39.0 ppb (0.5 to $28.5 \mu\text{g m}^{-3}$), and exhibited
346 consistent diurnal cycles. NH_3 was generally higher in the late mornings and early afternoons.
347 Concentrations started to increase at 07:30, which coincided with an increase in temperature at
348 sunrise (Fig. S3). Possible reasons for the morning increase include volatilization of particulate
349 ammonium and animal waste, entrainment from the residual layer where NH_3 may not have been
350 depleted, evaporation of dew or fog that contained dissolved NH_3 , and emission from plant stomata
351 (Ellis et al., 2011). NH_3 decreased at 14:30, approximately 1 hour before temperature decreased,
352 and may be due to changes in the boundary layer height. However, this hypothesis cannot be tested
353 since the boundary layer height was not measured during the study. The diurnal plot does not
354 account for dilution as the boundary layer expanded, and only indicates that if emissions were
355 solely from the surface and lower concentrations aloft, these NH_3 sources were of significant
356 magnitude.

357 The average NH_3 concentration measured by the NH_3 -CIMS is 8.1 ± 5.2 ppb. This is
358 approximately 2 times higher than the average NH_3 concentration (3.8 ± 2.9 ppb) measured by the
359 denuder-based instrument operated by the SEARCH network over the same time period (Fig. S4).
360 Differences in NH_3 concentrations measured by the two instruments may be due to positive and
361 negative sampling artifacts caused by differences in sampling inlets (e.g., inlet length and
362 location), frequency of calibration and background measurements, and (in the case of the denuder-
363 based instrument) possible sample contamination during chemical analysis. Discussions on how
364 differences in measured NH_3 concentrations affect PM_{10} pH predictions will be presented in section
365 3.3. Nevertheless, there is a record of NH_3 concentrations measured by the denuder-based
366 instrument at this site since 2008. Just prior to, and during this study, NH_3 concentrations are
367 generally the highest observed since 2011 (Fig. S5). These elevated NH_3 concentrations may be
368 due to sporadic biomass burning episodes caused by elevated temperatures and widespread
369 drought across the southeastern U.S. in 2016 (Park Williams et al., 2017; Case and Zavodsky,
370 2018).

371 The NH_3 -CIMS measurements are examined with the meteorological data to gain insights
372 on the primary NH_3 sources during the sampling period. To account for wind speed, the 1-hour
373 averaged NH_3 concentrations are first multiplied by their corresponding 1-hour averaged wind
374 speeds. These normalized NH_3 concentrations are then used to construct a wind direction polar

375 plot showing the average normalized NH_3 concentration per 10 degrees bin (Fig. 1c). The wind
376 direction polar plot shows that the normalized NH_3 is approximately 2 times greater than the
377 average when air masses are transported from the south-east, the general direction of the poultry
378 CAFOs located approximately 2 km from the field site (Fig. S1), which are known for high NH_3
379 emissions. This conclusion is reaffirmed by NH_3 measurements by the SEARCH network's
380 denuder-based instrument.

381 NH_3 concentrations measured by the two instruments in this study are substantially higher
382 than those measured in three recent field studies conducted in the continental U.S.: 2010 California
383 Nexus (CalNex) study, 2013 Southeast Nexus (SENEX) study and 2013 SOAS study (see Table
384 1). The differences in NH_3 may be attributed to differences in land use, proximity to CAFOs and
385 meteorological conditions. The high NH_3 concentrations in this study allow us to make ambient
386 observations of the effect of NH_3 on particle acidity and the gas-particle partitioning of semi-
387 volatile inorganic and organic compounds, and compare them with previous studies.

388 3.2. PM_{10} composition

389 The aerosol inorganic chemical composition was measured by several instruments during
390 this study. The HR-ToF-AMS, PILS-IC and PILS-HPIC measured the composition of PM_{10} , while
391 a filter-based particle composition monitor measured the composition of $\text{PM}_{2.5}$. Comparisons of
392 aerosol SO_4^{2-} , NO_3^- and NH_4^+ mass concentrations obtained from the application of CDCE values
393 to the raw HR-ToF-AMS data are compared to those measured by the other three instruments in
394 Fig. S6. NH_4^+ measurements by the PILS-IC are not available for comparison due to denuder
395 breakthrough that occurred during the study.

396 SO_4^{2-} measurements by the various instruments are generally well correlated with each
397 other, with R^2 values ranging from 0.64 to 0.92. Although PM_{10} SO_4^{2-} measurements by the two
398 PILS systems show good agreement with each other, HR-ToF-AMS CDCE-applied SO_4^{2-}
399 measurements are approximately two times higher than the PILS and filter measurements. Similar
400 systematic differences are also observed for NO_3^- and NH_4^+ measurements. NO_3^- and NH_4^+
401 measurements by the four instruments are moderately correlated ($R^2 = 0.54$ to 0.79 and $R^2 = 0.94$,
402 respectively). NO_3^- measurements by the PILS and filter systems are mostly similar; however, HR-
403 ToF-AMS CDCE-applied PM_{10} NO_3^- and NH_4^+ measurements are approximately three times and

Deleted: these four

Deleted: are summarized

two times higher than the PILS and filter measurements. One possible reason is that the calculated CDCE is lower due to organics dominating the aerosol composition during the study (average of 74.2 ± 7.9 % of the non-refractory PM₁ mass concentration). Lee et al. (2015) suggested that a high organic mass fraction may impede the complete efflorescence of aerosols when they are passed through the drier prior to delivery into the HR-ToF-AMS, thus reducing the particle bounce and increasing the CE value. Hence, we estimated HR-ToF-AMS PM₁ mass concentrations that would be consistent with PILS and filter measurements by multiplying all the raw HR-ToF-AMS data by a constant CE value of 0.9, which was obtained from comparisons of the raw HR-ToF-AMS SO₄²⁻ data with PILS-IC and PILS-HPIC SO₄²⁻ measurements. The constant CE-applied HR-ToF-AMS data is used in all our subsequent analyses.

Figure 2 shows the time series and average diurnal profiles of non-refractory PM₁ species. The average non-refractory PM₁ organics, SO₄²⁻, NO₃⁻ and NH₄⁺ mass concentrations are 5.0 ± 2.3 , 1.6 ± 0.4 , 0.2 ± 0.1 and 0.4 ± 0.2 $\mu\text{g m}^{-3}$, respectively. Organics are the dominant non-refractory PM₁ species, accounting for 74.2 ± 7.9 % of the non-refractory PM₁ mass concentration during the field study. Organic aerosol mass concentration was slightly higher at night, which is likely caused by changes in the boundary layer height, emission sources and SOA formation processes (Xu et al., 2015b). Previous studies have shown that nighttime SOA production in the Southeastern U.S. is largely attributed to nitrate radical oxidation and ozonolysis of monoterpenes, which are abundant at night (Pye et al., 2015; Xu et al., 2015a; Xu et al., 2015b; Lee et al., 2016; Zhang et al., 2018). Specifically, the nitrate radical oxidation of some monoterpenes (e.g., β -pinene) could form low volatility organic nitrates that are condensable and could contribute substantially to the nocturnal organic aerosol mass (Boyd et al., 2015; Boyd et al., 2017; Ng et al., 2017). Apportionment of organic aerosol sources will be discussed in an upcoming publication. SO₄²⁻ is the second most abundant non-refractory PM₁ species (16.3 ± 5.7 % mass fraction), followed by NH₄⁺ (5.9 ± 2 % mass fraction) and NO₃⁻ (3.6 ± 2.2 % mass fraction). SO₄²⁻ mass concentration peaked in the afternoon due to enhanced SO₂ photooxidation (Weber et al., 2003). The NO₃⁻ mass concentration measured by the HR-ToF-AMS is the nitrate functional group (-ONO₂) present on organic and inorganic nitrates. Hence, the diurnal profile of the NO₃⁻ mass concentration in Fig. 2 has contributions from both organic and inorganic nitrates. The mass concentrations of organic and inorganic nitrates increased after sunset and peaked at sunrise (Fig. S7), likely due to the formation of organic nitrates from nighttime NO₃ chemistry and increased

Deleted: Although the higher HR-ToF-AMS PM₁ NO₃⁻ measurements may be due, in part, to the HR-ToF-AMS not being able to readily discriminate between the inorganic and organic nitrates, reasons for the HR-ToF-AMS PM₁ SO₄²⁻ and NH₄⁺ measurements being systematically higher than the PILS and filter measurements are not known. ¶ We

Deleted: factor

Deleted: 5

Deleted: (i.e., average of the PILS-HPIC/HR-ToF-AMS and PILS-IC/HR-ToF-AMS SO₄²⁻ slopes)

Deleted: scaled

Formatted: Font: (Asian) +Body (Calibri), Font color: Black

Deleted: study-averaged

Deleted: study-averaged

Deleted: NO₃⁻ mass concentration

gas-to-particle partitioning of organic and inorganic nitrates as temperature decreased (Xu et al., 2015a; Xu et al., 2015b). Quantification and characterization of organic nitrates based on HR-ToF-AMS and PILS-IC PM₁ NO₃⁻ measurements will be discussed in a future publication. NH₄⁺ mass concentration has moderate diurnal variations with marginally higher concentrations in the afternoon, likely due to the contrasting day/night phases of ammonium sulfate and ammonium nitrate formation. SO₄²⁻, NO₃⁻ and NH₄⁺ molar concentrations indicated that NH₄⁺ is mainly associated with SO₄²⁻ in PM₁.

3.3. PM₁ pH predictions

CIMS HNO₃ and NH₃ data, HR-ToF-AMS PM₁ SO₄²⁻ and NH₄⁺ data, PILS-IC PM₁ NO₃⁻ and non-volatile cation (Cl⁻, Na⁺, Ca²⁺, K⁺ and Mg²⁺) data, measured temperature and RH are used as ISORROPIA-II model inputs to predict PM₁ W_i and pH from 13 September to 6 October. Figure 3 shows the time series and average diurnal profiles of ISORROPIA-predicted PM₁ W_i and pH. PM₁ are highly acidic with pH values ranging from 0.9 to 3.8, and an average pH of 2.2 ± 0.6 . The average PM₁ pH was 2.5 ± 0.6 during periods where the NH₃ concentration was higher than 13.3 ppb (i.e., average NH₃ concentration + 1 standard deviation = $8.1 + 5.2 = 13.3$ ppb). The PM₁ pH values in this study are generally similar to those reported by Guo et al. (2015) at the same field site during winter 2012. Our observation that PM₁ are acidic despite the high NH₃ concentrations in this study is consistent with previous studies showing that particle pH has weak sensitivities to wide NH₃ and SO₄²⁻ mass concentration ranges due to pH buffering caused by the partitioning of NH₃ between the gas and particle phases (Weber et al., 2016; Guo et al., 2017c). This weak particle pH sensitivity also explains the small changes in PM₁ pH values (about 10 % lower, Fig. S8) when NH₃ measurements by the SEARCH network denuder-based instrument are used in ISORROPIA-II calculations (instead of NH₃-CIMS measurements).

PM₁ pH varied by approximately 1.4 units throughout the day. W_i has an average value of $1.6 \pm 1.7 \mu\text{g m}^{-3}$. PM₁ W_i and pH showed similar diurnal profiles, with both peaking in the mid-morning and reaching their minima in the mid-afternoon. These diurnal trends are consistent with those previously reported by Guo et al. (2015) for PM₁ measured during the summer and winter in different parts of the southeastern U.S. Also shown in Fig. 3b is the diurnal profile of H_{air}^+ , which peaked in the mid-afternoon. The W_i and H_{air}^+ maximum/minimum ratios are comparable (6.5 and

Deleted: scaled

Deleted: study-averaged

Deleted: study-

Deleted: d

Deleted: study-averaged

Deleted: 7

Deleted: a study-averaged

Deleted: ., and reaffirm that diurnal variation in particle pH is driven by W_i and not aerosol chemistry

5.3, respectively), thus indicating that the diurnal variation in particle pH is driven by both W_i and H_{air}^+ .

The average PM_1 pH for this study is about 1 unit higher than those for the SENEX and SOAS campaigns (Table 1), and is likely due to the much higher abundance of NH_3 in this study. The average NH_3 mass concentration in this study is approximately 49 times and 15 times higher than those in the SENEX and SOAS campaigns, respectively. The average PM_1 pH for this study is similar to that for the CalNex campaign even though the average NH_3 mass concentration in this study is only approximately 4 times higher than that in the CalNex campaign (Guo et al., 2017a). This ~~may be due, in part, to~~ PM_1 SO_4^{2-} and NO_3^- mass concentrations at CalNex being approximately 2 times and 18 times larger than those of this study, respectively. Aerosol inorganic SO_4^{2-} and NO_3^- species are hygroscopic species. The much higher NO_3^- mass concentrations in the CalNex campaign (due, in part, to high NO_x emissions) increased particle W_i substantially, which diluted H^+ and raised particle pH, resulting in more gas-to-particle partitioning of NO_3^- , and eventually leading to pH levels similar to those observed in this study. This type of feedback does not happen in the southeastern U.S. where non-volatile SO_4^{2-} dominates the uptake of particle water. It is also possible that the higher RH and lower temperatures during the CalNex campaign (relative to this study) contributed to high particle W_i , which diluted H^+ and raised particle pH levels similar to those observed in this study.

The validity of this study's thermodynamic model predictions is evaluated by comparing the predicted gas-particle partitioning ratios of semi-volatile inorganic compounds (i.e., NO_3^- and NH_4^+) with measured values (Fig. S9). CIMS HNO_3 and NH_3 data, PILS-IC NO_3^- and HR-ToF-AMS NH_4^+ data are used in this comparison. $\epsilon(NO_3^-)$ and $\epsilon(NH_4^+)$ are defined as the particle-phase molar concentration divided by the total molar concentration (gas + particle), i.e., $\epsilon(NO_3^-) = NO_3^- / (HNO_3 + NO_3^-)$ and $\epsilon(NH_4^+) = NH_4^+ / (NH_3 + NH_4^+)$. Predicted NH_3 , NH_4^+ and $\epsilon(NH_4^+)$ values are generally within 10 % of and are highly correlated ($R^2 = 0.96$ to 0.99) with measured values (Fig. S9). While predicted HNO_3 values generally agreed with measurements, substantial scatter can be seen between the predicted and measured values for NO_3^- and $\epsilon(NO_3^-)$. This scatter can be attributed, at least in part, to uncertainties brought about by the low PM_1 NO_3^- mass concentrations and effects of coarse mode cations (e.g., Na^+ , Ca^{2+} , K^+ and Mg^{2+}) on fine mode HNO_3 - NO_3^- gas-particle equilibrium (i.e., HNO_3 can partition to both fine and coarse modes, thereby affecting fine

Deleted: can be explained by

Deleted: highly

Deleted: 8

Deleted: scaled

Deleted: 8

mode NO_3^- concentrations; no such effect occurs for $\text{NH}_3\text{-NH}_4^+$ gas-particle equilibrium). In general, the overall good agreement between model predictions and measurements indicated that our assumptions that aerosols are metastable (i.e., aerosols are supersaturated aqueous droplets) with no phase separation for the thermodynamic calculations are reasonable for the conditions of this study, and do not affect model predictions.

The molar fractions of NO_3^- and NH_4^+ in the particle phase (i.e., $\epsilon(\text{NO}_3^-)$ and $\epsilon(\text{NH}_4^+)$) measured in this study are compared with those measured during the CalNex, SENEX and SOAS campaigns. Figure 4 shows the measured $\epsilon(\text{NO}_3^-)$ and $\epsilon(\text{NH}_4^+)$ values as a function of their ISORROPIA-predicted particle pH for the various field studies. For each field study, only a subset of the data is chosen for this comparison ($1 \leq W_i \leq 4 \mu\text{g m}^{-3}$ and $15 \text{ }^\circ\text{C} \leq \text{temperature} \leq 25 \text{ }^\circ\text{C}$) to reduce the effects of variability of W_i and temperature on gas-particle partitioning for comparison with the calculated S (or sigmoidal) curves, which are calculated based on $W_i = 2.5 \mu\text{g m}^{-3}$ and temperature = $20 \text{ }^\circ\text{C}$. The S curves for $\text{HNO}_3\text{-NO}_3^-$ and $\text{NH}_3\text{-NH}_4^+$ partitioning as a function of particle pH are also plotted as solid lines. The S curves are calculated based on the solubility and dissociation of NO_3^- and NH_4^+ species in water:

$$\epsilon(\text{NO}_3^-) = \frac{H_{\text{HNO}_3}^* RT W_i \times 0.987 \times 10^{-14}}{\gamma_{\text{H}^+} \gamma_{\text{NO}_3^-} 10^{-\text{pH}} + H_{\text{HNO}_3}^* RT W_i \times 0.987 \times 10^{-14}} \quad (2)$$

$$\epsilon(\text{NH}_4^+) = \frac{\frac{\gamma_{\text{H}^+} 10^{-\text{pH}}}{\gamma_{\text{NH}_4^+}} H_{\text{NH}_3}^* RT W_i \times 0.987 \times 10^{-14}}{1 + \frac{\gamma_{\text{H}^+} 10^{-\text{pH}}}{\gamma_{\text{NH}_4^+}} H_{\text{NH}_3}^* RT W_i \times 0.987 \times 10^{-14}} \quad (3)$$

where $H_{\text{HNO}_3}^*$ and $H_{\text{NH}_3}^*$ ($\text{mole}^2 \text{ kg}^{-2} \text{ atm}^{-1}$) are equilibrium constants and are the products of the Henry's law constant and the dissociation constant of HNO_3 and NH_3 , respectively, R is the gas constant ($8.314 \text{ m}^3 \text{ Pa K}^{-1} \text{ mol}^{-1}$), T is temperature (K), and γ_i 's are activity coefficients. $H_{\text{HNO}_3}^*$ and $H_{\text{NH}_3}^*$ values at $20 \text{ }^\circ\text{C}$ are calculated using equations found in Clegg and Brimblecombe (1990) and Clegg et al. (1998), respectively. Activity coefficients predicted by ISORROPIA-II are $\gamma_{\text{H}^+ - \text{NO}_3^-} = \sqrt{\gamma_{\text{H}^+} \gamma_{\text{NO}_3^-}} = 0.28$, $\gamma_{\text{H}^+} = 1$ and $\gamma_{\text{NH}_4^+} = 1$. Derivations of the analytically calculated S curves for $\epsilon(\text{NO}_3^-)$ and $\epsilon(\text{NH}_4^+)$ in equations 2 and 3 can be found in Guo et al. (2017a). As shown in Fig. 4, the measured $\epsilon(\text{NO}_3^-)$ and $\epsilon(\text{NH}_4^+)$ values for the four field studies all generally converged on the calculated S curves. The higher particle pH values in this study and the CalNex

549 campaign relative to those for the SENEX and SOAS campaigns resulted in less NH_3 and more
550 HNO_3 partitioned to the particle phase, as predicted by these simple analytical expressions. A
551 similar analysis will be performed for the organic acids in section 3.5.

552 3.4. WSOC and water-soluble organic acids

553 The time series and [average](#) diurnal profiles of WSOC_g and WSOC_p are shown in Fig. [S10](#).
554 The [average](#) WSOC_g mass concentration ($3.6 \pm 2.7 \mu\text{gC m}^{-3}$) is roughly four times higher than that
555 of WSOC_p ($1.0 \pm 0.6 \mu\text{gC m}^{-3}$). The diurnal profile of WSOC_p is somewhat flat, likely due to
556 various organic aerosol sources having different water solubility and diurnal cycles, and
557 compensating each other throughout the day (Xu et al., 2015b; Xu et al., 2017). In contrast, WSOC_g
558 displayed strong diurnal variations. WSOC_g increased at 07:30, which coincided with the sharp
559 increase in solar irradiance (Fig. S3). WSOC_g decreased at 21:30, approximately 2 hours after
560 sunset. Also shown in Fig. [S10](#) are the time series and [average](#) diurnal profile of the mass fraction
561 of total WSOC in the particle phase, i.e., $F_p = \text{WSOC}_p / (\text{WSOC}_p + \text{WSOC}_g)$. The peak F_p coincided
562 with the minima of WSOC_g at 07:30.

563 The [average](#) WSOC_g and WSOC_p ($3.6 \pm 2.7 \mu\text{gC m}^{-3}$ and $1.0 \pm 0.6 \mu\text{gC m}^{-3}$) are slightly
564 lower than those measured during the SOAS campaign (SOAS $\text{WSOC}_g = 4.9 \mu\text{gC m}^{-3}$ and WSOC_p
565 $= 1.7 \mu\text{gC m}^{-3}$) (Xu et al., 2017). While the diurnal profiles of WSOC_p in both studies are flat, the
566 diurnal profiles of WSOC_g measured in the two studies are different. WSOC_g measured in the
567 SOAS study decreased at sunset, while WSOC_g measured in this study decreased 2 hours after
568 sunset. Differences in WSOC_g diurnal profiles in the two studies are likely due to differences in
569 emission sources as a result of different sampling periods (SOAS was in early summer and this
570 study was in early fall), land use and/or land cover. The ratio of WSOC_p to OC for this study was
571 estimated at 30 %, but this comparison is imprecise because WSOC_p was PM_{10} and OC was $\text{PM}_{2.5}$
572 (refer to Fig. [S11](#) and SI section S2).

573 Figure 5 shows the time series of particle- and gas-phase concentrations of formic, acetic,
574 oxalic, malonic, succinic, glutaric and maleic acids. Their diurnal profiles are shown in Fig. 6.
575 Gas-phase measurements of glutaric and maleic acids are not available. Gas-phase measurements
576 of butyric, glycolic, propionic and valeric acids were also measured during the study and have

Deleted: study-averaged

Deleted: S9

Deleted: study-averaged

Deleted: S9

Deleted: study-averaged

Deleted: study-averaged

Deleted: S10

584 been presented in Nah et al. (2018), but will not be discussed here since their particle-phase
585 measurements are not available.

586 Assuming that all the measured organic acids are completely water-soluble, 30 % of the
587 WSOC_g is comprised of these organic acids (Nah et al., 2018). Formic and acetic acids are the
588 most abundant gas-phase organic acids, with averages of 2.2 ± 1.6 and $1.9 \pm 1.3 \mu\text{g m}^{-3}$,
589 respectively. The average carbon mass fraction of WSOC_g comprised of formic and acetic acids
590 are 7 and 13 %, respectively. All the gas-phase organic acids displayed strong and consistent
591 diurnal cycles, with higher concentrations being measured during warm and sunny days. Their
592 concentrations start to increase at sunrise (at 07:30), building to a peak between 15:30 and 19:30,
593 then decrease overnight.

594 Nah et al. (2018) previously showed that the measured gas-phase organic acids during the
595 study, including oxalic acid, likely have the same or similar sources. Poor correlations between
596 gas-phase organic acid concentrations and those of anthropogenic pollutants (HNO₃, SO₂, CO and
597 O₃) indicated that these organic acids are not due to anthropogenic emissions, and are likely
598 biogenic in nature. Biogenic emissions of gas-phase organic acids and/or their BVOC precursors
599 are elevated at high temperatures, resulting in higher organic acid concentrations during warm and
600 sunny days. For example, isoprene, which is the dominant BVOC in Yorkville, has a somewhat
601 similar diurnal profile as the organic acids. In addition, the concentration of isoprene is moderately
602 correlated with those of formic and acetic acids (Fig. S10 of Nah et al., 2018), which are known
603 products of isoprene photooxidation. Some of these gas-phase organic acids may also be formed
604 in the particle phase during organic aerosol photochemical aging, with subsequent volatilization
605 into the gas phase. The gas-particle partitioning of organic acids likely depends on thermodynamic
606 conditions, which are controlled by particle pH and W_i and meteorological conditions as will be
607 shown in section 3.5.

608 The measured particle-phase water-soluble organic acids contributed on average 6 % to the
609 HR-ToF-AMS-measured organic aerosol mass concentration. The average carbon mass fraction
610 of WSOC_p comprised of these organic acids is 4 %. Previous studies have shown that particle-
611 phase organic acids found in rural environments are oxidation products of gas-phase aliphatic
612 monocarboxylic acids, which are formed in the photochemical oxidation of biogenic unsaturated
613 fatty acids and other BVOC precursors (Kawamura and Gagosian, 1987; Kawamura and Ikushima,

Deleted: study average

Deleted: study-averaged

Deleted: scaled

Deleted: study-averaged

1993; Kerminen et al., 2000; Kawamura and Bikkina, 2016). These particle-phase organic acids can also be produced during the multiphase photochemical aging of ambient organic aerosols (Ervens et al., 2004; Lim et al., 2005; Sorooshian et al., 2007; Sorooshian et al., 2010).

Oxalate is the most abundant measured particle-phase water-soluble organic acid anion (contributing on average 26 % to the total particle-phase organic acid mass concentration), with mass concentrations ranging from 0.01 to 0.34 $\mu\text{g m}^{-3}$ and a average of $0.07 \pm 0.05 \mu\text{g m}^{-3}$. Acetate (average of $0.06 \pm 0.03 \mu\text{g m}^{-3}$) and formate (average of $0.05 \pm 0.03 \mu\text{g m}^{-3}$) are the second and third most abundant measured particle-phase water-soluble organic acid anions, respectively. Particle-phase formate, acetate and maleate showed weak diurnal variations, and may be due, in part, to various emission sources having different diurnal cycles and compensating each other throughout the day. Particle-phase oxalate, malonate and succinate peaked in the mid- to late afternoon, while glutarate generally peaked in the mid-morning. This suggests that while the production of these organic acids is photochemically-driven, they may have different BVOC precursors and/or different photochemical production pathways. In addition, since oxalic (C_2), malonic (C_3), succinic (C_4) and glutaric (C_5) acids belong to the same homologous series of organic diacids, it is possible that the photochemical aging of particle-phase glutaric acid resulted in the formation of its successive homologues via the cleavage of C-C bonds. Hence, organic aerosol photochemical aging may also have contributed to the diurnal profiles of particle-phase oxalate, malonate, succinate and glutarate.

3.5. Gas-particle partitioning of organic acids

The online and simultaneous measurements of gas- and particle-phase organic acid mass concentrations provided the opportunity to study gas-particle partitioning behavior of semi-volatile organic compounds with respect to particle pH, as is more commonly done with semi-volatile inorganic species (see section 3.3). Since formic, acetic and oxalic acids are the three most abundant measured organic acids present in the gas and particle phases, we focus on the gas-particle partitioning behaviors of these three organic acids. The average molar fractions (± 1 standard deviation) of formic, acetic and oxalic acid in the particle phase (i.e., $\epsilon(\text{HCOO}^-)$, $\epsilon(\text{CH}_3\text{CO}_2^-)$ and $\epsilon(\text{C}_2\text{O}_4^{2-})$) are $3.6 \pm 3.6 \%$, $5.8 \pm 5.0 \%$ and $73.7 \pm 9.8 \%$, respectively. The uncertainties of these ratios for formic, acetic and oxalic acids are 16, 16 and 17 %, respectively,

Deleted: a study-averaged

Deleted: study average

Deleted: study average

Deleted: study average

Deleted: likely

Deleted: study-averaged

which are obtained from the propagation of their SF₆-CIMS and PILS-HPIC measurement uncertainties.

3.5.1. Oxalic acid

To investigate the factors affecting oxalic acid gas-particle partitioning, the equation for the S curve describing the dependence of oxalic acid gas-particle partitioning (i.e., $\varepsilon(\text{C}_2\text{O}_4^{2-}) = \text{C}_2\text{O}_4^{2-} / (\text{C}_2\text{H}_2\text{O}_4 + \text{C}_2\text{O}_4^{2-})$) on particle pH is derived. As shown in SI section S3, the analytically calculated S curve for $\varepsilon(\text{C}_2\text{O}_4^{2-})$ can be simplified to:

$$\varepsilon(\text{C}_2\text{O}_4^{2-}) \cong \frac{H_{\text{C}_2\text{H}_2\text{O}_4} W_i RT \left(\frac{\gamma_H + \gamma_{\text{C}_2\text{HO}_4^-}}{\gamma_{\text{C}_2\text{H}_2\text{O}_4}} 10^{-\text{pH} + K_{a1}} \right) \times 0.987 \times 10^{-14}}{\gamma_H + \gamma_{\text{C}_2\text{HO}_4^-} 10^{-\text{pH}} + H_{\text{C}_2\text{H}_2\text{O}_4} W_i RT \left(\frac{\gamma_H + \gamma_{\text{C}_2\text{HO}_4^-}}{\gamma_{\text{C}_2\text{H}_2\text{O}_4}} 10^{-\text{pH} + K_{a1}} \right) \times 0.987 \times 10^{-14}} \quad (4)$$

where $H_{\text{C}_2\text{H}_2\text{O}_4}$ (mole L⁻¹ atm⁻¹) is the Henry's law constant for oxalic acid, K_{a1} (mole L⁻¹) is the first acid dissociation constant for oxalic acid, R is the gas constant (8.314 m³ Pa K⁻¹ mol⁻¹), T is temperature (K), and γ_i 's are activity coefficients. We used the web version of AIOMFAC (www.aiomfac.caltech.edu) (Zuend et al., 2008; Zuend et al., 2011; Zuend et al., 2012) to compute an average $\gamma_{\text{C}_2\text{H}_2\text{O}_4}$ value of 0.0492. Since AIOMFAC does not predict $\gamma_H + \gamma_{\text{C}_2\text{HO}_4^-}$, we assumed that $\gamma_H + \gamma_{\text{C}_2\text{HO}_4^-} = \gamma_H + \gamma_{\text{NO}_3^-}$, and used the ISORROPIA-predicted $\gamma_H + \gamma_{\text{NO}_3^-}$ value of 0.07. We used the average of $H_{\text{C}_2\text{H}_2\text{O}_4}$ values provided by Clegg et al. (1996), Compernelle and Muller (2014) and Saxena and Hildemann (1996) (6.11×10^8 mole L⁻¹ atm⁻¹ at 25 °C), and accounted for the effect of temperature using equation 19 in Sander (2015). Although K_{a1} also depends on temperature, we used the K_{a1} value at 25 °C (5.62×10^{-2} mole L⁻¹, (Haynes, 2014)) for all the oxalic acid S curve calculations since equations that compute K_{a1} values for pure aqueous oxalic acid solutions at different temperatures are not available in the literature. In addition, the temperatures observed in this study were close to 25 °C (study-average temperature = 23.4 ± 4.0 °C).

Different S curves for $\varepsilon(\text{C}_2\text{O}_4^{2-})$ are calculated using 1-hour average values obtained from the diurnal profiles of temperature and W_i (specifically at 00:30, 06:30 and 12:30). The shape of the S curve changes with the time of day due to the diurnal variations of temperature and W_i (Fig S12 and SI section S3). The S curves for $\varepsilon(\text{C}_2\text{O}_4^{2-})$ are very different from those of other acids,

Deleted: a study-averaged

Deleted: S11

681 such as $\epsilon(\text{NO}_3^-)$ (shown in Fig. 4b). From the S curves for $\epsilon(\text{C}_2\text{O}_4^{2-})$, which are calculated using
 682 conditions in this study, some molar fraction of oxalic acid is always expected to be present in the
 683 particle phase, even at low particle pH (i.e., the S curve does not go to zero at low pH). In contrast,
 684 HNO_3 is expected to be present primarily in the gas phase at low particle pH (i.e., $\text{pH} < 1$) under
 685 similar temperature and W_i conditions. This is due primarily to differences in the Henry's law
 686 constants for the two acids. H_{HNO_3} ($2.57 \times 10^5 \text{ mole L}^{-1} \text{ atm}^{-1}$) at 23.4°C is three orders of
 687 magnitude smaller than $H_{\text{C}_2\text{H}_2\text{O}_4}$ ($7.27 \times 10^8 \text{ mole L}^{-1} \text{ atm}^{-1}$) (Clegg and Brimblecombe, 1990;
 688 Sander, 2015). This means that some undissociated form of oxalate can be found in the particle
 689 phase at any pH, and the molar fraction of this form increases with particle W_i (see Fig. S12).
 690 Oxalic acid's very high Henry's law constant combined with the W_i conditions in this study
 691 ensures that some fraction of the organic acid will be in the particle phase regardless the particle
 692 pH.

693 Figure 7 compares the measured $\epsilon(\text{C}_2\text{O}_4^{2-})$ vs. ISORROPIA-predicted PM_1 pH to the
 694 analytically calculated S curves(s). The S curve is calculated based on the average temperature and
 695 W_i from 13 September to 6 October ($23.4 \pm 4.0^\circ\text{C}$ and $1.6 \pm 1.7 \mu\text{g m}^{-3}$, respectively). We also
 696 calculated the "upper" and "lower" bounds of this S curve based on one standard deviation from
 697 the average temperature and average W_i . Temperature = 27.4°C and $W_i = 0.5 \mu\text{g m}^{-3}$ are used for
 698 calculations of the "lower" bound, while temperature = 19.4°C and $W_i = 3.3 \mu\text{g m}^{-3}$ are used for
 699 calculations of the "upper" bound. For the ambient data, a range in W_i (0.5 to $4 \mu\text{g m}^{-3}$) and
 700 temperature (15 to 31°C) is chosen to be close to the analytical calculation. As shown in Fig. 7,
 701 the measured $\epsilon(\text{C}_2\text{O}_4^{2-})$ generally converged around the S curve calculated using the average
 702 temperature and W_i values. Although there is some scatter, the measured ratios are mostly within
 703 the "upper" and "lower" bounds of the S curve.

704 Since the measured $\epsilon(\text{C}_2\text{O}_4^{2-})$ are in general agreement with the analytically calculated S
 705 curve (Fig. 7), we can use the S curve to understand qualitatively how high NH_3 events at the site
 706 affect oxalic acid gas-particle partitioning. Here we define high NH_3 events as periods where the
 707 NH_3 concentration was higher than 13.3 ppb (which is the average NH_3 concentration + 1 standard
 708 deviation). As discussed in section 3.3, the PM_1 pH during high NH_3 events is 2.5 ± 0.6 , which is
 709 slightly higher than the average PM_1 pH of 2.2 ± 0.6 . Based on the S curve calculated using the

Deleted: S11

Deleted: W

Deleted: also

Deleted: the S curves for $\epsilon(\text{C}_2\text{O}_4^{2-})$ in Fig. 7

Deleted: study-averaged

Deleted: study-averaged

716 average temperature and W_i values, $\epsilon(\text{C}_2\text{O}_4^{2-})$ increases from 81 % to 89 % when particle pH
717 increases from 2.2 to 2.5. While this result indicates that high NH_3 concentrations can raise the
718 particle pH sufficiently such that it can promote gas-to-particle partitioning of oxalic acid, this is
719 not always the case. Specifically, increasing the particle pH from -2 (or lower) to 1 will not result
720 in a significant increase in $\epsilon(\text{C}_2\text{O}_4^{2-})$. Therefore, whether or not particle pH, and consequently
721 oxalic acid gas-particle partitioning, is sensitive to NH_3 concentration depends strongly on particle
722 pH values.

723 We also examined how well the analytically calculated S curve for $\epsilon(\text{C}_2\text{O}_4^{2-})$ captures
724 diurnal variations of the measured $\epsilon(\text{C}_2\text{O}_4^{2-})$. The ambient data is divided into two 12 hour sets
725 (08:00 to 19:59 and 20:00 to 07:59) based on the diurnal profile of solar irradiance. Two S curves
726 and their corresponding “upper” and “lower” bounds are calculated based on the average
727 temperature and W_i of the two data sets, and are subsequently compared to the ambient data. As
728 shown in Fig. S13, the measured $\epsilon(\text{C}_2\text{O}_4^{2-})$ in both data sets are generally consistent with predicted
729 values.

730 A number of inferences can be drawn from the overall good agreement between the
731 predicted and measured molar fractions of oxalic acid in the particle phase in Figs. 7 and S13. Our
732 assumptions regarding the activity coefficients, Henry’s law constant and acid dissociation
733 constants used in the S curve calculations of $\epsilon(\text{C}_2\text{O}_4^{2-})$ are reasonable for the conditions of this
734 study (or are at least self-consistent). Analytically calculated S curves are a simple way of
735 exploring how the gas-particle partitioning of semi-volatile inorganic and organic compounds in
736 the atmosphere are affected by the compound’s physicochemical properties (e.g., Henry’s law
737 constants and acid dissociation constants), temperature, W_i and pH. Overall, these results indicate
738 that particle-phase oxalate is in equilibrium with gas-phase oxalic acid, and that particle pH can
739 influence particle-phase oxalate concentrations. It also showed that particle-phase oxalate can be
740 found over a broad pH range, and that the presence of oxalate does not necessarily provide insights
741 of the particle pH. Because of its high Henry’s law constant, particle-phase oxalate can be found
742 in aerosols even at extremely low pH values (i.e., the flat region in Fig. 7), although our data cannot
743 be used to test this since ambient particle pH values in this study are too high.

744 3.5.2 Formic and acetic acids

Deleted: S12

Deleted: S11

Deleted: S curves can be used to estimate activity coefficients based on gas-particle partitioning data in cases where they are not available in the literature if the other parameters are known.

Similar comparisons between the predicted and measured $\varepsilon(\text{HCOO}^-)$ and $\varepsilon(\text{CH}_3\text{CO}_2^-)$ can also be made. Derivation of the equations for S curves describing the dependence of formic and acetic acid gas-particle partitioning (i.e., $\varepsilon(\text{HCOO}^-) = \text{HCOO}^- / (\text{HCOOH} + \text{HCOO}^-)$ and $\varepsilon(\text{CH}_3\text{CO}_2^-) = \text{CH}_3\text{CO}_2^- / (\text{CH}_3\text{CO}_2\text{H} + \text{CH}_3\text{CO}_2^-)$, respectively) on particle pH are similar to that of HNO_3 since they are monoprotic acids:

$$\varepsilon(\text{HCOO}^-) = \frac{H_{\text{HCOOH}} W_i RT \left(\frac{\gamma_H + \gamma_{\text{HCOO}^-}}{\gamma_{\text{HCOOH}}} 10^{-\text{pH} + K_{a1}} \right) \times 0.987 \times 10^{-14}}{\gamma_H + \gamma_{\text{HCOO}^-} 10^{-\text{pH}} + H_{\text{HCOOH}} W_i RT \left(\frac{\gamma_H + \gamma_{\text{HCOO}^-}}{\gamma_{\text{HCOOH}}} 10^{-\text{pH} + K_{a1}} \right) \times 0.987 \times 10^{-14}} \quad (5)$$

$$\varepsilon(\text{CH}_3\text{CO}_2^-) = \frac{H_{\text{CH}_3\text{CO}_2\text{H}} W_i RT \left(\frac{\gamma_H + \gamma_{\text{CH}_3\text{CO}_2^-}}{\gamma_{\text{CH}_3\text{CO}_2\text{H}}} 10^{-\text{pH} + K_{a1}} \right) \times 0.987 \times 10^{-14}}{\gamma_H + \gamma_{\text{CH}_3\text{CO}_2^-} 10^{-\text{pH}} + H_{\text{CH}_3\text{CO}_2\text{H}} W_i RT \left(\frac{\gamma_H + \gamma_{\text{CH}_3\text{CO}_2^-}}{\gamma_{\text{CH}_3\text{CO}_2\text{H}}} 10^{-\text{pH} + K_{a1}} \right) \times 0.987 \times 10^{-14}} \quad (6)$$

where H_{HCOOH} and $H_{\text{CH}_3\text{CO}_2\text{H}}$ (mole $\text{L}^{-1} \text{atm}^{-1}$) are the Henry's law constants for formic and acetic acid, K_{a1} 's (mole L^{-1}) are the first acid dissociation constants, R is the gas constant ($8.314 \text{ m}^3 \text{ Pa K}^{-1} \text{ mol}^{-1}$), T is temperature (K), and γ_i 's are activity coefficients. We used the web version of AIOMFAC (www.aiomfac.caltech.edu) (Zuend et al., 2008; Zuend et al., 2011; Zuend et al., 2012) to compute average γ_{HCOOH} and $\gamma_{\text{CH}_3\text{CO}_2\text{H}}$ values of 0.334 and 2.150, respectively. Similar to the case of oxalic acid, we assumed that $\gamma_H + \gamma_{\text{HCOO}^-} = \gamma_H + \gamma_{\text{CH}_3\text{CO}_2^-} = \gamma_H + \gamma_{\text{NO}_3^-}$, and used the ISORROPIA-predicted $\gamma_H + \gamma_{\text{NO}_3^-}$ value of 0.07. Temperature-dependent H_{HCOOH} and $H_{\text{CH}_3\text{CO}_2\text{H}}$ values are obtained from Sander (2015) using the same methodology employed to determine temperature-dependent $H_{\text{C}_2\text{H}_2\text{O}_4}$ values. We used K_{a1} values at 25°C (1.78×10^{-4} mole L^{-1} for formic acid, and 1.75×10^{-5} mole L^{-1} for acetic acid (Haynes, 2014)) for the S curve calculations.

S curves for $\varepsilon(\text{HCOO}^-)$ and $\varepsilon(\text{CH}_3\text{CO}_2^-)$ calculated based on temperature = 23.4°C and $W_i = 1.6 \mu\text{g m}^{-3}$ can be seen in Fig. 8. Practically no formic or acetic acids are predicted to partition to the particle phase (relative to oxalic acid) for the range of PM_1 pH calculated in this study. This is due to significant differences in the Henry's law constants and acid dissociation constants for the three organic acids. H_{HCOOH} and $H_{\text{CH}_3\text{CO}_2\text{H}}$ (9540 and 5370 mole $\text{L}^{-1} \text{atm}^{-1}$, respectively) at 23.4°C are substantially smaller than $H_{\text{C}_2\text{H}_2\text{O}_4}$ (7.27×10^8 mole $\text{L}^{-1} \text{atm}^{-1}$) (Sander, 2015). The K_{a1} values for formic and acetic acids (1.78×10^{-4} and 1.75×10^{-5} mole L^{-1} , respectively) are also considerably smaller than the K_{a1} value for oxalic acid (5.62×10^{-2} mole L^{-1}) (Haynes, 2014). Note

Deleted: study-averaged

777 that H_{HNO_3} is between that of $H_{C_2H_2O_4}$ and those of H_{HCOOH} and $H_{CH_3CO_2H}$ (compare Fig. 4b with
778 Figs. 7 and 8).

779 As shown in Fig. 8, higher than expected levels of formate and acetate are observed in the
780 particle phase. This has also been reported in previous studies (Liu et al., 2012). Laboratory tests
781 showed that the disagreement cannot be explained by positive biases in the particle-phase formate
782 and acetate PILS-HPIC measurements resulting from less than 100 % gas removal by the carbon
783 denuder. The measured denuder efficiency for formic acid was $\geq 99.97\%$ (SI section S4). The
784 possibility that formic and acetic acid dimers in the aqueous phase (Schrier et al., 1964; Gilson et
785 al., 1997; Chen et al., 2008) may result in higher than predicted molar fractions of formate and
786 acetate in the particle phase was explored, but also could not explain the observed gas-particle
787 partitioning of these acids (SI section S5). The disagreement could be due to incorrect Henry's law
788 constants for formic and acetic acids. However, the Henry's law constants for formic and acetic
789 acid would have to be $\sim 10^4$ times and $\sim 3 \times 10^5$ times larger than their literature values, respectively,
790 in order for their S curves to match our measured molar fractions of formic and acetic acid in the
791 particle phase. In addition, formic and acetic acids may not be internally mixed with most of the
792 other PM₁ aerosol components (e.g., SO₄²⁻, NO₃⁻, NH₄⁺, CH₃CO₂H), and thus are not associated
793 with acidic aerosols, as assumed above. They may instead be associated with aerosols largely
794 composed of non-volatile cations and have a pH closer to neutral. More research is needed to
795 explain this disagreement.

796 4. Summary

797 Gas- and particle-phase measurements were conducted in Yorkville, Georgia (a rural field
798 site) during fall 2016. The goal of the field study was to understand how NH₃ affects particle
799 acidity, and consequently SOA formation through the gas-particle partitioning of semi-volatile
800 inorganic and organic compounds. Since it is a rural site surrounded by forest, agricultural land
801 and CAFOs, this study provided an opportunity for ambient observations in an area impacted by
802 high local emissions of BVOCs and NH₃.

803 NH₃ concentrations measured by the NH₃-CIMS ranged from 0.7 to 39.0 ppb (average 8.1
804 ± 5.2 ppb), which were substantially higher than typical levels in the southeastern U.S.. PM₁
805 inorganic chemical composition, gas-phase HNO₃ and NH₃ concentrations, temperature and RH

Deleted: study average

807 were used as model inputs in the ISORROPIA-II thermodynamic model to calculate PM₁ pH and
808 W_i . PM₁ pH ranged from 0.9 to 3.8, with an average pH of 2.2 ± 0.6 . The measured and predicted
809 HNO₃-NO₃⁻ and NH₃-NH₄⁺ gas-particle partitioning ratios were in good agreement. The measured
810 gas-phase organic acids were estimated to contribute 30 % of the overall WSOC_g on a carbon mass
811 basis, whereas measured particle-phase organic acids comprised 6 % of the total organic aerosol
812 mass concentration and 4 % of the overall WSOC_p on a carbon mass basis. Formic and acetic acids
813 were the most abundant gas-phase organic acids, with averages of 2.2 ± 1.6 and 1.9 ± 1.3 µg m⁻³,
814 respectively. Oxalate was the most abundant particle-phase water-soluble organic acid anion, with
815 a average of 0.07 ± 0.05 µg m⁻³. Measured oxalic acid gas-particle partitioning ratios generally
816 agreed with analytical predictions, which were based on oxalic acid's physicochemical properties
817 (specifically, its Henry's law constants, acid dissociation constants and activity coefficients),
818 temperature, W_i and particle pH. The partitioning of oxalic acid to the particle phase is highly
819 sensitive to temperature and W_i . In contrast, the partitioning of formic and acetic acids to the
820 particle phase were higher than predicted for reasons currently unknown.

Deleted: a study-averaged

Deleted: study average

Deleted: study average

821 Although past air regulations have resulted in decreased sulfate, nitrate and ammonium
822 aerosol mass concentrations across the U.S., our study suggests that the current limited regulation
823 of NH₃ emissions may result in some increase in the organic aerosol mass concentration due to
824 increased gas-to-particle partitioning of some organic acids. However, in this study, the effect was
825 small since the organic acids comprised a small fraction of the overall organic aerosol mass.

826 5. Acknowledgements

827 The authors thank Eric Edgerton (Atmospheric Research and Analysis, Inc.) for providing
828 SEARCH network measurements and meteorological data.

829 6. Funding

830 This publication was developed under U.S. Environmental Protection Agency (EPA)
831 STAR Grant R835882 awarded to Georgia Institute of Technology. It has not been formally
832 reviewed by the EPA. The views expressed in this document are solely those of the authors and
833 do not necessarily reflect those of the EPA. EPA does not endorse any products or commercial
834 services mentioned in this publication.

7. Competing financial interests

The authors declare no competing financial interests.

8. Data availability

Data can be accessed by request (rweber@eas.gatech.edu).

9. References

Barbier-Jr, J., and Duprez, D.: Steam Effects in 3-way catalysis, *Applied Catalysis B-Environmental*, 4, 105-140, 10.1016/0926-3373(94)80046-4, 1994.

Bertram, A. K., Martin, S. T., Hanna, S. J., Smith, M. L., Bodsworth, A., Chen, Q., Kuwata, M., Liu, A., You, Y., and Zorn, S. R.: Predicting the relative humidities of liquid-liquid phase separation, efflorescence, and deliquescence of mixed particles of ammonium sulfate, organic material, and water using the organic-to-sulfate mass ratio of the particle and the oxygen-to-carbon elemental ratio of the organic component, *Atmos. Chem. Phys.*, 11, 10995-11006, 10.5194/acp-11-10995-2011, 2011.

Blanchard, C. L., Hidy, G. M., Tanenbaum, S., and Edgerton, E. S.: NMOC, ozone, and organic aerosol in the southeastern United States, 1999-2007: 3. Origins of organic aerosol in Atlanta, Georgia, and surrounding areas, *Atmospheric Environment*, 45, 1291-1302, 10.1016/j.atmosenv.2010.12.004, 2011.

Blanchard, C. L., Hidy, G. M., Tanenbaum, S., Edgerton, E. S., and Hartsell, B. E.: The Southeastern Aerosol Research and Characterization (SEARCH) study: Spatial variations and chemical climatology, 1999-2010, *Journal of the Air & Waste Management Association*, 63, 260-275, 10.1080/10962247.2012.749816, 2013a.

Blanchard, C. L., Hidy, G. M., Tanenbaum, S., Edgerton, E. S., and Hartsell, B. E.: The Southeastern Aerosol Research and Characterization (SEARCH) study: Temporal trends in gas and PM concentrations and composition, 1999-2010, *Journal of the Air & Waste Management Association*, 63, 247-259, 10.1080/10962247.2012.748523, 2013b.

Deleted: 7

864 Blanchard, C. L., Tanenbaum, S., and Hidy, G. M.: Source Attribution of Air Pollutant
 865 Concentrations and Trends in the Southeastern Aerosol Research and Characterization (SEARCH)
 866 Network, *Environmental Science & Technology*, 47, 13536-13545, 10.1021/es402876s, 2013c.

867 Bougiatioti, A., Nikolaou, P., Stavroulas, I., Kouvarakis, G., Weber, R., Nenes, A., Kanakidou,
 868 M., and Mihalopoulos, N.: Particle water and pH in the eastern Mediterranean: source variability
 869 and implications for nutrient availability, *Atmos. Chem. Phys.*, 16, 4579-4591, 10.5194/acp-16-
 870 4579-2016, 2016.

871 Boyd, C. M., Sanchez, J., Xu, L., Eugene, A. J., Nah, T., Tuet, W. Y., Guzman, M. I., and Ng, N.
 872 L.: Secondary organic aerosol formation from the beta-pinene+NO₃ system: effect of humidity
 873 and peroxy radical fate, *Atmos. Chem. Phys.*, 15, 7497-7522, 10.5194/acp-15-7497-2015, 2015.

874 Boyd, C. M., Nah, T., Xu, L., Berkemeier, T., and Ng, N. L.: Secondary Organic Aerosol (SOA)
 875 from Nitrate Radical Oxidation of Monoterpenes: Effects of Temperature, Dilution, and Humidity
 876 on Aerosol Formation, Mixing, and Evaporation, *Environmental Science & Technology*, 51, 7831-
 877 7841, 10.1021/acs.est.7b01460, 2017.

878 Canagaratna, M. R., Jayne, J. T., Jimenez, J. L., Allan, J. D., Alfarra, M. R., Zhang, Q., Onasch,
 879 T. B., Drewnick, F., Coe, H., Middlebrook, A., Delia, A., Williams, L. R., Trimborn, A. M.,
 880 Northway, M. J., DeCarlo, P. F., Kolb, C. E., Davidovits, P., and Worsnop, D. R.: Chemical and
 881 microphysical characterization of ambient aerosols with the aerodyne aerosol mass spectrometer,
 882 *Mass Spectrometry Reviews*, 26, 185-222, 10.1002/mas.20115, 2007.

883 Canagaratna, M. R., Jimenez, J. L., Kroll, J. H., Chen, Q., Kessler, S. H., Massoli, P., Hildebrandt
 884 Ruiz, L., Fortner, E., Williams, L. R., Wilson, K. R., Surratt, J. D., Donahue, N. M., Jayne, J. T.,
 885 and Worsnop, D. R.: Elemental ratio measurements of organic compounds using aerosol mass
 886 spectrometry: characterization, improved calibration, and implications, *Atmos. Chem. Phys.*, 15,
 887 253-272, 10.5194/acp-15-253-2015, 2015.

888 Case, J. L., and Zavodsky, B. T.: Evolution of 2016 drought in the Southeastern United States from
 889 a Land surface modeling perspective, *Results in Physics*, 8, 654-656, 10.1016/j.rinp.2017.12.029,
 890 2018.

891 Chen, J. H., Brooks, C. L., and Scheraga, H. A.: Revisiting the carboxylic acid dimers in aqueous
 892 solution: Interplay of hydrogen bonding, hydrophobic interactions, and entropy, *Journal of*
 893 *Physical Chemistry B*, 112, 242-249, 10.1021/jp074355h, 2008.

894 Clegg, S. L., and Brimblecombe, P.: Equilibrium partial pressures and mean activity and osmotic
 895 coefficients of 0-100-percent nitric- acid as a function of temperature, *Journal of Physical*
 896 *Chemistry*, 94, 5369-5380, 10.1021/j100376a038, 1990.

897 Clegg, S. L., Brimblecombe, P., and Khan, L.: The Henry's law constant of oxalic acid and its
 898 partitioning into the atmospheric aerosol, *Idojaras*, 100, 51-68, 1996.

899 Clegg, S. L., Brimblecombe, P., and Wexler, A. S.: Thermodynamic model of the system H^+ -
 900 NH_4^+ - SO_4^{2-} - NO_3^- - H_2O at tropospheric temperatures, *Journal of Physical Chemistry A*, 102,
 901 2137-2154, 10.1021/jp973042r, 1998.

902 DeCarlo, P. F., Kimmel, J. R., Trimborn, A., Northway, M. J., Jayne, J. T., Aiken, A. C., Gonin,
 903 M., Fuhrer, K., Horvath, T., Docherty, K. S., Worsnop, D. R., and Jimenez, J. L.: Field-deployable,
 904 high-resolution, time-of-flight aerosol mass spectrometer, *Analytical Chemistry*, 78, 8281-8289,
 905 10.1021/ac061249n, 2006.

906 Dentener, F. J., and Crutzen, P. J.: A 3-DIMENSIONAL MODEL OF THE GLOBAL AMMONIA
 907 CYCLE, *Journal of Atmospheric Chemistry*, 19, 331-369, 10.1007/bf00694492, 1994.

908 Eatough, D. J., Wadsworth, A., Eatough, D. A., Crawford, J. W., Hansen, L. D., and Lewis, E. A.:
 909 A multiple-system, multi-channel diffusion denuder sampler for the determination of fine-
 910 particulate organic material in the atmosphere, *Atmospheric Environment. Part A. General Topics*,
 911 27, 1213-1219, 10.1016/0960-1686(93)90247-V, 1993.

912 Edgerton, E. S., Hartsell, B. E., Saylor, R. D., Jansen, J. J., Hansen, D. A., and Hidy, G. M.: The
 913 southeastern aerosol research and characterization study: Part II. Filter-based measurements of
 914 fine and coarse particulate matter mass and composition, *Journal of the Air & Waste Management*
 915 *Association*, 55, 1527-1542, 2005.

916 Edgerton, E. S., Hartsell, B. E., Saylor, R. D., Jansen, J. J., Hansen, D. A., and Hidy, G. M.: The
 917 Southeastern Aerosol Research and Characterization Study, part 3: Continuous measurements of

918 fine particulate matter mass and composition, *Journal of the Air & Waste Management*
919 Association, 56, 1325-1341, 10.1080/10473289.2006.10464585, 2006.

920 Edgerton, E. S., Saylor, R. D., Hartsell, B. E., Jansen, J. J., and Hansen, D. A.: Ammonia and
921 ammonium measurements from the southeastern United States, *Atmospheric Environment*, 41,
922 3339-3351, 10.1016/j.atmosenv.2006.12.034, 2007.

923 Ellis, R. A., Murphy, J. G., Markovic, M. Z., VandenBoer, T. C., Makar, P. A., Brook, J., and
924 Mihele, C.: The influence of gas-particle partitioning and surface-atmosphere exchange on
925 ammonia during BAQS-Met, *Atmos. Chem. Phys.*, 11, 133-145, 10.5194/acp-11-133-2011, 2011.

926 Ellis, R. A., Jacob, D. J., Sulprizio, M. P., Zhang, L., Holmes, C. D., Schichtel, B. A., Blett, T.,
927 Porter, E., Pardo, L. H., and Lynch, J. A.: Present and future nitrogen deposition to national parks
928 in the United States: critical load exceedances, *Atmos. Chem. Phys.*, 13, 9083-9095, 10.5194/acp-
929 13-9083-2013, 2013.

930 Ervens, B., Feingold, G., Frost, G. J., and Kreidenweis, S. M.: A modeling study of aqueous
931 production of dicarboxylic acids: 1. Chemical pathways and speciated organic mass production,
932 *Journal of Geophysical Research-Atmospheres*, 109, 10.1029/2003jd004387, 2004.

933 Fountoukis, C., and Nenes, A.: ISORROPIA II: a computationally efficient thermodynamic
934 equilibrium model for $K^+-Ca^{2+}-Mg^{2+}-NH_4^+-Na^+-SO_4^{2-}-NO_3^- -Cl^- -H_2O$ aerosols, *Atmos.*
935 *Chem. Phys.*, 7, 4639-4659, 2007.

936 Gilson, M. K., Given, J. A., Bush, B. L., and McCammon, J. A.: The statistical-thermodynamic
937 basis for computation of binding affinities: A critical review, *Biophysical Journal*, 72, 1047-1069,
938 10.1016/s0006-3495(97)78756-3, 1997.

939 Guenther, A. B., Jiang, X., Heald, C. L., Sakulyanontvittaya, T., Duhl, T., Emmons, L. K., and
940 Wang, X.: The Model of Emissions of Gases and Aerosols from Nature version 2.1 (MEGAN2.1):
941 an extended and updated framework for modeling biogenic emissions, *Geoscientific Model*
942 *Development*, 5, 1471-1492, 10.5194/gmd-5-1471-2012, 2012.

943 Guo, H., Xu, L., Bougiatioti, A., Cerully, K. M., Capps, S. L., Hite, J. R., Jr., Carlton, A. G., Lee,
944 S. H., Bergin, M. H., Ng, N. L., Nenes, A., and Weber, R. J.: Fine-particle water and pH in the

945 southeastern United States, *Atmos. Chem. Phys.*, 15, 5211-5228, 10.5194/acp-15-5211-2015,
946 2015.

947 Guo, H., Sullivan, A. P., Campuzano-Jost, P., Schroder, J. C., Lopez-Hilfiker, F. D., Dibb, J. E.,
948 Jimenez, J. L., Thornton, J. A., Brown, S. S., Nenes, A., and Weber, R. J.: Fine particle pH and
949 the partitioning of nitric acid during winter in the northeastern United States, *Journal of*
950 *Geophysical Research-Atmospheres*, 121, 10355-10376, 10.1002/2016jd025311, 2016.

951 Guo, H., Liu, J. M., Froyd, K. D., Roberts, J. M., Veres, P. R., Hayes, P. L., Jimenez, J. L., Nenes,
952 A., and Weber, R. J.: Fine particle pH and gas-particle phase partitioning of inorganic species in
953 Pasadena, California, during the 2010 CalNex campaign, *Atmos. Chem. Phys.*, 17, 5703-5719,
954 10.5194/acp-17-5703-2017, 2017a.

955 Guo, H., Nenes, A., and Weber, R. J.: The underappreciated role of nonvolatile cations on aerosol
956 ammonium-sulfate molar ratios, *Atmos. Chem. Phys. Discuss.*, 2017, 1-19, 10.5194/acp-2017-
957 737, 2017b.

958 Guo, H., Weber, R. J., and Nenes, A.: High levels of ammonia do not raise fine particle pH
959 sufficiently to yield nitrogen oxide-dominated sulfate production, *Scientific Reports*, 7,
960 10.1038/s41598-017-11704-0, 2017c.

961 Hansen, D. A., Edgerton, E. S., Hartsell, B. E., Jansen, J. J., Kandasamy, N., Hidy, G. M., and
962 Blanchard, C. L.: The southeastern aerosol research and characterization study: Part 1-overview,
963 *Journal of the Air & Waste Management Association*, 53, 1460-1471, 2003.

964 Haynes, W. M.: *CRC handbook of chemistry and physics: A ready-reference book of chemical*
965 *and physical data.* , Boca Raton: CRC Press, 2014.

966 Hennigan, C. J., Izumi, J., Sullivan, A. P., Weber, R. J., and Nenes, A.: A critical evaluation of
967 proxy methods used to estimate the acidity of atmospheric particles, *Atmos. Chem. Phys.*, 15,
968 2775-2790, 10.5194/acp-15-2775-2015, 2015.

969 Huey, L. G., Hanson, D. R., and Howard, C. J.: Reactions of SF₆- and I- with Atmospheric Trace
970 Gases, *Journal of Physical Chemistry*, 99, 5001-5008, 10.1021/j100014a021, 1995.

971 Huey, L. G., Tanner, D. J., Slusher, D. L., Dibb, J. E., Arimoto, R., Chen, G., Davis, D., Buhr, M.
 972 P., Nowak, J. B., Mauldin, R. L., Eisele, F. L., and Kosciuch, E.: CIMS measurements of HNO₃
 973 and SO₂ at the South Pole during ISCAT 2000, *Atmospheric Environment*, 38, 5411-5421,
 974 10.1016/j.atmosenv.2004.04.037, 2004.

975 Kawamura, K., and Gagosian, R. B.: Implication of omega-oxocarboxylic acids in the remote
 976 marine atmosphere for photo-oxidation of unsaturated fatty acids, *Nature*, 325, 330-332,
 977 10.1038/325330a0, 1987.

978 Kawamura, K., and Ikushima, K.: Seasonal changes in the distribution of dicarboxylic acids in the
 979 urban atmosphere, *Environmental Science & Technology*, 27, 2227-2235, 10.1021/es00047a033,
 980 1993.

981 Kawamura, K., and Bikkina, S.: A review of dicarboxylic acids and related compounds in
 982 atmospheric aerosols: Molecular distributions, sources and transformation, *Atmospheric Research*,
 983 170, 140-160, 10.1016/j.atmosres.2015.11.018, 2016.

984 Kerminen, V. M., Ojanen, C., Pakkanen, T., Hillamo, R., Aurela, M., and Merilainen, J.: Low-
 985 molecular-weight dicarboxylic acids in an urban and rural atmosphere, *Journal of Aerosol Science*,
 986 31, 349-362, 10.1016/s0021-8502(99)00063-4, 2000.

987 Lamarque, J. F., Bond, T. C., Eyring, V., Granier, C., Heil, A., Klimont, Z., Lee, D., Lioussé, C.,
 988 Mieville, A., Owen, B., Schultz, M. G., Shindell, D., Smith, S. J., Stehfest, E., Van Aardenne, J.,
 989 Cooper, O. R., Kainuma, M., Mahowald, N., McConnell, J. R., Naik, V., Riahi, K., and van
 990 Vuuren, D. P.: Historical (1850-2000) gridded anthropogenic and biomass burning emissions of
 991 reactive gases and aerosols: methodology and application, *Atmos. Chem. Phys.*, 10, 7017-7039,
 992 10.5194/acp-10-7017-2010, 2010.

993 Laskin, A., Laskin, J., and Nizkorodov, S. A.: Chemistry of Atmospheric Brown Carbon, *Chemical*
 994 *Reviews*, 115, 4335-4382, 10.1021/cr5006167, 2015.

995 Laskin, J., Laskin, A., Roach, P. J., Slys, G. W., Anderson, G. A., Nizkorodov, S. A., Bones, D.
 996 L., and Nguyen, L. Q.: High-Resolution Desorption Electrospray Ionization Mass Spectrometry

997 for Chemical Characterization of Organic Aerosols, *Analytical Chemistry*, 82, 2048-2058,
 998 10.1021/ac902801f, 2010.

999 Lee, B. H., Mohr, C., Lopez-Hilfiker, F. D., Lutz, A., Hallquist, M., Lee, L., Romer, P., Cohen, R.
 1000 C., Iyer, S., Kurten, T., Hu, W. W., Day, D. A., Campuzano-Jost, P., Jimenez, J. L., Xu, L., Ng,
 1001 N. L., Guo, H. Y., Weber, R. J., Wild, R. J., Brown, S. S., Koss, A., de Gouw, J., Olson, K.,
 1002 Goldstein, A. H., Seco, R., Kim, S., McAvey, K., Shepson, P. B., Starn, T., Baumann, K.,
 1003 Edgerton, E. S., Liu, J. M., Shilling, J. E., Miller, D. O., Brune, W., Schobesberger, S., D'Ambro,
 1004 E. L., and Thornton, J. A.: Highly functionalized organic nitrates in the southeast United States:
 1005 Contribution to secondary organic aerosol and reactive nitrogen budgets, *Proceedings of the*
 1006 *National Academy of Sciences of the United States of America*, 113, 1516-1521,
 1007 10.1073/pnas.1508108113, 2016.

1008 Lee, B. P., Li, Y. J., Yu, J. Z., Louie, P. K. K., and Chan, C. K.: Characteristics of submicron
 1009 particulate matter at the urban roadside in downtown Hong Kong-Overview of 4 months of
 1010 continuous high-resolution aerosol mass spectrometer measurements, *Journal of Geophysical*
 1011 *Research-Atmospheres*, 120, 7040-7058, 10.1002/2015jd023311, 2015.

1012 Lee, H. J., Laskin, A., Laskin, J., and Nizkorodov, S. A.: Excitation-Emission Spectra and
 1013 Fluorescence Quantum Yields for Fresh and Aged Biogenic Secondary Organic Aerosols,
 1014 *Environmental Science & Technology*, 47, 5763-5770, 10.1021/es400644c, 2013.

1015 Lim, H. J., Carlton, A. G., and Turpin, B. J.: Isoprene forms secondary organic aerosol through
 1016 cloud processing: Model simulations, *Environmental Science & Technology*, 39, 4441-4446,
 1017 10.1021/es048039h, 2005.

1018 Liu, J., Zhang, X., Parker, E. T., Veres, P. R., Roberts, J. M., de Gouw, J. A., Hayes, P. L., Jimenez,
 1019 J. L., Murphy, J. G., Ellis, R. A., Huey, L. G., and Weber, R. J.: On the gas-particle partitioning of
 1020 soluble organic aerosol in two urban atmospheres with contrasting emissions: 2. Gas and particle
 1021 phase formic acid, *Journal of Geophysical Research-Atmospheres*, 117, 10.1029/2012jd017912,
 1022 2012.

1023 Livingston, C., Rieger, P., and Winer, A.: Ammonia emissions from a representative in-use fleet
 1024 of light and medium-duty vehicles in the California South Coast Air Basin, *Atmospheric*
 1025 *Environment*, 43, 3326-3333, 10.1016/j.atmosenv.2009.04.009, 2009.

1026 Malm, W. C., and Day, D. E.: Estimates of aerosol species scattering characteristics as a function
 1027 of relative humidity, *Atmospheric Environment*, 35, 2845-2860, 10.1016/s1352-2310(01)00077-
 1028 2, 2001.

1029 Middlebrook, A. M., Bahreini, R., Jimenez, J. L., and Canagaratna, M. R.: Evaluation of
 1030 Composition-Dependent Collection Efficiencies for the Aerodyne Aerosol Mass Spectrometer
 1031 using Field Data, *Aerosol Science and Technology*, 46, 258-271, 10.1080/02786826.2011.620041,
 1032 2012.

1033 Na, K., Song, C., Switzer, C., and Cocker, D. R.: Effect of ammonia on secondary organic aerosol
 1034 formation from alpha-Pinene ozonolysis in dry and humid conditions, *Environmental Science &*
 1035 *Technology*, 41, 6096-6102, 10.1021/es061956y, 2007.

1036 Nah, T., Ji, Y., Tanner, D. J., Guo, H., Sullivan, A. P., Ng, N. L., Weber, R. J., and Huey, L. G.:
 1037 Real-time measurements of gas-phase organic acids using SF₆- chemical ionization mass
 1038 spectrometry, *Atmos. Meas. Tech. Discuss.*, 2018, 1-40, 10.5194/amt-2018-46, 2018.

1039 Nenes, A., Pandis, S. N., and Pilinis, C.: ISORROPIA: A new thermodynamic equilibrium model
 1040 for multiphase multicomponent inorganic aerosols, *Aquatic Geochemistry*, 4, 123-152,
 1041 10.1023/a:1009604003981, 1998.

1042 Neuman, J. A., Ryerson, T. B., Huey, L. G., Jakoubek, R., Nowak, J. B., Simons, C., and
 1043 Fehsenfeld, F. C.: Calibration and evaluation of nitric acid and ammonia permeation tubes by UV
 1044 optical absorption, *Environmental Science & Technology*, 37, 2975-2981, 10.1021/es0264221,
 1045 2003.

1046 Ng, N. L., Brown, S. S., Archibald, A. T., Atlas, E., Cohen, R. C., Crowley, J. N., Day, D. A.,
 1047 Donahue, N. M., Fry, J. L., Fuchs, H., Griffin, R. J., Guzman, M. I., Herrmann, H., Hodzic, A.,
 1048 Iinuma, Y., Jimenez, J. L., Kiendler-Scharr, A., Lee, B. H., Luecken, D. J., Mao, J. Q., McLaren,
 1049 R., Mutzel, A., Osthoff, H. D., Ouyang, B., Picquet-Varrault, B., Platt, U., Pye, H. O. T., Rudich,

1050 Y., Schwantes, R. H., Shiraiwa, M., Stutz, J., Thornton, J. A., Tilgner, A., Williams, B. J., and
 1051 Zaveri, R. A.: Nitrate radicals and biogenic volatile organic compounds: oxidation, mechanisms,
 1052 and organic aerosol, *Atmos. Chem. Phys.*, 17, 2103-2162, 10.5194/acp-17-2103-2017, 2017.

1053 Nowak, J. B., Huey, L. G., Eisele, F. L., Tanner, D. J., Mauldin, R. L., Cantrell, C., Kosciuch, E.,
 1054 and Davis, D. D.: Chemical ionization mass spectrometry technique for detection of
 1055 dimethylsulfoxide and ammonia, *Journal of Geophysical Research-Atmospheres*, 107,
 1056 10.1029/2001jd001058, 2002.

1057 Nowak, J. B., Huey, L. G., Russell, A. G., Tian, D., Neuman, J. A., Orsini, D., Sjostedt, S. J.,
 1058 Sullivan, A. P., Tanner, D. J., Weber, R. J., Nenes, A., Edgerton, E., and Fehsenfeld, F. C.:
 1059 Analysis of urban gas phase ammonia measurements from the 2002 Atlanta Aerosol Nucleation
 1060 and Real-Time Characterization Experiment (ANARChE), *Journal of Geophysical Research-*
 1061 *Atmospheres*, 111, 14, 10.1029/2006jd007113, 2006.

1062 Orsini, D. A., Ma, Y. L., Sullivan, A., Sierau, B., Baumann, K., and Weber, R. J.: Refinements to
 1063 the particle-into-liquid sampler (PILS) for ground and airborne measurements of water soluble
 1064 aerosol composition, *Atmospheric Environment*, 37, 1243-1259, 10.1016/s1352-2310(02)01015-
 1065 4, 2003.

1066 Park Williams, A., Cook, B. I., Smerdon, J. E., Bishop, D. A., Seager, R., and Mankin, J. S.: The
 1067 2016 Southeastern U.S. Drought: An Extreme Departure From Centennial Wetting and Cooling,
 1068 *Journal of Geophysical Research: Atmospheres*, 122, 10,888-810,905, 10.1002/2017JD027523,
 1069 2017.

1070 Pechony, O., and Shindell, D. T.: Driving forces of global wildfires over the past millennium and
 1071 the forthcoming century, *Proceedings of the National Academy of Sciences of the United States*
 1072 *of America*, 107, 19167-19170, 10.1073/pnas.1003669107, 2010.

1073 Pye, H. O. T., Luecken, D. J., Xu, L., Boyd, C. M., Ng, N. L., Baker, K. R., Ayres, B. R., Bash, J.
 1074 O., Baumann, K., Carter, W. P. L., Edgerton, E., Fry, J. L., Hutzell, W. T., Schwede, D. B., and
 1075 Shepson, P. B.: Modeling the Current and Future Roles of Particulate Organic Nitrates in the
 1076 Southeastern United States, *Environmental Science & Technology*, 49, 14195-14203,
 1077 10.1021/acs.est.5b03738, 2015.

1078 Reis, S., Pinder, R. W., Zhang, M., Lijie, G., and Sutton, M. A.: Reactive nitrogen in atmospheric
 1079 emission inventories, *Atmos. Chem. Phys.*, 9, 7657-7677, 10.5194/acp-9-7657-2009, 2009.

1080 Sander, R.: Compilation of Henry's law constants (version 4.0) for water as solvent, *Atmos. Chem.*
 1081 *Phys.*, 15, 4399-4981, 10.5194/acp-15-4399-2015, 2015.

1082 Saxena, P., and Hildemann, L. M.: Water-soluble organics in atmospheric particles: A critical
 1083 review of the literature and application of thermodynamics to identify candidate compounds,
 1084 *Journal of Atmospheric Chemistry*, 24, 57-109, 10.1007/bf00053823, 1996.

1085 Saylor, R., Myles, L., Sibble, D., Caldwell, J., and Xing, J.: Recent trends in gas-phase ammonia
 1086 and PM_{2.5} ammonium in the Southeast United States, *Journal of the Air & Waste Management*
 1087 *Association*, 65, 347-357, 10.1080/10962247.2014.992554, 2015.

1088 Schrier, E. E., Pottle, M., and Scheraga, H. A.: The Influence of Hydrogen and Hydrophobic Bonds
 1089 on the Stability of the Carboxylic Acid Dimers in Aqueous Solution, *Journal of the American*
 1090 *Chemical Society*, 86, 3444-3449, 10.1021/ja01071a009, 1964.

1091 Seinfeld, J. H., and Pandis, S. N.: *Atmospheric chemistry and physics : from air pollution to*
 1092 *climate change*, Third edition. ed., John Wiley & Sons, Inc., Hoboken, New Jersey, xxvi, 1120
 1093 pages pp., 2016.

1094 Shi, G. L., Xu, J., Peng, X., Xiao, Z. M., Chen, K., Tian, Y. Z., Guan, X. B., Feng, Y. C., Yu, H.
 1095 F., Nenes, A., and Russell, A. G.: pH of Aerosols in a Polluted Atmosphere: Source Contributions
 1096 to Highly Acidic Aerosol, *Environmental Science & Technology*, 51, 4289-4296,
 1097 10.1021/acs.est.6b05736, 2017.

1098 Song, M., Marcolli, C., Krieger, U. K., Zuend, A., and Peter, T.: Liquid-liquid phase separation
 1099 and morphology of internally mixed dicarboxylic acids/ammonium sulfate/water particles, *Atmos.*
 1100 *Chem. Phys.*, 12, 2691-2712, 10.5194/acp-12-2691-2012, 2012.

1101 Song, S., Gao, M., Xu, W., Shao, J., Shi, G., Wang, S., Wang, Y., Sun, Y., and McElroy, M. B.:
 1102 Fine particle pH for Beijing winter haze as inferred from different thermodynamic equilibrium
 1103 models, *Atmos. Chem. Phys. Discuss.*, 2018, 1-26, 10.5194/acp-2018-6, 2018.

1104 Sorooshian, A., Ng, N. L., Chan, A. W. H., Feingold, G., Flagan, R. C., and Seinfeld, J. H.:
 1105 Particulate organic acids and overall water-soluble aerosol composition measurements from the
 1106 2006 Gulf of Mexico Atmospheric Composition and Climate Study (GoMACCS), *Journal of*
 1107 *Geophysical Research-Atmospheres*, 112, 16, 10.1029/2007jd008537, 2007.

1108 Sorooshian, A., Murphy, S. M., Hersey, S., Bahreini, R., Jonsson, H., Flagan, R. C., and Seinfeld,
 1109 J. H.: Constraining the contribution of organic acids and AMS m/z 44 to the organic aerosol
 1110 budget: On the importance of meteorology, aerosol hygroscopicity, and region, *Geophys. Res.*
 1111 *Lett.*, 37, 5, 10.1029/2010gl044951, 2010.

1112 Spaulding, R. S., Talbot, R. W., and Charles, M. J.: Optimization of a mist chamber (cofer
 1113 scrubber) for sampling water-soluble organics in air, *Environmental Science & Technology*, 36,
 1114 1798-1808, 10.1021/es011189x, 2002.

1115 Suarez-Bertoa, R., Zardini, A. A., and Astorga, C.: Ammonia exhaust emissions from spark
 1116 ignition vehicles over the New European Driving Cycle, *Atmospheric Environment*, 97, 43-53,
 1117 10.1016/j.atmosenv.2014.07.050, 2014.

1118 Sullivan, A. P., Weber, R. J., Clements, A. L., Turner, J. R., Bae, M. S., and Schauer, J. J.: A
 1119 method for on-line measurement of water-soluble organic carbon in ambient aerosol particles:
 1120 Results from an urban site, *Geophysical Research Letters*, 31, 10.1029/2004gl019681, 2004.

1121 Sun, K., Tao, L., Miller, D. J., Pan, D., Golston, L. M., Zondlo, M. A., Griffin, R. J., Wallace, H.
 1122 W., Leong, Y. J., Yang, M. M., Zhang, Y., Mauzerall, D. L., and Zhu, T.: Vehicle Emissions as an
 1123 Important Urban Ammonia Source in the United States and China, *Environmental Science &*
 1124 *Technology*, 51, 2472-2481, 10.1021/acs.est.6b02805, 2017.

1125 Updyke, K. M., Nguyen, T. B., and Nizkorodov, S. A.: Formation of brown carbon via reactions
 1126 of ammonia with secondary organic aerosols from biogenic and anthropogenic precursors,
 1127 *Atmospheric Environment*, 63, 22-31, 10.1016/j.atmosenv.2012.09.012, 2012.

1128 Van Damme, M., Clarisse, L., Heald, C. L., Hurtmans, D., Ngadi, Y., Clerbaux, C., Dolman, A.
 1129 J., Erisman, J. W., and Coheur, P. F.: Global distributions, time series and error characterization

1130 of atmospheric ammonia (NH₃) from IASI satellite observations, *Atmos. Chem. Phys.*, 14, 2905-
 1131 2922, 10.5194/acp-14-2905-2014, 2014.

1132 Warner, J. X., Wei, Z. G., Strow, L. L., Dickerson, R. R., and Nowak, J. B.: The global
 1133 tropospheric ammonia distribution as seen in the 13-year AIRS measurement record, *Atmos.*
 1134 *Chem. Phys.*, 16, 5467-5479, 10.5194/acp-16-5467-2016, 2016.

1135 Warner, J. X., Dickerson, R. R., Wei, Z., Strow, L. L., Wang, Y., and Liang, Q.: Increased
 1136 atmospheric ammonia over the world's major agricultural areas detected from space, *Geophysical*
 1137 *Research Letters*, 44, 2875-2884, 10.1002/2016gl072305, 2017.

1138 Weber, R. J., Orsini, D., Daun, Y., Lee, Y. N., Klotz, P. J., and Brechtel, F.: A particle-into-liquid
 1139 collector for rapid measurement of aerosol bulk chemical composition, *Aerosol Science and*
 1140 *Technology*, 35, 718-727, 10.1080/02786820152546761, 2001.

1141 Weber, R. J., Lee, S., Chen, G., Wang, B., Kapustin, V., Moore, K., Clarke, A. D., Mauldin, L.,
 1142 Kosciuch, E., Cantrell, C., Eisele, F., Thornton, D. C., Bandy, A. R., Sachse, G. W., and Fuelberg,
 1143 H. E.: New particle formation in anthropogenic plumes advecting from Asia observed during
 1144 TRACE-P, *Journal of Geophysical Research-Atmospheres*, 108, 13, 10.1029/2002jd003112,
 1145 2003.

1146 Weber, R. J., Guo, H., Russell, A. G., and Nenes, A.: High aerosol acidity despite declining
 1147 atmospheric sulfate concentrations over the past 15 years, *Nature Geoscience*, 9, 282-+,
 1148 10.1038/ngeo2665, 2016.

1149 Whittington, B. I., Jiang, C. J., and Trimm, D. L.: Vehicle exhaust catalysis: I. The relative
 1150 importance of catalytic oxidation, steam reforming and water-gas shift reactions, *Catalysis Today*,
 1151 26, 41-45, 10.1016/0920-5861(95)00093-u, 1995.

1152 Xing, J., Pleim, J., Mathur, R., Pouliot, G., Hogrefe, C., Gan, C. M., and Wei, C.: Historical
 1153 gaseous and primary aerosol emissions in the United States from 1990 to 2010, *Atmos. Chem.*
 1154 *Phys.*, 13, 7531-7549, 10.5194/acp-13-7531-2013, 2013.

1155 Xu, L., Guo, H., Boyd, C. M., Klein, M., Bougiatioti, A., Cerully, K. M., Hite, J. R., Isaacman-
 1156 VanWertz, G., Kreisberg, N. M., Knote, C., Olson, K., Koss, A., Goldstein, A. H., Hering, S. V.,

1157 de Gouw, J., Baumann, K., Lee, S.-H., Nenes, A., Weber, R. J., and Ng, N. L.: Effects of
 1158 anthropogenic emissions on aerosol formation from isoprene and monoterpenes in the southeastern
 1159 United States, *Proceedings of the National Academy of Sciences of the United States of America*,
 1160 112, 37-42, 10.1073/pnas.1417609112, 2015a.

1161 Xu, L., Suresh, S., Guo, H., Weber, R. J., and Ng, N. L.: Aerosol characterization over the
 1162 southeastern United States using high-resolution aerosol mass spectrometry: spatial and seasonal
 1163 variation of aerosol composition and sources with a focus on organic nitrates, *Atmos. Chem. Phys.*,
 1164 15, 7307-7336, 10.5194/acp-15-7307-2015, 2015b.

1165 Xu, L., Guo, H. Y., Weber, R. J., and Ng, N. L.: Chemical Characterization of Water-Soluble
 1166 Organic Aerosol in Contrasting Rural and Urban Environments in the Southeastern United States,
 1167 *Environmental Science & Technology*, 51, 78-88, 10.1021/acs.est.6b05002, 2017.

1168 Yao, X. H., Hu, Q. J., Zhang, L. M., Evans, G. J., Godri, K. J., and Ng, A. C.: Is vehicular emission
 1169 a significant contributor to ammonia in the urban atmosphere?, *Atmospheric Environment*, 80,
 1170 499-506, 10.1016/j.atmosenv.2013.08.028, 2013.

1171 You, Y., Renbaum-Wolff, L., and Bertram, A. K.: Liquid-liquid phase separation in particles
 1172 containing organics mixed with ammonium sulfate, ammonium bisulfate, ammonium nitrate or
 1173 sodium chloride, *Atmos. Chem. Phys.*, 13, 11723-11734, 10.5194/acp-13-11723-2013, 2013.

1174 You, Y., Kanawade, V. P., de Gouw, J. A., Guenther, A. B., Madronich, S., Sierra-Hernandez, M.
 1175 R., Lawler, M., Smith, J. N., Takahama, S., Ruggeri, G., Koss, A., Olson, K., Baumann, K., Weber,
 1176 R. J., Nenes, A., Guo, H., Edgerton, E. S., Porcelli, L., Brune, W. H., Goldstein, A. H., and Lee,
 1177 S. H.: Atmospheric amines and ammonia measured with a chemical ionization mass spectrometer
 1178 (CIMS), *Atmos. Chem. Phys.*, 14, 12181-12194, 10.5194/acp-14-12181-2014, 2014a.

1179 You, Y., Smith, M. L., Song, M., Martin, S. T., and Bertram, A. K.: Liquid-liquid phase separation
 1180 in atmospherically relevant particles consisting of organic species and inorganic salts, *International*
 1181 *Reviews in Physical Chemistry*, 33, 43-77, 10.1080/0144235x.2014.890786, 2014b.

1182 You, Y., and Bertram, A. K.: Effects of molecular weight and temperature on liquid-liquid phase
 1183 separation in particles containing organic species and inorganic salts, *Atmos. Chem. Phys.*, 15,
 1184 1351-1365, 10.5194/acp-15-1351-2015, 2015.

1185 Yu, H., and Lee, S. H.: Chemical ionisation mass spectrometry for the measurement of
 1186 atmospheric amines, *Environ. Chem.*, 9, 190-201, 10.1071/en12020, 2012.

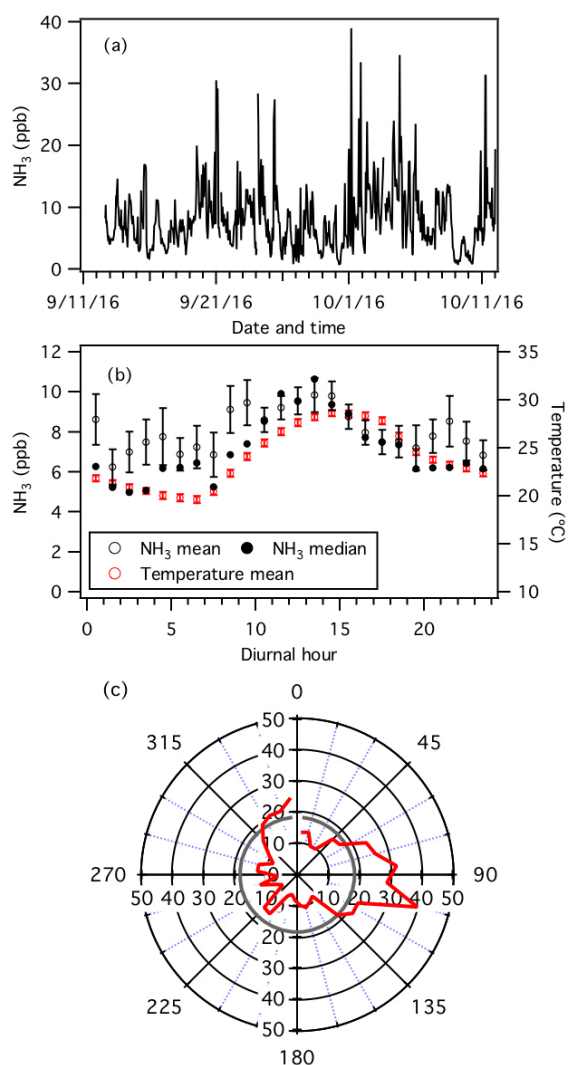
1187 Zhang, H. F., Yee, L. D., Lee, B. H., Curtis, M. P., Worton, D. R., Isaacman-VanWertz, G.,
 1188 Offenberg, J. H., Lewandowski, M., Kleindienst, T. E., Beaver, M. R., Holder, A. L., Lonneman,
 1189 W. A., Docherty, K. S., Jaoui, M., Pye, H. O. T., Hu, W. W., Day, D. A., Campuzano-Jost, P.,
 1190 Jimenez, J. L., Guo, H. Y., Weber, R. J., de Gouw, J., Koss, A. R., Edgerton, E. S., Brune, W.,
 1191 Mohr, C., Lopez-Hilfiker, F. D., Lutz, A., Kreisberg, N. M., Spielman, S. R., Hering, S. V., Wilson,
 1192 K. R., Thornton, J. A., and Goldstein, A. H.: Monoterpenes are the largest source of summertime
 1193 organic aerosol in the southeastern United States, *Proceedings of the National Academy of*
 1194 *Sciences of the United States of America*, 115, 2038-2043, 10.1073/pnas.1717513115, 2018.

1195 Zuend, A., Marcolli, C., Luo, B. P., and Peter, T.: A thermodynamic model of mixed organic-
 1196 inorganic aerosols to predict activity coefficients, *Atmos. Chem. Phys.*, 8, 4559-4593,
 1197 10.5194/acp-8-4559-2008, 2008.

1198 Zuend, A., Marcolli, C., Booth, A. M., Lienhard, D. M., Soonsin, V., Krieger, U. K., Topping, D.
 1199 O., McFiggans, G., Peter, T., and Seinfeld, J. H.: New and extended parameterization of the
 1200 thermodynamic model AIOMFAC: calculation of activity coefficients for organic-inorganic
 1201 mixtures containing carboxyl, hydroxyl, carbonyl, ether, ester, alkenyl, alkyl, and aromatic
 1202 functional groups, *Atmos. Chem. Phys.*, 11, 9155-9206, 10.5194/acp-11-9155-2011, 2011.

1203 Zuend, A., Marcolli, C., Luo, B. P., and Peter, T.: A thermodynamic model of mixed organic-
 1204 inorganic aerosols to predict activity coefficients (vol 8, pg 4559, 2008), *Atmos. Chem. Phys.*, 12,
 1205 10075-10075, 10.5194/acp-12-10075-2012, 2012.

1206

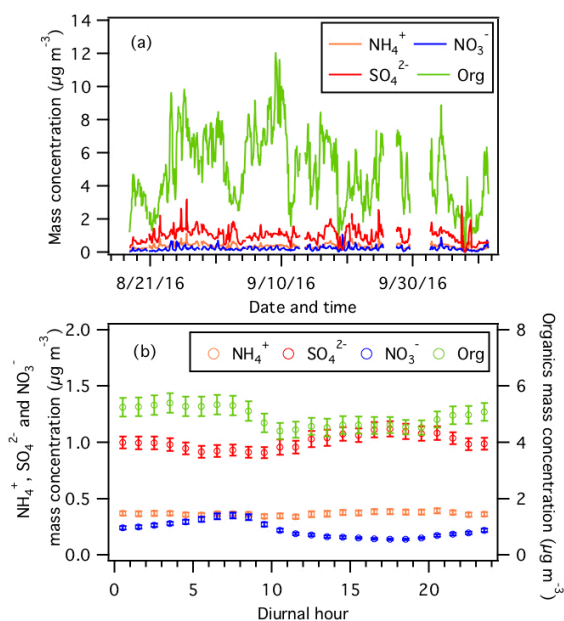


1207

1208 **Figure 1:** Measurements by the NH_3 -CIMS during the second half of the study. (a) Time series of
 1209 NH_3 concentration. The data is displayed as 1-hour averages. (b) Diurnal profiles of NH_3
 1210 concentration (mean and median) and temperature. Error bars shown are the standard errors. Dates
 1211 and times displayed are local time. All the concentrations represent averages in 1-hour intervals

1212 and the standard errors are plotted as error bars. (c) Average NH_3 concentration normalized to
 1213 wind speed (i.e., NH_3 concentration (ppb) x wind speed (m s^{-1})) in each 10 degrees bin (red line).
 1214 The average normalized NH_3 concentration is shown as a grey line.

Deleted: study-averaged



1216
 1217 **Figure 2:** (a) Time series and (b) diurnal profiles of non-refractory PM_1 species measured by the
 1218 AMS. Error bars shown in panel (b) are the standard errors. Dates and times displayed are local
 1219 time. All the mass concentrations shown here are obtained from scaling the raw data by 0.5. Refer
 1220 to the text for details.

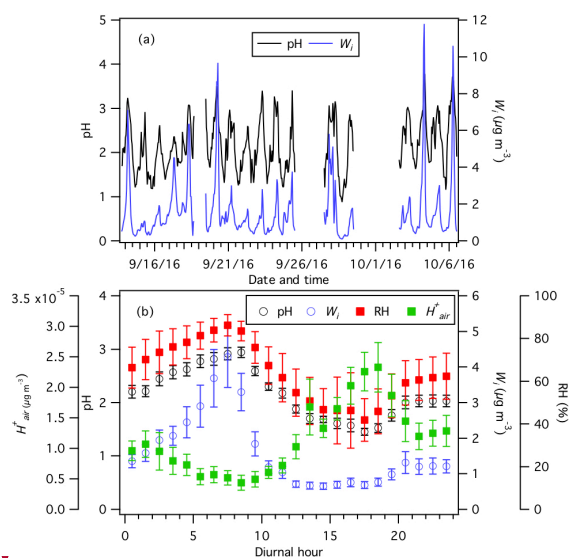
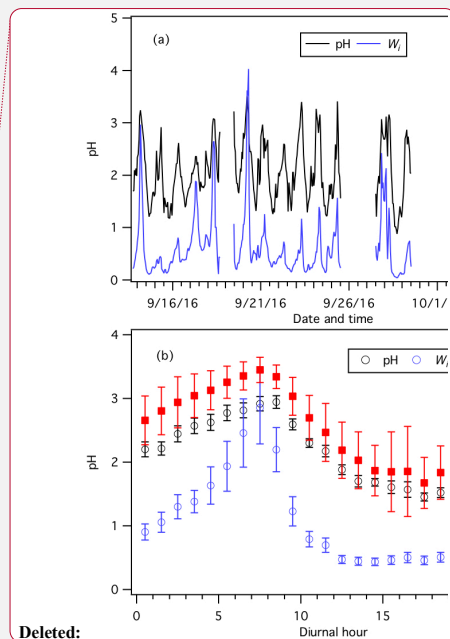
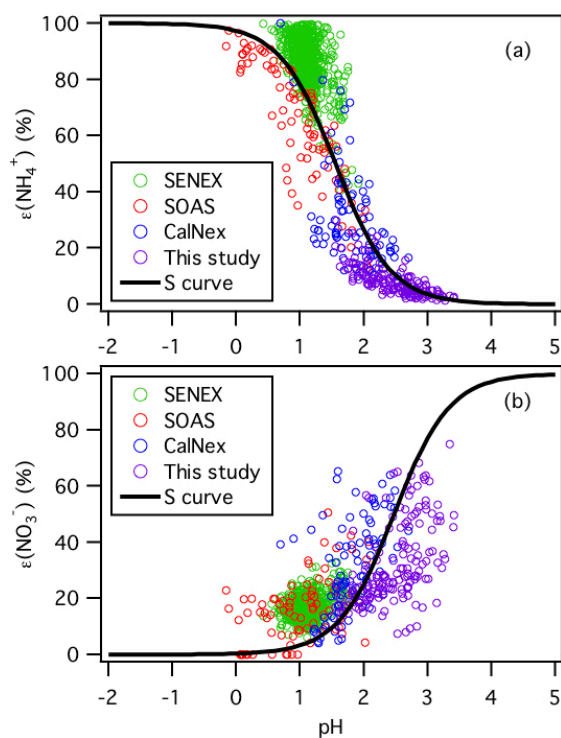


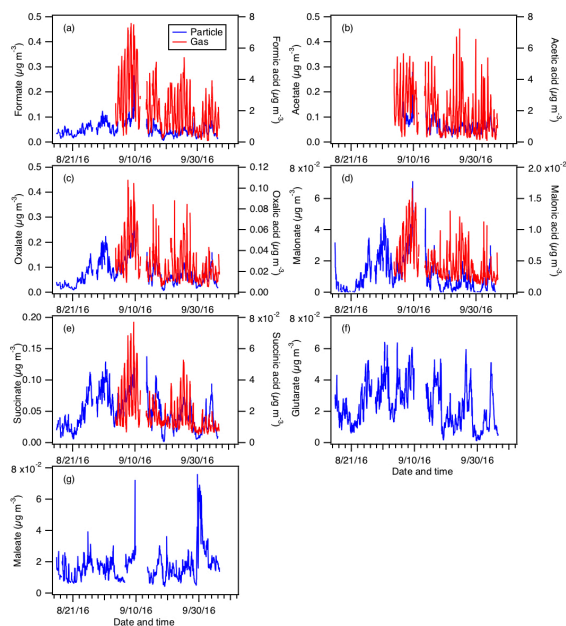
Figure 3: (a) Time series and (b) diurnal profiles of ISORROPIA-predicted PM_1 pH and W_i . The diurnal profiles of RH and ISORROPIA-predicted H^+_{air} are also shown in panel (b). Dates and times displayed are local time. All the data shown here represent averages in 1-hour intervals. Error bars shown in panel (b) are the standard errors.





1228

1229 **Figure 4:** Analytically calculated S curves of $\epsilon(\text{NH}_4^+)$ and $\epsilon(\text{NO}_3^-)$ and ambient data plotted
 1230 against ISORROPIA-predicted particle pH for this study, SENEX, SOAS and CalNex. For the
 1231 ambient datasets, a narrow range of W_i (1 to 4 $\mu\text{g m}^{-3}$) and temperature (15 to 25 $^\circ\text{C}$) are selected
 1232 to be close to the analytical calculation input (i.e., $W_i = 2.5 \mu\text{g m}^{-3}$ and temperature = 20 $^\circ\text{C}$).
 1233 Similar to Guo et al. (2017a), $\gamma_{\text{NH}_4^+} = 1$ and $\gamma_{\text{H}^+ - \text{NO}_3^-} = \sqrt{\gamma_{\text{H}^+} \gamma_{\text{NO}_3^-}} = 0.28$ are used for the
 1234 analytically calculated S curves.



1235

1236 **Figure 5:** Particle- and gas-phase measurements of (a) formic, (b) acetic, (c) oxalic, (d) malonic,
 1237 (e) succinic, (f) glutaric, and (g) maleic acids. Particle-phase measurements are shown on the left
 1238 y axes, while gas-phase measurements are shown on the right y axes. Dates and times displayed
 1239 are local time. Gas-phase measurements of glutaric and maleic acids are not available.

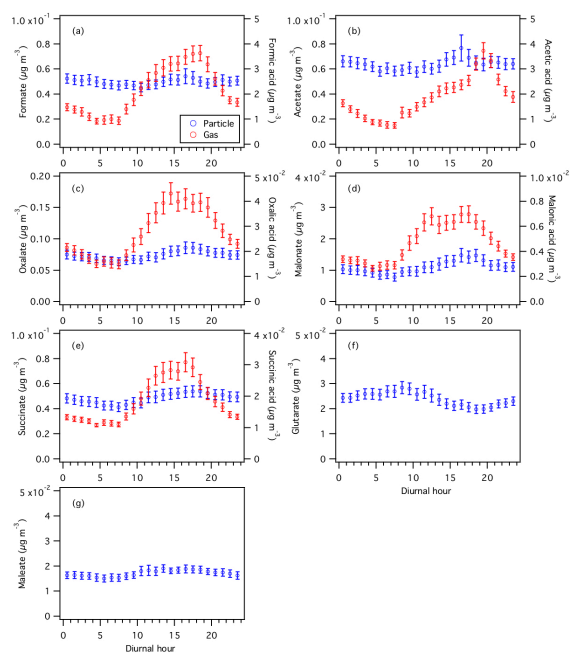
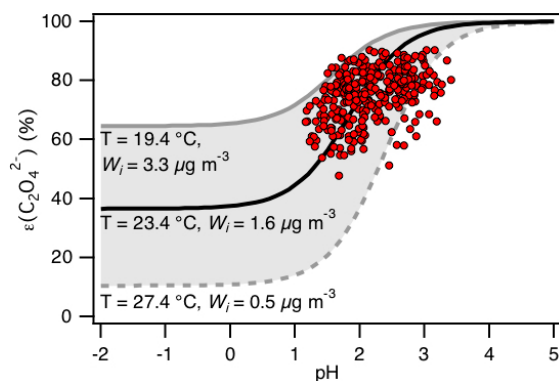
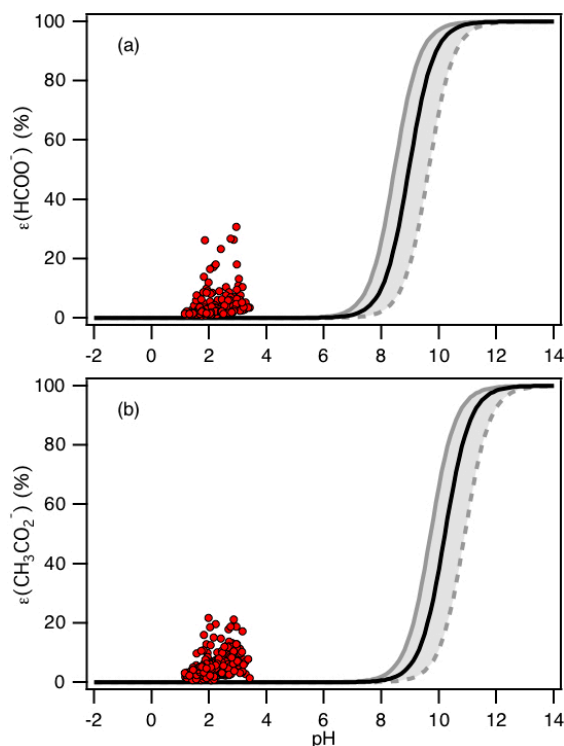


Figure 6: Diurnal profiles of particle- and gas-phase (a) formic, (b) acetic, (c) oxalic, (d) malonic, (e) succinic, (f) glutaric, and (g) maleic acids. Particle-phase measurements are shown on the left y axes, while gas-phase measurements are shown on the right y axes. All the data shown here represent averages in 1-hour intervals. Error bars shown are the standard errors.



1247

1248 **Figure 7:** Analytically calculated S curve of $\varepsilon(\text{C}_2\text{O}_4^{2-})$ and ambient data from 13 September to 6
 1249 October 2016 plotted against ISORROPIA-predicted particle pH. For the ambient data, a range in
 1250 W_i (0.5 to $4 \mu\text{g m}^{-3}$) and temperature (15 to $31 \text{ }^\circ\text{C}$) are chosen to be close to the analytically
 1251 calculated outputs. For the analytically calculated S curves, we used $\gamma_{\text{C}_2\text{H}_2\text{O}_4} = 0.0492$ (AIOMFAC
 1252 predicted). We also assumed that $\gamma_{\text{H}^+} + \gamma_{\text{C}_2\text{HO}_4^-} = \gamma_{\text{H}^+} + \gamma_{\text{NO}_3^-}$, and used the ISORROPIA-predicted
 1253 $\gamma_{\text{H}^+ - \text{NO}_3^-} = \sqrt{\gamma_{\text{H}^+} + \gamma_{\text{NO}_3^-}} = 0.265$. The black line is the S curve calculated using the selected time
 1254 period's average temperature ($23.4 \pm 4.0 \text{ }^\circ\text{C}$) and W_i ($1.6 \pm 1.7 \mu\text{g m}^{-3}$). The grey lines are S curves
 1255 calculated using one standard deviation from the average temperature and W_i (i.e., temperature =
 1256 $27.4 \text{ }^\circ\text{C}$ and $W_i = 0.5 \mu\text{g m}^{-3}$ for dotted grey line, temperature = $19.4 \text{ }^\circ\text{C}$ and $W_i = 3.3 \mu\text{g m}^{-3}$ for
 1257 solid grey line).



1258

1259 **Figure 8:** Analytically calculated S curves of $\epsilon(\text{HCOO}^-)$ and $\epsilon(\text{CH}_3\text{CO}_2^-)$ (solid black lines) and
 1260 ambient data from 13 September to 6 October 2016 plotted against ISORROPIA-predicted particle
 1261 pH (shown in panels (a) and (b), respectively). For the ambient data, a narrow range in W_i (0.5 to
 1262 $4 \mu\text{g m}^{-3}$) and RH (20 to 90 %) is chosen to be close to the analytically calculated outputs. For the
 1263 analytically calculated S curves, we used $\gamma_{\text{HCOOH}} = 0.334$ and $\gamma_{\text{CH}_3\text{COOH}} = 2.150$ (AIOMFAC
 1264 predicted). We also assumed that $\gamma_{\text{H}^+} + \gamma_{\text{HCOO}^-} = \gamma_{\text{H}^+} + \gamma_{\text{CH}_3\text{COO}^-} = \gamma_{\text{H}^+} + \gamma_{\text{NO}_3^-}$, and used the
 1265 ISORROPIA-predicted $\gamma_{\text{H}^+ + \text{NO}_3^-} = \sqrt{\gamma_{\text{H}^+} + \gamma_{\text{NO}_3^-}} = 0.265$. The black lines are S curves calculated
 1266 using the selected time period's average temperature ($23.4 \pm 4.0 \text{ }^\circ\text{C}$) and W_i ($1.6 \pm 1.7 \mu\text{g m}^{-3}$).
 1267 The grey lines are S curves calculated using one standard deviation from the average temperature
 1268 and W_i (i.e., temperature = $27.4 \text{ }^\circ\text{C}$ and $W_i = 0.5 \mu\text{g m}^{-3}$ for dotted grey line, temperature = 19.4
 1269 $^\circ\text{C}$ and $W_i = 3.3 \mu\text{g m}^{-3}$ for solid grey line).

Table 1: Comparisons between different field campaigns for particle pH, major inorganic ions and gases and meteorological conditions. All pH values were calculated using ISORROPIA-II run in forward mode. These statistics were previously compiled by Guo et al. (2017a). Campaign acronyms used here stand for the California Research at the Nexus of Air Quality and Climate Change (CalNex), Southern Oxidant and Aerosol Study (SOAS), and Southeastern Nexus of Air Quality and Climate (SENEX).

Campaign	CalNex		SOAS	SENEX	This study
Type	Ground		Ground	Aircraft	Ground
PM cut size	PM ₁	PM _{2.5} ^a	PM ₁ &PM _{2.5} ^b	PM ₁	PM ₁
Year	2010		2013	2013	2016
Season	(Early Summer)		Summer	Summer	Fall
Region/Location	SW US		SE US	SE US	SE US
SO ₄ ²⁻ , $\mu\text{g m}^{-3}$	2.86 ± 1.70	1.88 ± 0.69	1.73 ± 1.21	2.05 ± 0.80	1.6 ± 0.4
NO ₃ ⁻ , $\mu\text{g m}^{-3}$	3.58 ± 3.65	3.74 ± 1.53	0.08 ± 0.08	0.28 ± 0.09	0.20 ± 0.10
HNO ₃ , $\mu\text{g m}^{-3}$	6.65 ± 7.03	4.45 ± 3.59	0.36 ± 0.14	1.35 ± 0.66	0.50 ± 0.26
$\epsilon(\text{NO}_3^-)$	39 ± 16 %	51 ± 18 %	22 ± 16 %	18 ± 6 %	26 ± 15 %
Total NO ₃ ⁻ , $\mu\text{g m}^{-3}$	10.22 ± 9.74	8.19 ± 3.89	0.45 ± 0.26	1.63 ± 0.70	0.70 ± 0.28
NH ₄ ⁺ , $\mu\text{g m}^{-3}$	2.06 ± 1.67	1.79 ± 0.65	0.46 ± 0.34	1.06 ± 0.25	0.40 ± 0.20
NH ₃ , $\mu\text{g m}^{-3}$	1.37 ± 0.90	0.75 ± 0.61	0.39 ± 0.25	0.12 ± 0.19	5.79 ± 3.67
$\epsilon(\text{NH}_4^+)$	55 ± 25%	71 ± 19%	50 ± 25%	92 ± 11%	7 ± 5 %
Total NH ₄ ⁺ , $\mu\text{g m}^{-3}$	3.44 ± 1.81	2.54 ± 0.89	0.78 ± 0.50	1.17 ± 0.81	6.19 ± 3.68
Na ⁺ , $\mu\text{g m}^{-3}$	\	0.77 ± 0.39	0.03 ± 0.07	\	\
Cl ⁻ , μgm^{-3}	\	0.64 ± 0.48	0.02 ± 0.03	\	0.01 ± 0.01
RH, %	79 ± 17	87 ± 9	74 ± 16	72 ± 9	69 ± 18
T, °C	18 ± 4	18 ± 3	25 ± 3	22 ± 3	24 ± 4
W _i , $\mu\text{g m}^{-3}$	13.9 ± 18.1	29.8 ± 20.7	5.1 ± 3.8	3.2 ± 2.8	1.6 ± 1.7
pH	1.9 ± 0.5	2.7 ± 0.3	0.9 ± 0.6	1.1 ± 0.4	2.2 ± 0.6
Reference	(Guo et al., 2017a)		(Guo et al., 2015)	(Xu et al., 2016)	This study

^aOnly during the last week of CalNex.

^bPM_{2.5} was sampled in the first half and PM₁ sampled in the second half of the study. Various parameters were similar in both cases. Crustal components were higher, but are overall generally in low concentrations so the differences had minor effects. For example, PM_{2.5} Na⁺ was 0.06 ± 0.09 $\mu\text{g m}^{-3}$ and PM₁ Na⁺ was 0.01 ± 0.01 $\mu\text{g m}^{-3}$.

1 **Characterization of Aerosol Composition, Aerosol Acidity and Organic Acid Partitioning at**
2 **an Agriculture-Intensive Rural Southeastern U.S. Site**

3
4 Theodora Nah,¹ Hongyu Guo,¹ Amy P. Sullivan,² Yunle Chen,¹ David J. Tanner,¹ Athanasios
5 Nenes,^{1,3,4,5} Armistead Russell,⁶ Nga Lee Ng,^{1,3} L. Gregory Huey¹ and Rodney J. Weber^{1,*}

6
7 ¹*School of Earth and Atmospheric Sciences, Georgia Institute of Technology, Atlanta, GA, USA*

8 ²*Department of Atmospheric Science, Colorado State University, Fort Collins, CO, USA*

9 ³*School of Chemical and Biomolecular Engineering, Georgia Institute of Technology, Atlanta, GA, USA*

10 ⁴*ICE-HT, Foundation for Research and Technology, Hellas, 26504 Patras, Greece*

11 ⁵*IERSD, National Observatory of Athens, P. Penteli, 15236, Athens, Greece*

12 ⁶*School of Civil and Environmental Engineering, Georgia Institute of Technology, Atlanta, GA, USA*

13

14

15

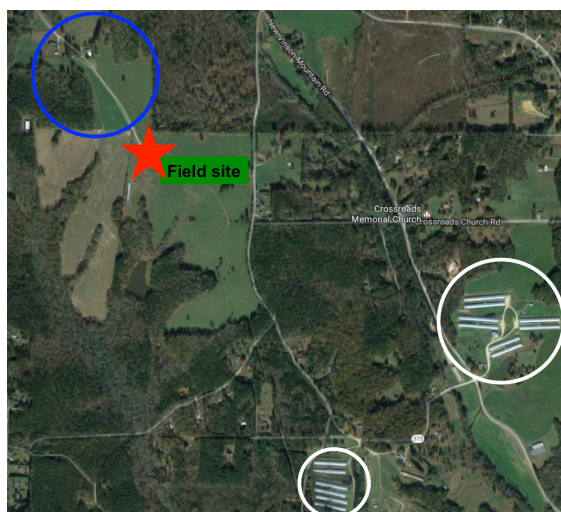
16

17

18

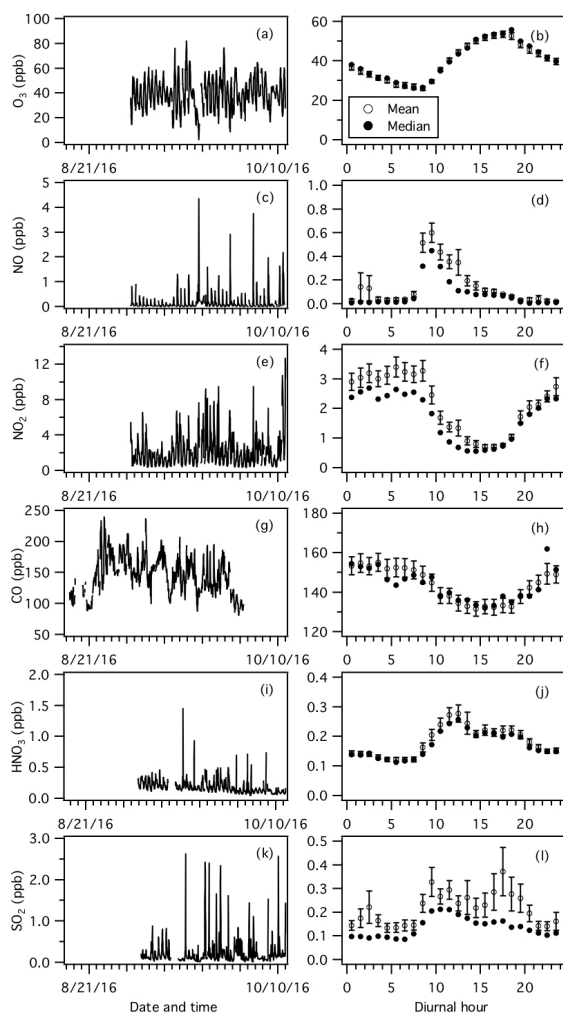
19

20



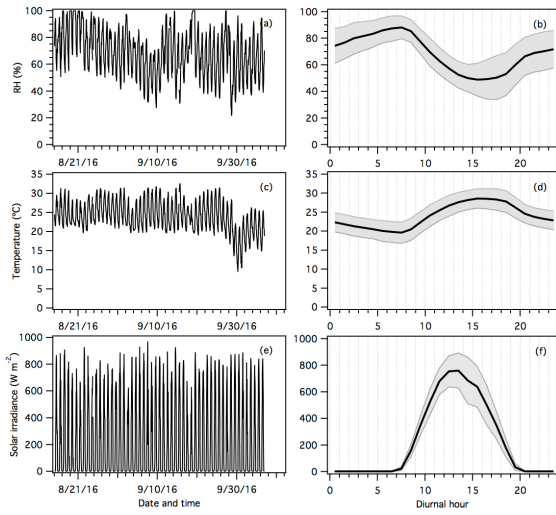
21

22 **Figure S1:** Map of the Yorkville field site (marked by the red diamond) and its surrounding areas
 23 (from Google Maps). Locations of nearby cattle-grazing pastures (north-west direction) and
 24 poultry CAFOs (south-east direction) are marked by the blue and white circles, respectively.



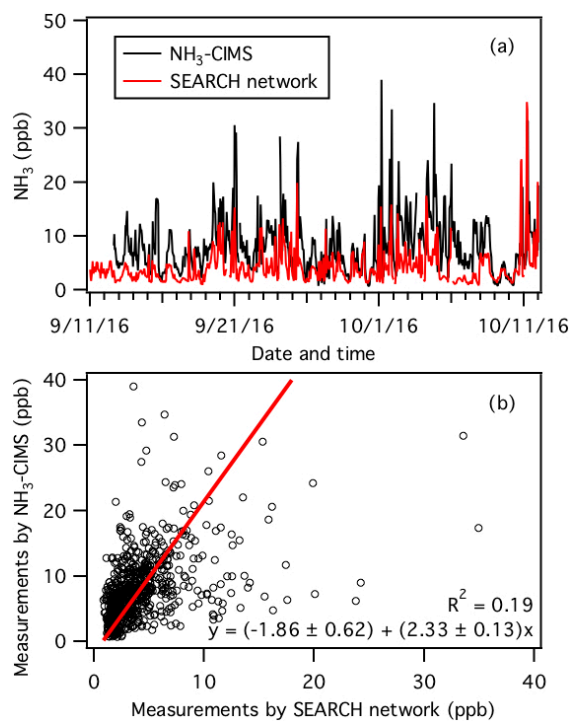
25

26 **Figure S2:** Time series and diurnal profiles of (a and b) O₃, (c and d) NO, (e and f) NO₂, (g and
 27 h) CO, (i and j) HNO₃, and (k and l) SO₂. Dates and times displayed are local time. All the
 28 concentrations represent averages in 1-hour intervals and the standard errors are plotted as error
 29 bars. O₃, NO, NO₂ and CO measurements were provided by the SEARCH network. HNO₃ and
 30 SO₂ were measured by the SF₆-CIMS.



31

32 **Figure S3:** Time series and diurnal profiles of (a and b) RH, (c and d) temperature, and (e and f)
 33 solar irradiance. Dates and times displayed are local time. In panels b, d and f, the lines within the
 34 shaded area represents the average values. The upper and lower boundaries of the shaded areas
 35 mark one standard deviation. RH, temperature and solar irradiance measurements were provided
 36 by the SEARCH network.



37

38 **Figure S4:** (a) Time series of NH_3 concentrations measured by the NH_3 -CIMS and denuder-based
 39 instrument operated by the SEARCH network. (b) Comparison of NH_3 concentrations measured
 40 by the NH_3 -CIMS and denuder-based instrument. The red line is the orthogonal distance regression
 41 fit to the data. All the data are displayed as 1-hour averages.

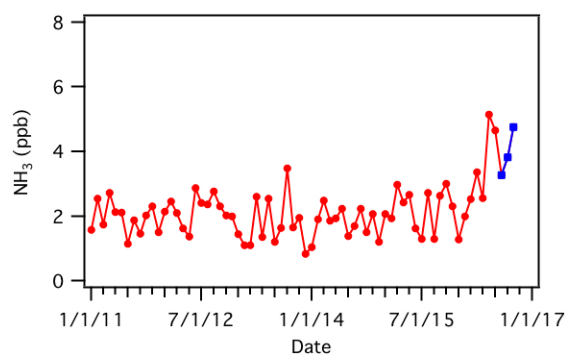


Figure S5: Monthly-averaged NH₃ concentrations at the Yorkville SEARCH monitoring site for 2011 to 2016. These measurements were made using the denuder-based instrument operated by the SEARCH network. Concentrations measured during this study (mid-August to mid-October 2016) are shown in blue.

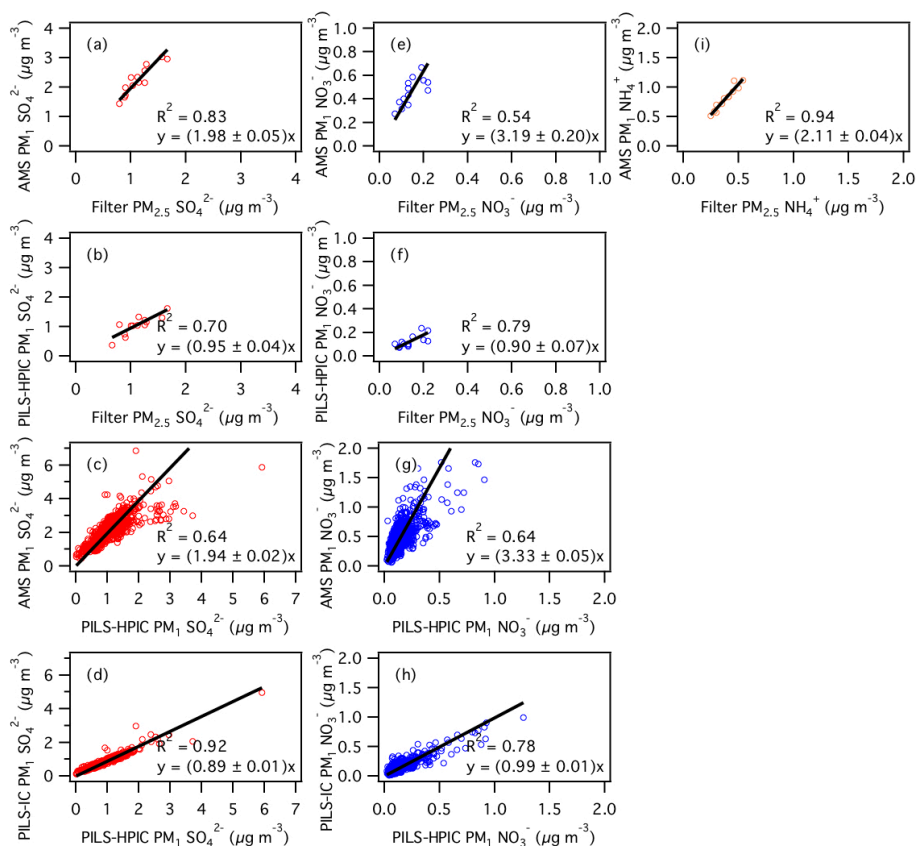


Figure S6: Aerosol (panels a to d) SO_4^{2-} , (panels e to h) NO_3^- , and (i) NH_4^+ comparisons between HR-ToF-AMS, PILS-IC, PILS-HPIC and filters for the entire field study. CDCE values were applied to the raw HR-ToF-AMS data to obtain the mass concentrations shown here (see main text for details). For comparisons between the HR-ToF-AMS, PILS-IC and PILS-HPIC data (panels c, d, g and h), the measurements are averaged over 1 hour intervals. For comparisons with filter data (panels a, b, e, f and i), the HR-ToF-AMS, PILS-IC and PILS-HPIC data are averaged over 24 hour intervals. Orthogonal regression fits are shown. Uncertainties in the fits are 1 standard deviation.

Deleted: AMS

Deleted: AMS

Deleted: AMS

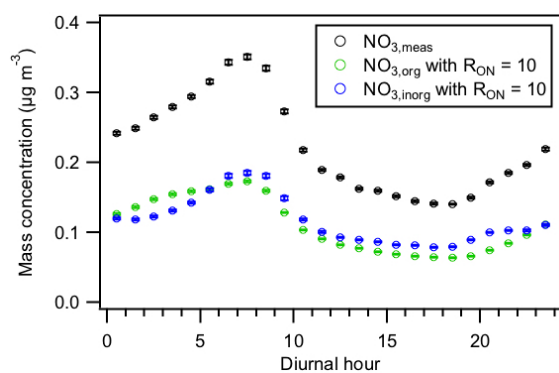


Figure S7: Diurnal profiles of the total nitrate functionality contributed by organic and inorganic nitrates ($\text{NO}_{3,\text{meas}}$), and the nitrate functionality solely from organic nitrates ($\text{NO}_{3,\text{org}}$) and inorganic nitrates ($\text{NO}_{3,\text{inorg}}$). $\text{NO}_{3,\text{org}}$ and $\text{NO}_{3,\text{inorg}}$ are estimated using the $\text{NO}^+/\text{NO}_2^+$ ratio method as described by Farmer et al. (2010) and Xu et al. (2015). Similar to Xu et al. (2015), we used a R_{ON} (defined here as the $\text{NO}^+/\text{NO}_2^+$ ratio for organic nitrates) value of 10 to calculate $\text{NO}_{3,\text{org}}$ and $\text{NO}_{3,\text{inorg}}$. All the data shown here represent averages in 1-hour intervals. Error bars shown are the standard errors.

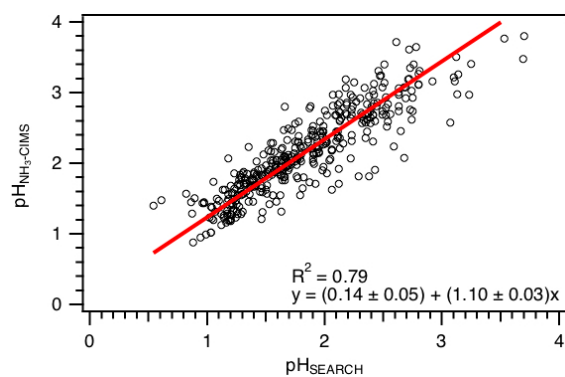
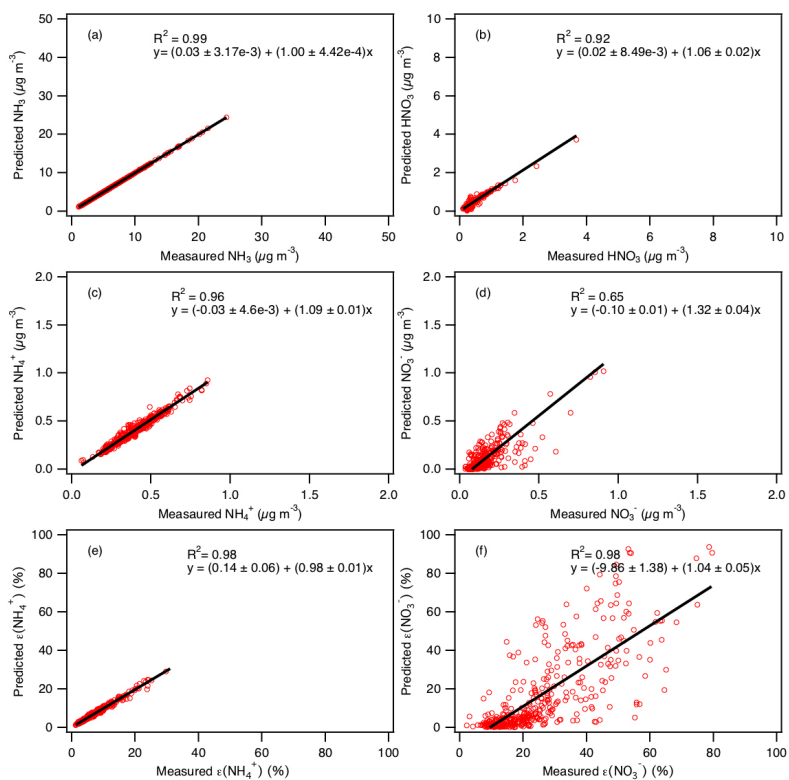


Figure S8: Comparison of predicted PM_{10} pH values determined using NH_3 -CIMS and SEARCH network's NH_3 measurements as ISORROPIA-II model inputs. The other model inputs are the same. The linear fit is obtained by orthogonal distance regression.

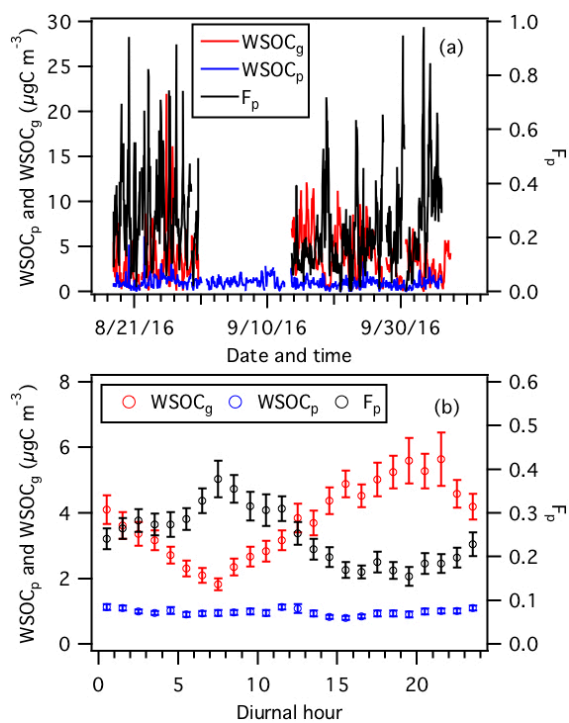
Deleted: S7



80

81 **Figure S9:** Comparisons of predicted and measured (a) NH_3 , (b) HNO_3 , (c) NH_4^+ , (d) NO_3^- , (e)
 82 $\epsilon(\text{NH}_4^+)$, and (f) $\epsilon(\text{NO}_3^-)$. Orthogonal regression fits are shown. Uncertainties in the fits are 1
 83 standard deviation.

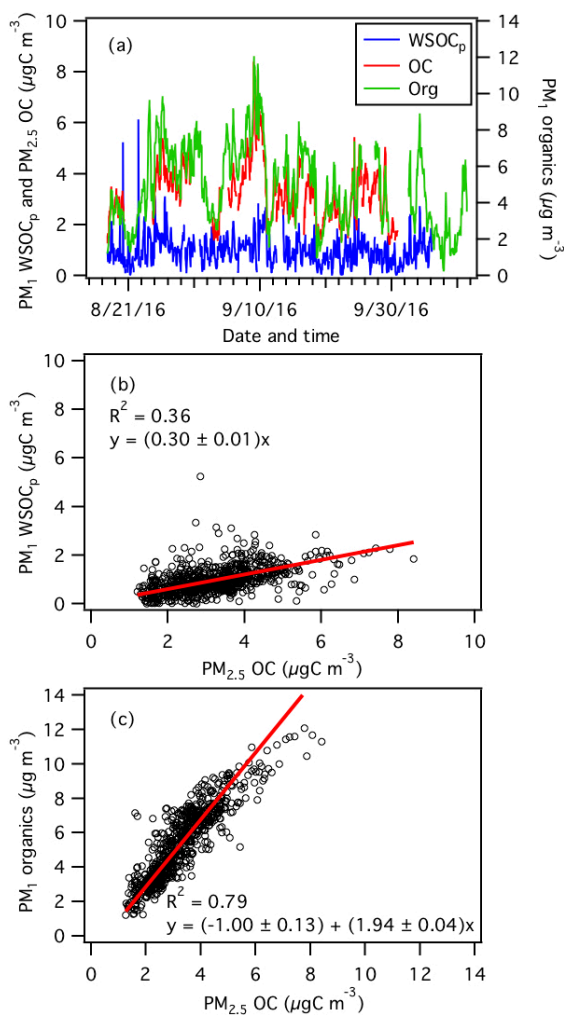
Deleted: S8



85

86 **Figure S10:** (a) Time series and (b) diurnal profiles of WSOC_g, WSOC_p and F_p. Dates and times
 87 displayed are local time. All the data shown here represent averages in 1-hour intervals. Error bars
 88 shown in panel (b) are the standard errors. $F_p = \text{WSOC}_p / (\text{WSOC}_p + \text{WSOC}_g)$.

Deleted: S9



90

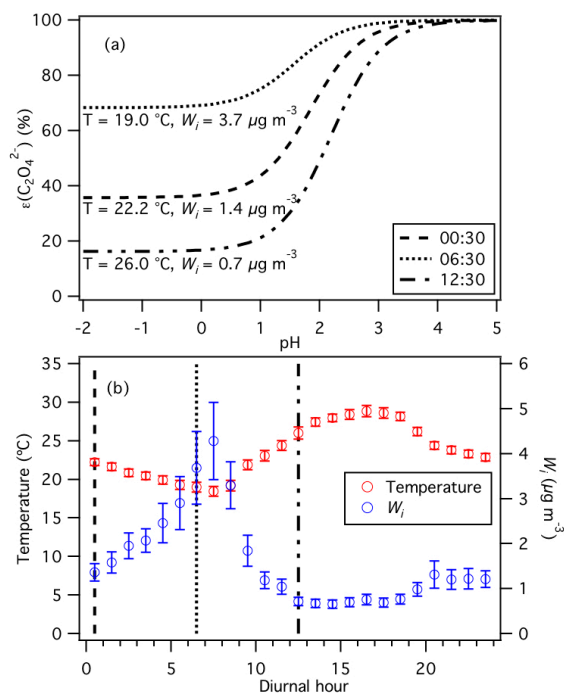
91 **Figure S11:** (a) Time series of **HR-ToF-AMS**, organics, WSOC_p and OC. (b) Linear regression
 92 correlation between WSOC_p and OC. (c) Linear regression correlation between **HR-ToF-AMS**,
 93 organics and OC. All the data shown here represent averages in 1-hour intervals. Note that OC
 94 measurements are PM_{2.5}, while WSOC_p and **HR-ToF-AMS**, organics measurements are PM₁.
 95 Linear fits are obtained by orthogonal distance regression.

Deleted: S10

Deleted: AMS

Deleted: AMS

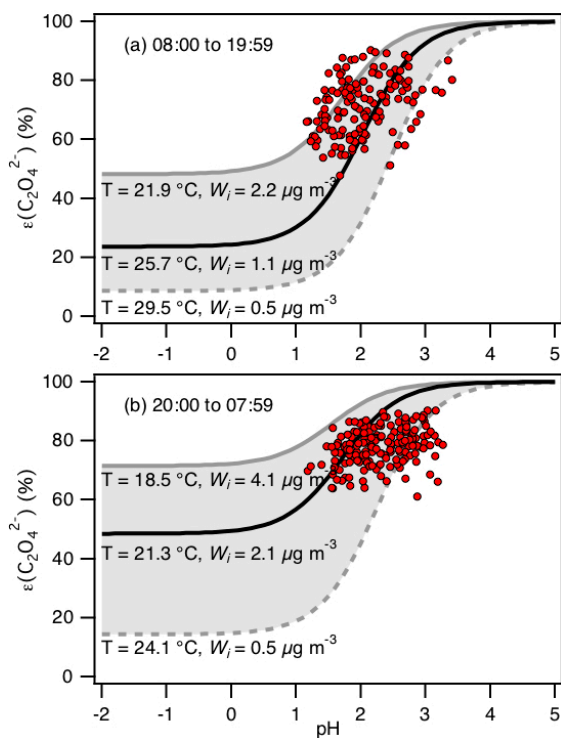
Deleted: AMS



100

101 **Figure S12:** (a) Analytically calculated S curves of $\epsilon(\text{C}_2\text{O}_4^{2-})$ at different times of the day: 00:30,
 102 06:30 and 12:30. These S curves are calculated using values obtained from (b) the diurnal profiles
 103 of temperature and W_i . The set of 1-hour average temperatures and W_i at diurnal hours 00:30,
 104 06:30 and 12:30 is used to calculate each S curve shown in panel (a). Similar to Fig. 7, we used
 105 $\gamma_{\text{C}_2\text{H}_2\text{O}_4} = 0.0492$ (AIOMFAC predicted) and assumed that $\gamma_{\text{H}^+ - \text{NO}_3^-} = \sqrt{\gamma_{\text{H}^+} \gamma_{\text{NO}_3^-}} = \sqrt{\gamma_{\text{H}^+} \gamma_{\text{C}_2\text{HO}_4^-}}$
 106 $= 0.265$ (ISORROPIA-II predicted) to generate these S curves.

Deleted: S11



108

109 **Figure S13:** Analytically calculated S curve of $\epsilon(\text{C}_2\text{O}_4^{2-})$ and ambient data from 13 September to
 110 6 October 2016 plotted against ISORROPIA-predicted particle pH. For the ambient data, a narrow
 111 range in W_i (0.5 to $4 \mu\text{g m}^{-3}$) and RH (20 to 90 %) is chosen to be close to the analytically calculated
 112 outputs. We divided the ambient data into two sets: panel (a) 08:00 to 19:59, and panel (b) 20:00
 113 to 07:59. For both analytically calculated S curves, we used $\gamma_{\text{C}_2\text{H}_2\text{O}_4} = 0.0492$ (AIOMFAC
 114 predicted). We also assumed that $\gamma_{\text{H}^+} + \gamma_{\text{C}_2\text{HO}_4^-} = \gamma_{\text{H}^+} + \gamma_{\text{NO}_3^-}$, and used the ISORROPIA-predicted
 115 $\gamma_{\text{H}^+ - \text{NO}_3^-} = \sqrt{\gamma_{\text{H}^+} + \gamma_{\text{NO}_3^-}} = 0.265$. In panel (a), we used the average temperature and W_i (25.7 ± 3.8
 116 $^\circ\text{C}$ and $1.1 \pm 1.1 \mu\text{g m}^{-3}$) for the data between 08:00 to 19:59 to calculate the S curve (black line).
 117 In panel (b), we used the average temperature and W_i (21.3 ± 2.8 $^\circ\text{C}$ and $2.1 \pm 2.0 \mu\text{g m}^{-3}$) for the
 118 data between 20:00 to 07:59 to calculate the S curve (black line). Grey lines in both panels are S
 119 curves calculated using one standard deviation from the average temperature and W_i for the two

Deleted: S12

121 datasets. In panel (a), the dotted grey line is the S curve calculated using 29.5 °C and 0.5 $\mu\text{g m}^{-3}$
122 while the solid grey line is the S curve calculated using 21.9 °C and 2.2 $\mu\text{g m}^{-3}$. In panel (b), the
123 dotted grey line is the S curve calculated using 24.1 °C and 0.5 $\mu\text{g m}^{-3}$ while the solid grey line is
124 the S curve calculated using 18.5 °C and 4.1 $\mu\text{g m}^{-3}$.

125

126

127

128

129

130

131

132

133

134

135

136

137

138

139

140

141

142

143 **Table S1:** List of gas-phase acids measured by SF₆-CIMS, and their measurement uncertainties
 144 and detection limits.

Acid	Measurement uncertainty (%)	Detection limits (ppb) ^a
Nitric acid	13	0.20
Formic acid	12	0.03
Acetic acid	12	0.06
Oxalic acid	14	1×10^{-3}
Butyric acid	14	0.03
Glycolic acid	22	2×10^{-3}
Propionic acid	14	6×10^{-3}
Valeric acid	22	0.01
Malonic acid	25	7×10^{-4}
Succinic acid	25	3×10^{-3}

145 ^aDetection limits are approximated from 3 times the standard deviation values (3σ) of the ion
 146 signals measured during background mode. Shown here are the average detection limits of the
 147 organic acids for 2.5 min integration periods which corresponds to the length of a background
 148 measurement at a 0.04 s duty cycle for each mass.

149

150

151

152

153

154

155

156

157

158

159

160

161

162 S1. SF₆-CIMS calibration of gas-phase HNO₃ and organic acids

163 Detailed descriptions of post-field laboratory calibrations of HNO₃, oxalic, butyric,
164 glycolic, propionic, valeric, malonic and succinic acids can be found in Nah et al. (2018). The
165 response of the CIMS acid signals were measured relative to the sensitivity of ³⁴SO₂ in these
166 calibration measurements.

167 The HNO₃ calibration source was a permeation tube (KIN-TEK) whose emission rate was
168 measured using UV optical absorption (Neuman et al., 2003). Solid or liquid samples of oxalic
169 (Sigma Aldrich, ≥ 99 %), butyric (Sigma Aldrich, ≥ 99 %), glycolic (Sigma Aldrich, 99 %),
170 propionic (Sigma Aldrich, ≥ 99.5 %), valeric (Sigma Aldrich, ≥ 99 %), malonic (Sigma Aldrich,
171 ≥ 99.5 %) and succinic (Sigma Aldrich, 99 %) acids were used in calibration measurements. The
172 acid sample was placed in a glass impinger, which was immersed in a water bath at a fixed
173 temperature to provide a constant vapor pressure. For oxalic, butyric, glycolic, propionic and
174 valeric acids, the water bath temperature was set to 0 °C. For malonic and succinic acids, the water
175 bath temperature was set to 40 °C in order to generate large enough gas phase concentrations for
176 calibration. 6 to 10 mL min⁻¹ of nitrogen gas (N₂) was passed over the organic acid in the glass
177 impinger. This organic acid air stream was diluted with different N₂ flows (1 to 5 L min⁻¹) to obtain
178 different mixing ratios of the organic acid. We calculated the mixing ratios based on the acid's
179 emission rate from the impinger or the acid's vapor pressure. Emission rates of gas-phase oxalic,
180 malonic and succinic acids from the impinger were measured by scrubbing the output of the
181 impinger in deionized water, followed by ion chromatography analysis. We measured the vapor
182 pressures of butyric and propionic acids at 0 °C using a capacitance manometer (MKS
183 Instruments). We estimated the vapor pressures of glycolic and valeric acids at 0 °C using their
184 literature vapor pressures at 25 °C and enthalpies of vaporization (Daubert and Danner, 1989; Lide,
185 1995; Acree and Chickos, 2010).

186 S2. WSOC_p and OC

187 We estimated the water-soluble fraction of OC by comparing the WSOC_p and OC
188 measurements. The time series of organics, WSOC_p and OC are shown in Fig. S11a. As shown in
189 Fig. S11b, WSOC_p is moderately correlated with OC at the site. The orthogonal distance regression
190 fit suggests that 30 % of the OC is water-soluble (estimated measurement uncertainty of 19 %),

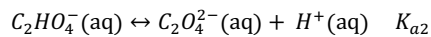
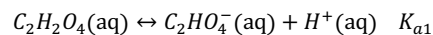
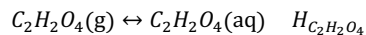
Deleted: S10a

Deleted: S10b

which is significantly smaller than the fraction (61 %) measured during the SOAS study (Xu et al., 2017). This difference may be due, in part, to the WSOC_p/OC ratio for this study being underestimated. WSOC_p are PM₁ measurements while OC are PM_{2.5} measurements. This is in contrast to the SOAS study where both WSOC_p and OC are PM_{2.5} measurements. PM₁ organics mass concentration is highly correlated with OC and has an orthogonal distance regression slope of 1.94 (Fig. S9c), which is similar to the value (1.92) reported for the SOAS study (Xu et al., 2017).

S3. C₂H₂O₄- C₂O₄²⁻ partitioning

Here, we show the detailed derivation of equation (4) in that paper. Equilibrium between gaseous C₂H₂O₄ and particle-phase C₂O₄²⁻ involves the dissolution of C₂H₂O₄ into the aqueous phase (assuming particles are liquids), followed by dissociation of the dissolved C₂H₂O₄:



for which the reaction equilibriums are expressed as follows:

$$H_{C_2H_2O_4} = \gamma_{C_2H_2O_4} [C_2H_2O_4] / p_{C_2H_2O_4} \quad (1)$$

$$K_{a1} = \frac{\gamma_{H^+} [H^+] \gamma_{C_2HO_4^-} [C_2HO_4^-]}{\gamma_{C_2H_2O_4} [C_2H_2O_4]} \quad (2)$$

$$K_{a2} = \frac{\gamma_{H^+} [H^+] \gamma_{C_2O_4^{2-}} [C_2O_4^{2-}]}{\gamma_{C_2HO_4^-} [C_2HO_4^-]} \quad (3)$$

where $H_{C_2H_2O_4}$ (mole L⁻¹ atm⁻¹) is the Henry's law constant for oxalic acid, K_{a1} and K_{a2} (mole L⁻¹) are the first and second acid dissociation constants for oxalic acid, $p_{C_2H_2O_4}$ (atm) is the partial pressure of oxalic acid in the atmosphere, and γ_i 's are activity coefficients. In equations (1) to (3), [x] represents aqueous concentrations (mole L⁻¹).

The total dissolved C₂H₂O₄ or particle-phase oxalate ($C_2O_4^T$) can be expressed as:

$$[C_2HO_4^T] = [C_2H_2O_4] + [C_2HO_4^-] + [C_2O_4^{2-}] \quad (4)$$

216 Using equations (1) to (3), $[C_2O_4^{T}]$ can be expressed as:

$$217 \quad [C_2O_4^T] = H_{C_2H_2O_4} p_{C_2H_2O_4} \left(\frac{1}{\gamma_{C_2H_2O_4}} + \frac{K_{a1}}{\gamma_{H^+} + \gamma_{C_2HO_4^-} [H^+]} + \frac{K_{a1}K_{a2}}{\gamma_{H^+} + \gamma_{H^+} + \gamma_{C_2O_4^{2-}} [H^+]^2} \right) \quad (5)$$

218 The ideal gas law gives:

$$219 \quad c(C_2H_2O_4) = \frac{p_{C_2H_2O_4}}{RT} \quad (6)$$

220 where R is the gas constant, T is temperature, and $c(x)$ represents concentration per volume of air
221 (mole m^{-3}). The particle-phase fraction of oxalate can then be expressed as:

$$222 \quad \varepsilon(C_2O_4^{2-}) = \frac{c(C_2O_4^T)}{c(C_2H_2O_4) + c(C_2O_4^T)} = \frac{[C_2HO_4^-]W_i}{c(C_2H_2O_4) + [C_2HO_4^-]W_i} \quad (7)$$

223 where W_i is the particle liquid water content associated with inorganic species ($\mu g\ m^{-3}$; mass per
224 volume of air). Note that the particle liquid water content associated with organic species is not
225 considered in this case, but it can be included. Alternatively, the measured particle water can be
226 used.

227 By putting equations (5) and (6) into equation (7), $\varepsilon(C_2O_4^{2-})$ can be expressed as:

$$228 \quad \varepsilon(C_2O_4^{2-}) = \frac{H_{C_2H_2O_4} W_i RT \left(\frac{1}{\gamma_{C_2H_2O_4}} + \frac{K_{a1}}{\gamma_{H^+} + \gamma_{C_2HO_4^-} [H^+]} + \frac{K_{a1}K_{a2}}{\gamma_{H^+} + \gamma_{H^+} + \gamma_{C_2O_4^{2-}} [H^+]^2} \right)}{1 + H_{C_2H_2O_4} W_i RT \left(\frac{1}{\gamma_{C_2H_2O_4}} + \frac{K_{a1}}{\gamma_{H^+} + \gamma_{C_2HO_4^-} [H^+]} + \frac{K_{a1}K_{a2}}{\gamma_{H^+} + \gamma_{H^+} + \gamma_{C_2O_4^{2-}} [H^+]^2} \right)} \quad (8)$$

229 At 298 K, $K_{a1} = 5.62 \times 10^{-2}$ mole L^{-1} and $K_{a2} = 1.55 \times 10^{-4}$ mole L^{-1} (Haynes, 2014). Assuming
230 that $\gamma_{H^+} = 1$, $K_{a1}K_{a2} \ll \gamma_{H^+} + \gamma_{H^+} + \gamma_{C_2O_4^{2-}} [H^+]^2$ for the conditions of our study. Hence, equation (8)
231 can be simplified to:

$$232 \quad \varepsilon(C_2O_4^{2-}) \cong \frac{H_{C_2H_2O_4} W_i RT \left(\frac{\gamma_{H^+} + \gamma_{C_2HO_4^-} [H^+] + K_{a1}}{\gamma_{C_2H_2O_4}} \right)}{\gamma_{H^+} + \gamma_{C_2HO_4^-} [H^+] + H_{C_2H_2O_4} W_i RT \left(\frac{\gamma_{H^+} + \gamma_{C_2HO_4^-} [H^+] + K_{a1}}{\gamma_{C_2H_2O_4}} \right)} \quad (9)$$

233 After accounting for the SI units and substituting $[H^+] = 10^{-pH}$, equation (9) becomes:

$$\varepsilon(C_2O_4^{2-}) \cong \frac{H_{C_2H_2O_4} W_i RT \left(\frac{\gamma_H + \gamma_{C_2HO_4^-}}{\gamma_{C_2H_2O_4}} 10^{-pH + K_{a1}} \right) \times 0.987 \times 10^{-14}}{\gamma_H + \gamma_{C_2HO_4^-} 10^{-pH} + H_{C_2H_2O_4} W_i RT \left(\frac{\gamma_H + \gamma_{C_2HO_4^-}}{\gamma_{C_2H_2O_4}} 10^{-pH + K_{a1}} \right) \times 0.987 \times 10^{-14}} \quad (10)$$

Note that 0.987×10^{-14} comes from using $R = 8.314 \text{ m}^3 \text{ Pa K}^{-1} \text{ mol}^{-1}$, and hence needing to convert 1 atm to 1 Pa and 1 L to 1 μg . We used the average of $H_{C_2H_2O_4}$ values provided by Clegg et al. (1996), Compernelle and Muller (2014) and Saxena and Hildemann (1996) ($6.11 \times 10^8 \text{ mole L}^{-1} \text{ atm}^{-1}$ at 25 °C), and accounted for the effect of temperature using equation 19 in Sander (2015). Although K_{a1} also depends on temperature, the K_{a1} value at 25 °C (5.62×10^{-2} , (Haynes, 2014)) is used for all the oxalic acid S curve calculations in this paper since equations that determine temperature-dependent K_{a1} values are not available. In addition, the temperatures observed in this study are close to 25 °C.

Figure S12 provides a conceptual picture of how the relationship between $\varepsilon(C_2O_4^{2-})$ and particle pH can change based on the time of the day. Different S curves for $\varepsilon(C_2O_4^{2-})$ are calculated using equation (10) and 1-hour average values obtained from the diurnal profiles of temperature and W_i (specifically at 00:30, 06:30 and 12:30). The S curves are shown to differ substantially due to the diurnal variations of temperature and W_i . For example, a decrease in temperature and an increase in W_i from 00:30 to 06:30 will result in the S curve shifting to the left, which indicates that a substantially higher fraction of gas-phase oxalic acid will partition to the particle phase for a given particle pH at 06:30 compared to at 00:30. Higher W_i also increases the fraction of oxalate that partitions to the particle phase due solely to solubility, as seen from the plateau regions at low pH in Fig. S12. Conversely, an increase in temperature and a decrease in W_i from 06:30 to 12:30 will result in a considerably lower fraction of gas-phase oxalic acid partitioning to the particle phase for a given particle pH at 12:30 compared to at 06:30.

S4. PILS-HPIC denuder efficiency

Post-field laboratory experiments were performed to determine if disagreements between the measured and predicted molar fractions of formic and acetic acid in the particle phase were due to positive biases in particle-phase PILS-HPIC measurements as a result of less than 100 % gas removal denuder efficiency and uptake of gases in the PILS liquid system. While experiments were done solely with formic acid, similar results are expected for acetic acid. In these

Deleted: S11

Deleted: S11

experiments, liquid formic acid (Sigma Aldrich, $\geq 99\%$) was diluted with ultrapure deionized water and placed in a bubbler. A flow of 18 mL min^{-1} of N_2 was passed through the formic acid in the bubbler. This formic acid air stream was then passed through a nafion dryer and diluted with 52 L min^{-1} of N_2 . Two experiments were performed. In the first experiment, the diluted formic acid air flow was introduced directly into the PILS, which was connected to a Metrohm 761 Compact IC (Metrohm AG). In the second experiment, the diluted formic acid air flow was passed through a 28 cm parallel plate carbon denuder (Sunset Lab) prior to introduction into the PILS-IC system.

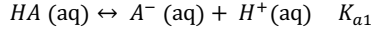
Our experiments showed that the IC detected formate when the diluted formic acid air flow was introduced directly into the PILS-IC system. IC analysis revealed that the gas-phase formic acid concentration was $\sim 75\text{ }\mu\text{g m}^{-3}$. However, no formate was detected above the limit of detection ($0.02\text{ }\mu\text{g m}^{-3}$) when the diluted formic acid air flow was passed through the carbon denuder prior to introduction into the PILS-IC system. These measurements indicated that the carbon denuder has a $\geq 99.97\%$ formic acid gas removal efficiency. Hence, these experiments indicate that the carbon denuder removes the formic acid gas completely. We conclude that disagreements between the measured and predicted molar fractions of formic and acetic acid in the particle phase were not due to positive biases in particle-phase formate and acetate PILS-HPIC measurements as a result of less than 100% gas removal denuder efficiency.

S5. Particle-phase formic and acetic acid dimers

Previous studies have shown that formic and acetic acid dimers may form in the aqueous phase (Schrier et al., 1964; Gilson et al., 1997; Chen et al., 2008). If the aforementioned acid dimers are present in aerosols, equilibrium between gas-phase formic/acetic acid (denoted as HA) and particle-phase formate/acetate (denoted as A^-) will differ from that predicted assuming no dimers existed, as done in the main text.

The dissolution of HA into the aqueous phase (assuming particles are liquids), followed by the formation of particle-phase dimers (denoted as $(\text{HA})_2$) and dissociation of the dissolved HA:





for which the reaction equilibriums are expressed as follows:

$$H_{HA} = \gamma_{HA}[HA]/p_{HA} \quad (11)$$

$$K_{dim} = \frac{[(HA)_2]}{[HA]^2} \quad (12)$$

$$K_{a1} = \frac{\gamma_{A^-}[A^-]\gamma_{H^+}[H^+]}{\gamma_{HA}[HA]} \quad (13)$$

where H_{HA} (mole L⁻¹ atm⁻¹) is the Henry's law constant for formic or acetic acid, K_{a1} (mole L⁻¹) is the first acid dissociation constants for formic or acetic acid, p_{HA} (atm) is the partial pressure of formic or acetic acid in the atmosphere, K_{dim} (L mole⁻¹) is the dimerization constant, and γ_i 's are activity coefficients. In equations (11) to (13), [x] represents aqueous concentrations (mole L⁻¹).

The total dissolved formate or acetate (A^T) can be expressed as:

$$[A^T] = [HA] + [A^-] + [(HA)_2] \quad (14)$$

Using equations (11) to (13), $[A^T]$ can be expressed as:

$$[A^T] = H_{HA}p_{HA} \left(\frac{1}{\gamma_{HA}} + \frac{K_{a1}}{\gamma_{H^+}\gamma_{A^-}[H^+]} + \frac{K_{dim}H_{HA}p_{HA}}{\gamma_{HA}\gamma_{HA}} \right) \quad (15)$$

The ideal gas law gives:

$$c(HA) = \frac{p_{HA}}{RT} \quad (16)$$

where R is the gas constant, T is temperature, and $c(x)$ represents concentration per volume of air (mole m⁻³). The particle-phase fraction of formate or acetate can then be expressed as:

$$\varepsilon(A^-) = \frac{c(A^T)}{c(HA) + c(A^T)} = \frac{[A^T]W_i}{c(HA) + [A^T]W_i} \quad (17)$$

where W_i is the particle liquid water content associated with inorganic species (μg m⁻³; mass per volume of air). Particle liquid water content associated with organic species is not considered in this case, but it can be included. Alternatively, the measured particle water can be used.

By putting equations (15) and (16) into equation (17), and accounting for the SI units, $\varepsilon(A^-)$ can ultimately be expressed as:

$$\varepsilon(A^-) = \frac{H_{HA} W_i RT \left(\frac{1}{\gamma_{HA}} + \frac{K_{a1}}{\gamma_{H^+} \gamma_{A^-} 10^{-pH}} + \frac{K_{dim} H_{HA} p_{HA}}{\gamma_{HA} \gamma_{HA}} \right) \times 0.987 \times 10^{-14}}{1 + H_{HA} W_i RT \left(\frac{1}{\gamma_{HA}} + \frac{K_{a1}}{\gamma_{H^+} \gamma_{A^-} 10^{-pH}} + \frac{K_{dim} H_{HA} p_{HA}}{\gamma_{HA} \gamma_{HA}} \right) \times 0.987 \times 10^{-14}} \quad (18)$$

At 298 K, K_{a1} values are 1.78×10^{-4} mole L⁻¹ and 1.75×10^{-5} mole L⁻¹ for formic and acetic acid, respectively (Haynes, 2014). K_{dim} values are 0.56 L mole⁻¹ and 0.92 L mole⁻¹ for formic and acetic acid, respectively (Chen et al., 2008). Temperature-dependent H_{HA} values for formic and acetic acid can be obtained from Sander (2015). p_{HA} can be calculated from the measured gas-phase formic or acetic acid concentrations ($\mu\text{g m}^{-3}$) and the ideal gas law. We used the web version of AIOMFAC (www.aiomfac.caltech.edu) (Zuend et al., 2008; Zuend et al., 2011; Zuend et al., 2012) to compute study-averaged γ_{HA} values of 0.334 and 2.150 for formic and acetic acid, respectively. We assumed that $\gamma_{H^+} \gamma_{A^-} = \gamma_{H^+} \gamma_{NO_3^-} = 0.07$ for both formic and acetic acid.

Comparison of S curves generated from equation (18) and those generated from equations (5) and (6) in the main text (which assumed that no dimers existed) showed that accounting for the presence of acid dimers increased predicted $\varepsilon(A^-)$ values by less than 1 % for particle pH 0.9 to 3.8 (i.e., pH values in this study). S curves generated by equation (18) also do not match our measured molar fractions of formic and acetic acid in the particle phase. This analysis shows that the molar fractions of formic and acetic acid in the particle phase do not change substantially when the presence of particle-phase acid dimers is accounted for due to the somewhat low H_{HA} values for formic and acetic acid. Hence, disagreements between the measured and predicted molar fractions of formic and acetic acid in the particle phase are not due to the presence of particle-phase formic and acetic acid dimers.

337 **References**

- 338 Acree, W., and Chickos, J. S.: Phase Transition Enthalpy Measurements of Organic and
339 Organometallic Compounds. Sublimation, Vaporization and Fusion Enthalpies From 1880 to
340 2010, J. Phys. Chem. Ref. Data, 39, 942, 10.1063/1.3309507, 2010.
- 341 Chen, J. H., Brooks, C. L., and Scheraga, H. A.: Revisiting the carboxylic acid dimers in aqueous
342 solution: Interplay of hydrogen bonding, hydrophobic interactions, and entropy, Journal of
343 Physical Chemistry B, 112, 242-249, 10.1021/jp074355h, 2008.
- 344 Clegg, S. L., Brimblecombe, P., and Khan, L.: The Henry's law constant of oxalic acid and its
345 partitioning into the atmospheric aerosol, Idojaras, 100, 51-68, 1996.
- 346 Compernelle, S., and Muller, J. F.: Henry's law constants of diacids and hydroxy polyacids:
347 recommended values, Atmos. Chem. Phys., 14, 2699-2712, 10.5194/acp-14-2699-2014, 2014.
- 348 Daubert, T. E., and Danner, R. P.: Physical and thermodynamic properties of pure chemicals: data
349 compilation, Taylor & Francis, Washington, DC, 1989.
- 350 Farmer, D. K., Matsunaga, A., Docherty, K. S., Surratt, J. D., Seinfeld, J. H., Ziemann, P. J., and
351 Jimenez, J. L.: Response of an aerosol mass spectrometer to organonitrates and organosulfates and
352 implications for atmospheric chemistry, Proceedings of the National Academy of Sciences of the
353 United States of America, 107, 6670-6675, 10.1073/pnas.0912340107, 2010.
- 354 Gilson, M. K., Given, J. A., Bush, B. L., and McCammon, J. A.: The statistical-thermodynamic
355 basis for computation of binding affinities: A critical review, Biophysical Journal, 72, 1047-1069,
356 10.1016/s0006-3495(97)78756-3, 1997.
- 357 Haynes, W. M.: CRC handbook of chemistry and physics: A ready-reference book of chemical
358 and physical data. , Boca Raton: CRC Press, 2014.
- 359 Lide, D. R.: CRC handbook of chemistry and physics: a ready-reference book of chemical and
360 physical data, CRC Press, Boca Raton, FL, 1995.

361 Nah, T., Ji, Y., Tanner, D. J., Guo, H., Sullivan, A. P., Ng, N. L., Weber, R. J., and Huey, L. G.:
 362 Real-time measurements of gas-phase organic acids using SF₆- chemical ionization mass
 363 spectrometry, *Atmos. Meas. Tech. Discuss.*, 2018, 1-40, 10.5194/amt-2018-46, 2018.

364 Neuman, J. A., Ryerson, T. B., Huey, L. G., Jakoubek, R., Nowak, J. B., Simons, C., and
 365 Fehsenfeld, F. C.: Calibration and evaluation of nitric acid and ammonia permeation tubes by UV
 366 optical absorption, *Environmental Science & Technology*, 37, 2975-2981, 10.1021/es0264221,
 367 2003.

368 Sander, R.: Compilation of Henry's law constants (version 4.0) for water as solvent, *Atmos. Chem.*
 369 *Phys.*, 15, 4399-4981, 10.5194/acp-15-4399-2015, 2015.

370 Saxena, P., and Hildemann, L. M.: Water-soluble organics in atmospheric particles: A critical
 371 review of the literature and application of thermodynamics to identify candidate compounds,
 372 *Journal of Atmospheric Chemistry*, 24, 57-109, 10.1007/bf00053823, 1996.

373 Schrier, E. E., Pottle, M., and Scheraga, H. A.: The Influence of Hydrogen and Hydrophobic Bonds
 374 on the Stability of the Carboxylic Acid Dimers in Aqueous Solution, *Journal of the American*
 375 *Chemical Society*, 86, 3444-3449, 10.1021/ja01071a009, 1964.

376 Xu, L., Suresh, S., Guo, H., Weber, R. J., and Ng, N. L.: Aerosol characterization over the
 377 southeastern United States using high-resolution aerosol mass spectrometry: spatial and seasonal
 378 variation of aerosol composition and sources with a focus on organic nitrates, *Atmos. Chem. Phys.*,
 379 15, 7307-7336, 10.5194/acp-15-7307-2015, 2015.

380 Xu, L., Guo, H. Y., Weber, R. J., and Ng, N. L.: Chemical Characterization of Water-Soluble
 381 Organic Aerosol in Contrasting Rural and Urban Environments in the Southeastern United States,
 382 *Environmental Science & Technology*, 51, 78-88, 10.1021/acs.est.6b05002, 2017.

383 Zuend, A., Marcolli, C., Luo, B. P., and Peter, T.: A thermodynamic model of mixed organic-
 384 inorganic aerosols to predict activity coefficients, *Atmos. Chem. Phys.*, 8, 4559-4593,
 385 10.5194/acp-8-4559-2008, 2008.

386 Zuend, A., Marcolli, C., Booth, A. M., Lienhard, D. M., Soonsin, V., Krieger, U. K., Topping, D.
 387 O., McFiggans, G., Peter, T., and Seinfeld, J. H.: New and extended parameterization of the

388 thermodynamic model AIOMFAC: calculation of activity coefficients for organic-inorganic
389 mixtures containing carboxyl, hydroxyl, carbonyl, ether, ester, alkenyl, alkyl, and aromatic
390 functional groups, *Atmos. Chem. Phys.*, 11, 9155-9206, 10.5194/acp-11-9155-2011, 2011.

391 Zuend, A., Marcolli, C., Luo, B. P., and Peter, T.: A thermodynamic model of mixed organic-
392 inorganic aerosols to predict activity coefficients (vol 8, pg 4559, 2008), *Atmos. Chem. Phys.*, 12,
393 10075-10075, 10.5194/acp-12-10075-2012, 2012.

394